IMPLEMENTATION OF METAL-BASED MICROCHANNEL HEAT EXCHANGERS IN A MICROREFRIGERATION CYCLE, AND NUMERICAL AND EXPERIMENTAL INVESTIGATION OF SURFACE ROUGHNESS EFFECTS ON FLOW BOILING

A THESIS SUBMITTED TO
THE GRADUATE SCHOOL OF NATURAL AND APPLIED SCIENCES
OF
MIDDLE EAST TECHNICAL UNIVERSITY

BY
RAHIM JAFARI KHOUSHEH MEHR

IN PARTIAL FULLFILLMENT OF THE REQUIREMENTS
FOR
THE DEGREE OF DOCTORATE
IN
MECHANICAL ENGINEERING

SEPTEMBER 2015

Approval of the thesis:

IMPLEMENTATION OF METAL-BASED MICROCHANNEL HEAT EXCHANGERS IN A MICROREFRIGERATION CYCLE, AND NUMERICAL AND EXPERIMENTAL INVESTIGATION OF SURFACE ROUGHNESS EFFECTS ON FLOW BOILING

submitted by **RAHIM JAFARI KHOUSHEH MEHR** in partial fulfillment of the requirements for the degree of **Doctorate in Department of Mechanical Engineering, Middle East Technical University** by,

Prof. Dr. Gülbin Dural Ünver
Dean, Graduate School of **Natural and Applied Sciences** ____________________

Prof. Dr. Tuna Balkan
Head of Department, **Mechanical Engineering** ____________________

Assoc. Prof. Dr. Tuba Okutucu-Özyurt
Supervisor, **Mechanical Engineering Dept., METU** ____________________

Asst. Prof. Dr. Hakkı Özgür Ünver
Co-Supervisor, **Mechanical Engineering Dept., TOBB University** ____________________

Examining Committee Members:

Assoc. Prof. Dr. İlker Tarı
Mechanical Engineering Dep., METU ____________________

Assoc. Prof. Dr. Tuba Okutucu-Özyurt
Mechanical Engineering Dep., METU ____________________

Assist. Prof. Dr. Özgür Bayer
Mechanical Engineering Dept., METU ____________________

Prof. Dr. S. Engin Kılıç
Manufacturing Engineering Dep., Atılım University ____________________

Assoc. Prof. Dr. Barbaros Çetin
Mechanical Engineering Dept., Bilkent University ____________________

Date: 01.09.2015

I hereby declare that all information in this document has been obtained and presented in accordance with academic rules and ethical conduct. I also declare that, as required by these rules and conduct, I have fully cited and referenced all material and results that are not original to this work.

Name, Last Name: Rahim JAFARI KHOUSHEH MEHR

Signature:

ABSTRACT

IMPLEMENTATION OF METAL-BASED MICROCHANNEL HEAT EXCHANGERS IN A MICROREFRIGERATION CYCLE, AND NUMERICAL AND EXPERIMENTAL INVESTIGATION OF SURFACE ROUGHNESS EFFECTS ON FLOW BOILING

JAFARI KHOUSHEH MEHR, Rahim

Ph.D., Department of Mechanical Engineering

Supervisor: Associate Professor Dr. Tuba OKUTUCU-ÖZYURT

Co-Supervisor: Assistant Professor Dr. Hakkı Özgür ÜNVER

September 2015, 128 pages

A microscale vapor compression refrigeration cycle has been constructed for possible application in the thermal management of compact electronic components. The micro-evaporator and micro-condenser components have been fabricated using wire electron discharge machining and micromilling, respectively. Three micro-evaporators have been manufactured with different surface roughness for the experimental and numerical investigation of roughness effect on nucleate flow boiling in microchannels.

In the numerical part of the study, two different techniques have been employed to simulate the evaporation in the microchannels. Firstly, the Arbitrary Lagrangian-Eulerian Method is used to investigate the hydrodynamics and heat transfer characteristics of a vaporized elongated bubble, and two successive bubbles in a microtube. Then, phase-field method is utilized, uniquely, for the simulation of saturated and subcooled water boiling in the microchannels with different size of cavities as a preliminary model for the surface roughness.

Manufacturing experiments with various process parameters have been conducted to create the different surface roughness values in the oxygen free copper micro-evaporator channels.

In the experimental evaluation part, the hydrodynamics and heat transfer performance of the three microchannel evaporators of the same dimensions and different surface roughness have been compared at variously imposed heat fluxes and mass fluxes. R134a has been used as the refrigerant with saturation temperature of 10°C at mass fluxes of 85 and 200 kg/(m^2·s). The results demonstrated that roughness yields up to 45% enhancement in two-phase heat transfer coefficient at low to moderate heat flux values ranging from 0 to 48 W/cm^2.

Keywords: Vapor compression refrigeration cycle, micro-evaporator, micro-condenser, boiling, ALE method, phase-field method, surface roughness, micro-fabrication

ÖZ

METAL TABANLI MİKROKANALLI ISI DEĞİŞTİRİCİLERİN BİR MİKRO SOĞUTMA ÇEVRİMİNE UYGULANMASI; YÜZEY PÜRÜZLÜĞÜNÜN BUHARLAŞMAYA ETKİSİNİN SAYISAL VE DENEYSEL İNCELEMESİ

JAFARI KHOUSHEH MEHR, Rahim

Doktora, Makina Mühendisliği Bölümü

Tez Yöneticisi: Doç. Dr. Tuba OKUTUCU-ÖZYURT

Ortak Tez Yöneticisi: Y. Doç. Dr. Özgür ÜNVER

Eylül 2015, 128 sayfa

Yüksek yoğunluklu elektronik bileşenlerin olası soğutma uygulamaları için mikro ölçekli bir buhar sıkıştırmalı soğutma çevrimi kurulmuştur. Mikro-buharlaştırıcı ve mikro-yoğuşturucu bileşenleri, sırasıyla tel erozyon ve mikro- frezeleme yöntemleri ile üretilmiştir. Yüzey pürüzlülüğünün mikrokanallarda akış tipi kabarcıklı kaynamaya etkisinin deneysel ve sayısal incelemesi için, farklı yüzey pürüzlüğünde üç mikro-buharlaştırıcı test bileşeni üretilmiştir.

Çalışmanın sayısal kısmında, mikrokanallardaki buharlaşmayı benzetimlemek için iki farklı tekniğe yer verilmiştir. Öncelikle, bir mikrotüpte buharlaşmış ve uzamış kabarcığın, ve birbirini izleyen iki kabarcığın hidrodinamik ve ısıl niteliklerini araştırmak için Rastgele Lagrange-Euler (Arbitrary Lagrangian-Eulerian) yöntemi

kullanılmıştır. Ardından faz-alan (phase field) yöntemi ile, ilk kez, yüzey pürüzlülüğünün bir ön modeli olarak farklı büyüklüklerde oyuklara sahip mikrokanallarda doymuş ve soğutulmuş suyun kaynaması benzetimlenmiştir.

Mikro-buharlaştırıcının oksijensiz bakır kanallarında farklı yüzey pürüzlükleri yaratmak için değişik süreç parametrelerini içeren üretim deneyleri yapılmıştır.

Çalışmanın deneysel değerlendirme kısmında, aynı boyutlarda olan, ancak farklı yüzey pürüzlüğüne sahip üç mikro-buharlaştırıcının ısı geçiş ve hidrodinamik performansı, uygulanan çeşitli ısı ve kütle akılarında karşılaştırılmıştır. Soğutkan olarak, 10°C doyma sıcaklığında, 85 kg/(m^2·s) ve 200 kg/(m^2·s) kütle akılarında R134a kullanılmıştır. Sonuçlar, yüzey pürüzlülüğünün, 0 ile 48 W/cm^2 arasında değişen düşük/orta ısı akısı değerlerinde iki fazlı ısı transfer katsayısında %45'e varan bir artış sağladığını ortaya koymuştur.

Anahtar Kelimeler: Buhar sıkıştırmalı soğutma çevirimi, mikro-buharlaştırıcı, mikro-yoğuşturucu, kaynama, ALE yöntemi, faz alanı yöntemi, yüzey pürüzlülüğü, mikro-üretim

ACKNOWLEDGEMENTS

I would like to express my gratitude to my advisor Dr. Tuba Okutucu for her great support and perfect guidance and encouragement. I would like to thank my co-advisor Dr. Özgür Ünver and my advisory committee members Prof. Engin Kılıç and Dr. Barbaros Çetin for their constructive advice and suggestions. I also appreciate Dr. Özgür Bayer for his helpful guidance.

I want to thank Mr. Samad Nadimi, Dr. Yiğit Karpat, Dr. Şakir Baytaroğlu and Mustafa Kılıç at Micro System Design and Manufacturing Center at Bilkent University for fabrication of the microchannels. A big thank you to Mr. Mustafa Yalçın for the help in the construction of the test setup of the micro refrigeration cycle. I also thank to my group mate Göker Türkakar for the discussion and exchanges.

I would like to thank my wife and my parents for their patience and support.

Finally, I would gratefully acknowledge full project support under grant number 11M168 from the Scientific and Technological Research Council of Turkey (TÜBİTAK).

TABLE OF CONTENTS

ABSTRACT v

ÖZ vii

ACKNOWLEDGEMENTS ix

TABLE OF CONTENTS x

LIST OF TABLES xiv

LIST OF FIGURES xv

LIST OF SYMBOLS AND ABBREVIATIONS xix

1 INTRODUCTION 1

1.1 Motivation 1

1.2 The Objective and Scope of the Thesis 3

2 BACKGROUND AND PRIOR RESEARCH 5

2.1 Two-Phase Flow Boiling 5

2.1.1 Nucleation Theory 5

2.1.2 Critical Heat Flux and Heat Transfer Coefficient 6

2.2 Effective Surface Characteristics for Flow Boiling 6

2.2.1 Surface Porosity 7

2.2.2 Surface Wettability 7

2.2.3 Surface Roughness 7

2.3 Microchannel Heat Sinks 8

2.3.1 Single Phase Flow in Microchannels 8

2.3.2 Two-Phase Flow in Microchannels 9

2.3.3 Microscale Refrigeration System 9

2.3.4 Techniques for Fabrication of Metal-Based Microchannels 13

2.3.5 Surface Roughness Parameters and Related Studies in Flow Boiling in Microchannels 16

2.4 Experimental and Numerical Studies for Flow Boiling in Microchannels 18

2.4.1 Experimental Studies to Investigate the Flow Boiling in Microchannels 18

2.4.2 Numerical Methods to Simulate the Flow boiling in Microchannels 20

2.5 Contribution of the Present Study 22

3 NUMERICAL MODEL 1: ARBITRARY LAGRANGIAN-EULERIAN METHOD 23

3.1 Arbitrary Lagrangian-Eulerian Method 23

3.2 Domain Equations and Boundary Conditions 24

3.3 Validation of the Model 27

3.4 Simulation of the Nucleated Bubble in the Microtube 28

3.5 Results and Discussions of the Simulation for Single Bubble and Two Successive Bubbles 29

4 NUMERICAL MODEL 2: PHASE-FIELD METHOD 37

4.1 Cahn-Hilliard Phase-Field Method 37

4.2 Numerical Model and Governing Equations 41

4.3 Simulation of the Nucleated Bubble in the Superheated Fluid in the Microchannel 43

4.3.1 Geometry and Computational Domain 43

4.3.2 Mesh Convergence Analysis 44

4.3.3 Validation of the Model 46

4.3.4 Results and Discussion 49

4.4 Simulation of the Nucleation from an Artificial Cavity of the Subcooled Water into the Microchannel 57

4.4.1 Geometry and Computational Domain 57

4.4.2 Results and Discussion 57

4.5 Simulation of the Surface Roughness Effect on Evaporation with Multi-Cavities in the Microchannels 67

5 FABRICATION OF MICROCHANNEL HEAT EXCHANGERS 69

5.1 Micro-Evaporator Fabrication 69

5.1.1 The Machine Specifications 69

5.1.2 Process Parameters 70

5.1.3 Surface Roughness Parameters 71

5.1.4 Design of Experiments with Taguchi Technique 73

5.1.5 Measurement of the Surface Roughness 74

5.1.6 Data Analysis 76

5.1.7 Modeling of the Results 78

5.1.8 Visualization of the Surface Texture under the Optic Microscope and SEM 80

5.2 Micro-Condenser Fabrication 84

5.2.1 The Machine Specifications 84

5.2.2 Process Parameters 84

5.2.3 Visualization 84

6 EXPERIMENTAL STUDY 87

6.1 Experimental Facilities 87

6.1.1 Test Setup 87

6.1.2 The Test Piece (Micro-Evaporator) 90

6.1.3 Test Section 92

6.1.4 Heat Flux Distribution within the Test Section 94
6.2 Energy Balance of the Cycle with the First Law of Thermodynamics 97
6.3 Vapor Quality Calculation in the Test Section 98
6.4 Uncertainty Analysis 99
6.5 Experimental Results 101
6.5.1 Wall Heat Transfer Coefficient 101
6.5.2 Pressure Drop 106
6.5.3 Coefficient of Performance (COP) 108
6.6 Preliminary Tests with Micro-Condenser 109
7 CONCLUSIONS AND FUTURE RECOMMENDATIONS 111
7.1 Conclusions 111
7.2 Future Work 114
REFERENCES 115
APPENDICES 127
A. CURRICULUM VITE 127

LIST OF TABLES

TABLES

Table 1.1 Heat flux limits for various cooling methods [4] 2
Table 2.1 The characteristics of availabe micro refrigeration systems in the literature 11
Table 2.2 Manufacturing methods and their parameters for metal based microchannels... 15
Table 4.1Comparison of the removed heat flux at the bottom wall and pressure drop in three microchannels with different surface roughness.. 68
Table 5.1 Adjustable and fixed parameters of machining... 71
Table 5.2 Levels of the process parameters 74
Table 5.3 Experimental design due to Taguchi method and surface roughness results 75
Table 5.4 Surface roughness results from the repetition of two experiments (2 and 14)... 75
Table 6.1 Application and specifications of the components used in the test setup .. 89
Table 6.2 Surface roughness parameters of the microchannels in three evaporator test pieces 91
Table 6.3 Temperatures and Pressures at Various States of the Cycle at Q = 50 W . 97
Table 6.4 Uncertainty results 101
Table 6.5 Comparison of COP values at the same cooling load with varying roughness.. 109
Table 6.6 Temperatures and pressures at various states of the cycle with micro-condenser at saturation temperature of 13.3°C 110

LIST OF FIGURES

FIGURES

Figure 2.1 Heterogeneous bubble nucleation (a) from a cavity and (b) on a smooth surface 6
Figure 3.1 The comparison of the bubble growth rates of the simulation and the analytical solution 28
Figure 3.2 The bubble growth in the microtube 29
Figure 3.3 (a) Grid distribution at the initial time (b) deformed mesh at t = 0.19 ms and (c) remeshed grids at t = 0.19 ms 30
Figure 3.4 Velocity distribution at t = 0.7 ms 31
Figure 3.5 Temperature distribution inside and around the vapor bubble at t = 0.7 ms 32
Figure 3.6 Local heat transfer coefficient along the wall of the microchannel for elongated bubble at t = 0.7 ms 33
Figure 3.7 Pressure distribution at different time steps 34
Figure 3.8 (a) Velocity distribution, (b) temperature distribution, and (c) pressure distribution of two elongated bubbles in the microtube at t = 0.57 ms 35
Figure 4.1 The computational domain (dimensions in μm) 44
Figure 4.2 The close up view of the computational mesh inside and around the initial bubble 45
Figure 4.3 Equivalent diameter of the bubble with three different grid sizes 46
Figure 4.4 The comparison of the bubble growth rates of the present numerical simulation and the experimental data [60] 47
Figure 4.5 The comparison of the bubble shapes of the present numerical study (left) and the experimental study [60] (right), at the same instant. 48
Figure 4.6 The surface tension and mixing energy in the bubble interface 49

Figure 4.7 The velocity distribution inside and around the elongated vapor bubble (a) XY plane and (b) ZY plane at t = 1.8 ms 50
Figure 4.8 The temperature distribution inside and around the elongated vapor bubble (a) XY plane and (b) ZY plane at t = 1.8 ms 51
Figure 4.9 The local heat transfer coefficient and the heat flux on (a) the bottom wall and (b) the side wall at t = 1.8 ms 52
Figure 4.10 The average heat transfer coefficients over the side walls and the bottom wall 53
Figure 4.11 The pressure distributions of the central XY plane (a) and the central ZY plane (b) at t = 1.8 ms 54
Figure 4.12 The effect of the contact angle on the average heat transfer coefficient for the inlet velocity of 0.0645 m/s 55
Figure 4.13 The effect of the contact angle on the average heat transfer coefficient for the inlet velocity of 0.129 m/s 56
Figure 4.14 The effect of the contact angle on the average heat transfer coefficient for the inlet velocity of 0.258 m/s 56
Figure 4.15 Computational domain, initial and boundary conditions (dimensions in μm's) 57
Figure 4.16 The bubble formation and departure from the microcavity 58
Figure 4.17 Comparison of the bubble radius obtained by the present numerical study and available experimental data [87] 59
Figure 4.18 Comparison of the bubble shape at different times obtained by the present numerical study (right) and the experimental data (left) [87] 60
Figure 4.19 Velocity distribution in the two-phase section of the microchannel 62
Figure 4.20 Temperature distribution in the two-phase section of the microchannel 62
Figure 4.21 Pressure distributions in the two-phase zone of the microchannel at various time steps 62
Figure 4.22 The flow pattern for different inlet mass fluxes at t = 10 ms 63
Figure 4.23 The local removed heat flux and heat transfer coefficient for the bottom wall in the flow streamwise direction for mass fluxes of (a) G = 32 kg/m^2· s and (b) G = 255 kg/m^2·s at t = 10 ms 64

Figure 4.24 Heat transfer coefficient and removed heat flux from the bottom heated wall at x = 22 mm with two different mass fluxes of (a) G = 32 kg/m^2·s and (b) G = 255 kg/m^2·s.. 66
Figure 4.25 (a) Microchannel with multi-cavities (b) geometry and dimensions (μm) of three different cavities 67
Figure 4.26 Bubble generation and movement along the microchannel for three different cavity geometries.. 68
Figure 5.1 Sodick AP250L WEDM machine used to fabricate the micro channels (Courtesy of Center for Microsystem Design and Manufacturing Center, Bilkent University) 70
Figure 5.2 Definition of the surface roughness parameters of R_a, R_z, R_v and S_m 73
Figure 5.3 S/N ratio plots of (a) R_a, (b) R_z, (c) R_v and (d) S_m 77
Figure 5.4 Mean squared errors of the training and the test results 79
Figure 5.5 The linear regressions between the outputs and targets of the network ... 79
Figure 5.6 Optical images of the surfaces for the 25 experiments............................. 80
Figure 5.7 SEM images of the surfaces of microchannels.. 82
Figure 5.8 SEM images of experiments 6, 24, 14 and 15 with the magnification of 8000.. 83
Figure 5.9 The condenser with microchannels 85
Figure 5.10 The microchannels of the condenser at two different magnifications... 85
Figure 6.1 Schematic diagram of the test setup 87
Figure 6.2 Photograph of the test setup... 88
Figure 6.3 The evaporator test piece 90
Figure 6.4 Side view of the fabricated microchannels (dimensions in μm) 91
Figure 6.5 Optical microscopic images from surfaces of microchannels on three different evaporator test pieces 92
Figure 6.6 Explosive view of the evaporator test section 93
Figure 6.7 (a) Temperature distribution in the designed evaporator (b) heat flux distribution at the lateral cross section and (c) on the plane just one millimeter under the microchannels... 95
Figure 6.8 Pressure-enthalpy diagram of the refrigeration cycle 99

Figure 6.9 The effect of microchannels' surface roughness on heat transfer coefficient with a mass flux of G = 85 kg/m^2·s and inlet vapor quality of x = 0.5 .. 103
Figure 6.10 The effect of microchannels' surface roughness on heat transfer coefficient with a mass flux of G = 85 kg/m^2·s and inlet vapor quality of x = 0.3 .. 103
Figure 6.11 The effect of microchannels' surface roughness on heat transfer coefficient with a mass flux of G = 200 kg/m^2·s and inlet vapor quality of x = 0.5 105
Figure 6.12 The effect of microchannels surface roughness on heat transfer coefficient with a mass flux of G = 200 kg/m^2·s and inlet vapor quality of x = 0.8 105
Figure 6.13 Total pressure drop for the mass flux of G = 85 kg/m^2·s and inlet vapor quality of x = 0.5 107
Figure 6.14 Total pressure drop for the mass flux of G = 200 kg/m^2·s and inlet vapor quality of x = 0.5 107
Figure 6.15 COP of the micro refrigeration cycle with two different mass fluxes .. 108
Figure 6.16 Photograph of the test setup with the micro-condenser 110

LIST OF SYMBOLS AND ABBREVIATIONS

C	Capacitance [pF]
C_p	Specific heat [J/kg·K]
Ca	Capillary number, $Ca = \frac{\mu u}{\sigma}$
f	Function
F	Volume force vector [N/m^3]
f_{mix}	Mixing energy [N]
g	Gravitational acceleration vector [m/s^2]
G	Chemical potential [Pa], mass flux [kg/m^2·s]
h	Thickness of the liquid film [μm], heat transfer coefficient [W/m^2·K]
h_{lg}	Latent heat [J/kg]
i	Enthalpy [kJ/kg]
I	Identity matrix
I_1	Invariant
J	Invariant
k	Thermal conductivity [W/m·K]
L	Length [μm]
M_f	Mass flux [kg/m^2·s]
m	Mass Flux [kg/m^2·s]
n	Unit normal to interface

p	Pressure [Pa]
q''	Local heat flux [W/m^2]
r	Radius [μm], constant [m/s]
R	Radius [m], constant [m/s]
R_a	Arithmetical average height [μm]
R_v	Maximum depth of the valleys [μm]
R_z	Ten point height [μm]
Re	Reynolds number, $Re = \frac{\rho u d}{\mu}$
S_m	Mean spacing at mean line [μm]
S_X	Material domain
S_x	Spatial domain
S_χ	Reference domain
SF	Feed rate of servo speed [mm/min]
t	Time [s]
T	Temperature [K]
T_{on}	Pulse on time [μs]
T_{off}	Pulse off time [μs]
$\boldsymbol{u}$	Velocity vector [m/s]
u_{mesh}	Velocity of the mesh at the interface [m/s]
V	Voltage [V], Volume [m^3]
V_f	volume fraction
WS	Wire speed [m/min]
x	Vapor quality
x_p	Axial location [μm]

Greek

β	Coefficient
γ	Mobility [$m^3 \cdot s/kg$]
δ	Smoothed representation of the interface [1/m]
ϵ	Capillary width [m]
λ	Mixing energy density [N]
μ	Dynamic viscosity [Pa·s]
μ'	Artificial Modula
ρ	Density [kg/m^3]
σ	Surface tension [Pa]
κ	Bulk Modula
τ	Viscous stress tensor [Pa]
ϕ	Phase field variable
ψ	Secondary phase field variable
∇	Gradient operator

Subscripts

b	Bubble
g	Gas
L	Liquid
s	Surface
sat	Saturation
v	Vapor

CHAPTER 1

INTRODUCTION

1.1 Motivation

Fabrication of integrated circuits with higher performance is now possible owing to novel manufacturing techniques. The main obstacle in achieving such high performances with more compact and functional devices is the dissipation of heat due to the increased power density. International Technology Roadmap for Semiconductors predicts maximum heat flux of 108 W/cm^2, maximum junction temperature of 85ºC, and an extreme ambient temperature of 45ºC for desktop personal computers in 2016 [1]. It may be inferred from this trend that the difference between junction and ambient temperatures is decreasing, and the heat flux is increasing. Additionally, the average power density for specialty applications such as laser diode arrays, phased array radar systems and power electronics, raised over 1000 W/cm^2 [2,3]. Hence the conventional air cooling systems, which are currently preferable and commercial to save the costs, seem to be unsatisfactory to overcome this challenge. Table 1.1 represents the limitations of the techniques to dissipate the heat for CPU cooling [4]. It may be observed from Table 1.1 that forced air cooling in combination with heat sinks is typically limited to 20 W/cm^2, whereas the phase change based cooling techniques such as pool boiling, flow boiling and spray, potentially remove higher heat fluxes over 100 W/cm^2.

Table 1.1 Heat flux limits for various cooling methods [4]

	Air		Fluorinert			Water		
Cooling Method	Natural Convection	Heat Sink	Pool Boiling	Spray Cooling	Pool Boiling	Spray Cooling	Flow Boiling	Jet Impingement
Heat Flux (W/cm^2)	0.01-1	0.1-20	1-50	10-150	10-100	$100\text{-}10^3$	$100\text{-}10^3$	$10^3\text{-}10^5$

There are many experimental data and correlations in the literature with adjustable parameters which can provide quick input to design and performance evaluation studies involving phase change process. However, the available information loses its value as the parameters of interest start falling outside the range of physical parameters for which the experimental data and correlations were developed. It is, therefore, necessary to take a deeper insight into phase change of the microscale.

Moreover, to reduce the repetition of experiments, understanding of the fundamentals of two phase flow at the microscale is essential. Numerical analyses are valuable tools to simulate the process of boiling in microchannels. Although the modeling of the two-phase flow with evaporation is a difficult issue due to the complexity of the non-linear set of equations that governs the two-phase flow and the interfacial deformation between the vapor and the liquid phases, it reduces the cost and time compared to those for experimental tests.

The heating surface condition is one of the parameters that has a significant influence on nucleate boiling heat transfer. The investigation of the effect of the surface roughness, typical standard parameters characterize the surface attributes, on the boiling heat transfer of the microchannels seems interesting. To do this numerically, available numerical methods in the literature could be extended to simulate the evaporation from the surfaces of the microchannels. Furthermore, it would be investigated experimentally, by constructing a microscale vapor compression refrigeration cycle.

1.2 The Objective and Scope of the Thesis

The ultimate goal in the present study is cooling electronic devices. Boiling heat transfer is utilized to manage cooling. A complete microscale refrigeration cycle has been constructed and tested for this purpose. The evaporator and condenser sections of the cycle have been fabricated as microchannel heat exchangers. The emphasis is given to the micro-evaporator section of the cycle. The effect of surface roughness on flow boiling in the micro-evaporator has been investigated both numerically and experimentally. The thesis is organized as follows:

Chapter 2 comprises the literature survey including two-phase flow boiling in microchannels and the effect of surface characteristics on nucleation boiling in the microchannels. Also, available numerical studies used for the simulation of the evaporation in microchannels have been reported.

In chapter 3, the Arbitrary Lagrangian-Eulerian Method is used to investigate the hydrodynamics and heat transfer characteristics of a vaporized elongated bubble in a microtube. Then, the method is extended to simulate the interactive effect of two successive bubbles.

In chapter 4, the phase-field method is verified to simulate the saturated and subcooled water boiling in the microchannels. Unlike in the previous numerical studies in the literature which presume a generated bubble at the beginning of the simulations or a pseudo-boiling in which bubbles are generated by the injection, in the present work, the boiling has been initiated from a cavity. The growth and departure of the nucleated bubbles from the cavity have been simulated. Hence, a complete simulation for nucleate boiling in a microchannel was illustrated. The code has been expanded to the microchannels with different size of cavities to simulate a preliminary model for the surface roughness.

Chapter 5 presents the manufacturing part of the study. The surface texture of the metal-based heat sinks has been the focus in this part. Manufacturing experiments with various process parameters have been conducted to create the different surface roughness values in the oxygen free copper micro-evaporator channels. The Taguchi method, a powerful experimental design tool, was used to find the optimum combination of specified process parameters. Analysis of variance has also been employed to analyze the significance of process parameters on surface roughness. An artificial neural network model has been utilized to assess the variation of the surface roughness with process parameters. The successful implementation of the process parameters to obtain the desired surface textures are also demonstrated by the optical microscope and SEM images of the fabricated microchannels.

In the experimental evaluation part, presented in chapter 6, the hydrodynamics and heat transfer performance of the three microchannel evaporators of the same dimensions and different surface roughness have been compared at variously imposed heat fluxes and mass fluxes. For this purpose, a microscale vapor compression refrigeration cycle has been constructed. The facility and instrumentation which include the two phase flow loop have been presented. R134a has been used as the refrigerant with boiling saturation temperature of 10°C at mass fluxes of 85 and 200 kg/(m^2·s).

In the first stage of the experimental works to evaluate the effect of surface roughness on evaporator performance, a conventional-scale condenser has been constructed and employed in the cycle. Then, a microscale condenser has also been constructed and tested. The overall performance of the micro-refrigeration cycle has been evaluated as well.

Finally, the conclusions and recommendations for the future work are given in chapter 7.

CHAPTER 2

BACKGROUND AND PRIOR RESEARCH

2.1 Two-Phase Flow Boiling

It is important firstly to consider the mechanisms by which boiling occurs. The processes of bubble nucleation, growth, and departure all affect the heat transfer from a surface.

2.1.1 Nucleation Theory

Nucleation is the process of vapor bubble formation where boiling heat transfer begins. Bubble nucleation can occur both in the bulk liquid - known as Homogeneous Nucleation, or at the interface between a liquid and the surfaces that contain it, known as Heterogeneous Nucleation. However, as homogeneous nucleation requires substantial superheat, heterogeneous nucleation is most commonly encountered at lower superheats [5]. Typically, heterogeneous nucleation occurs in small cavities on the surface, with a characteristic dimension of 0.1μm to 100 μm [5]. Here, vapor is trapped and serves to initiate bubble formation, as seen in Figure 2.1a. Because the bubble nucleation is seeded by stored vapor or air in the cavities, heterogeneous nucleation requires only a few degrees of superheat before the onset of nucleate boiling [6]. Heterogeneous bubble nucleation can also occur on a smooth surface, in the absence of a cavity. In this case, the energy required for nucleation becomes a function of the contact angle of the liquid on the surface. Contact angle, θ, is depicted in Figure 2.1b. This angle is a function of a surface's wettability and low contact angle corresponds to a high wettability.

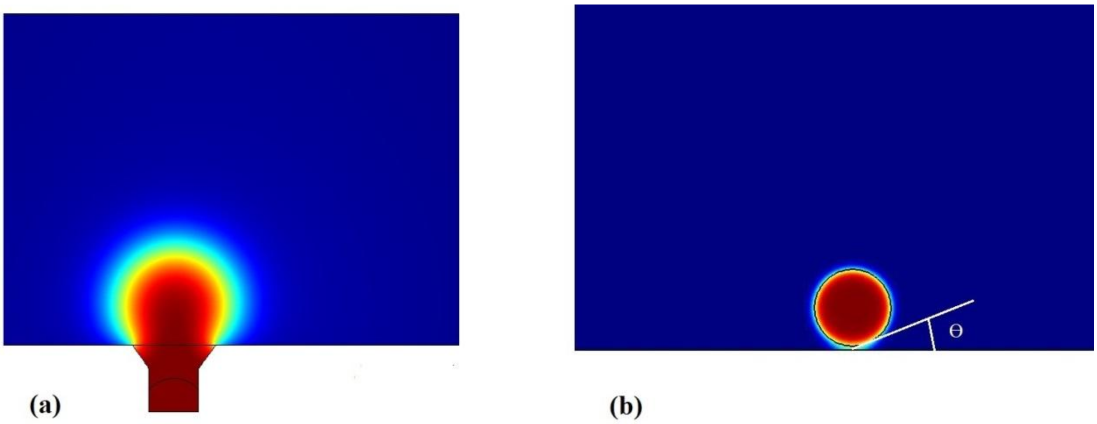

Figure 2.1 Heterogeneous bubble nucleation (a) from a cavity and (b) on a smooth surface

2.1.2 Critical Heat Flux and Heat Transfer Coefficient

Among the characteristics of a boiling flow, heat transfer coefficient and critical heat flux are the main concern. The critical heat flux (CHF) represents the operational limit of heat flux in the boiling heat transfer system because the transition from nucleate boiling to film boiling occurs when the heat flux exceeds CHF. In film boiling, the formation of a vapor film covers the heating surface completely. Liquid cannot contact the surface and, consequently, thermal resistance rises and heat transfer efficiency reduces.

The heat transfer coefficient (HTC) characterizes the system's ability to transfer heat by relating heat flux to the temperature difference between the surface and the bulk liquid. Both of these parameters illustrate a heat transfer system's capacity and performance.

2.2 Effective Surface Characteristics for Flow Boiling

Nucleate boiling is a complex phenomenon during which the liquid, vapor and wetted surface are in interaction. The heating surface condition is one of the parameters that have a significant influence on nucleate boiling heat transfer. It is directly related with the density of active nucleation locations on the heating surface and the cavity size distribution [7].

2.2.1 Surface Porosity

Surface porosity can enhance pool boiling heat transfer through a variety of hypothesized mechanisms. For example, porosity can increase the nucleation site density by creating cavities to seed bubble formation [8]. Moreover, the interconnection of the porous structure allows for transport of liquid between nucleation sites. Therefore, rewetting of nucleation sites is enabled, which can help delay CHF [9]. Finally, surface rewetting is further promoted through capillary action induced by the porous structure [8]. However, a porous layer can also have negative attributes. The porous structure can attract surface contaminant, accelerating fouling of the heat transfer surface. Moreover, the thickness of the layer also brings an additional thermal resistance to the heat transfer system. Therefore, it is necessary to balance the positive and negative consequences of a porous surface in a heat transfer system.

2.2.2 Surface Wettability

The contact angle is an important parameter in understanding bubble nucleation. A hydrophilic surface attracts water and can improve boiling performance through surface rewetting following bubble departure. On the other hand, a hydrophobic surface keeps away water and can be a disadvantage for boiling; however, hydrophobicity promotes bubble nucleation. Typically, 90˚ is considered neutrally wetting, with lesser angles being hydrophilic and greater angles being hydrophobic. Contact angle is primarily a function of surface chemistry, but other surface characteristics can also affect it. For example, roughness has the effect of making hydrophilic surfaces more hydrophilic and hydrophobic surfaces more hydrophobic.

2.2.3 Surface Roughness

In order to define the size range of active cavities as a function of wall temperature, heat flux, pressure of the system, subcooling and other physical properties, some models and correlations have been proposed [10,11,12,13]. The boiling experiments do not reveal the size distribution of potential nucleation cavities easily. Only the location of nucleation sites and the size of departed bubbles are observable. Another shortcoming is that typical standard parameters that are normally used to characterize roughness (R_a, R_z) are just statistical values. Their magnitudes depend on the size of the samples and the height of the measured roughness. In the other words, different area sizes of the same sample can return different roughness measurements. Also, samples with different cavity angles and radii but with statistically the same roughness height will return the same roughness value.

Roughening surface would promote pool boiling heat transfer. The increase in roughness would result in an increase in the number of bubble forming nuclei on the surface which results in a decrease in the surface temperature. Improvement of the heat transfer from the given surface of the same heat transfer area and wall superheat is usually desirable by investigating of surface conditions [14].

Various efforts have been spent to characterize the effects of surface roughness. Jones *et al.* [15] experimentally investigated the effect of surface roughness on pool boiling using water and FC-77. For water, a small increase in the heat transfer coefficient has been observed for low roughness values. On the other hand, a remarkable increase has been reported for the surface with R_a = 10 μm. With the same surface conditions, FC-77 yielded a continuous increase in the heat transfer coefficient with increasing roughness for the same heat flux. For FC-77, the heat transfer coefficient for the roughest surface was 210% more than that for the polished one. The corresponding enhancement was about 100% for the case of water.

2.3 Microchannel Heat Sinks

Microchannels are channels with small volume which have high surface to volume ratio. Therefore, microchannels could transfer a high rate of heat and mass that could be used in compact heat exchangers. Novel microchannel heat sinks have been employed to fabricate the microchannels as a part of the electronic circuitries by adding a few more steps to the standard CMOS fabrication flow [16].

2.3.1 Single Phase Flow in Microchannels

First time, Tuckerman and Pease studied single-phase flows in microchannels in 1981 [17]. Maximum heat flux of 790 W/cm^2 has been removed using silicon etched microchannels. A review study by Agostani *et al.* on single-phase microchannel heat sinks stated that, on the average, heat fluxes of 300 W/cm^2 can be removed with a heat sink unit with thermal resistance of 0.18 K·cm^2/W [18]. Optimizing the channel geometry and flow conditions can improve the results. Heat sinks with multilayered microchannels have been proposed by Wei *et al.* in which have proposed liquid overall thermal resistances as low as 0.09 K·cm^2/W [19]. Dissipation of high heat fluxes of 1 kW/cm^2 seems imaginable with enhanced microchannels from electronic circuits [20].

2.3.2 Two-Phase Flow in Microchannels

The vaporized bubble of microscopic size in a microchannel grows rapidly and fills the entire cross section of the microchannel in milliseconds, and eventually, an elongated bubble or slug flow appears in the microchannel [21].

The heat transfer coefficient in microchannels with single phase flow is quite high due to the small hydraulic diameter. Because of the coolant's latent heat, as well as the aid of slug flow, the heat transfer coefficient for flow boiling in microchannels is even higher. Additionally, the axial wall temperature maintains much uniform close to the coolant's saturation temperature. Even though flow boiling has these advantages in the microchannels, unstable operational conditions and the restrictive knowledge about the transport behavior are obstacles to the implementation of two phase in microchannels [22].

2.3.3 Microscale Refrigeration System

Microscale vapor compression refrigeration systems have been considered as ideal cooling systems in miniature scale for their several important advantages, including low mass flow rate, low cold plate temperature for long time, the ability to transport heat away from its source, high reliability and most importantly, high coefficient of performance (COP) and second law efficiency ($COP/COP_{reversible}$) [23]. There are two limitations for the development of a small scale refrigeration cycle; the compressor and the compactness of the heat exchangers. In addition, the size of the cooling package, the weight, and the pumping power are restrictions associated with small scale cooling technologies.

Table 2.1 shows some available experimental studies that implemented and tested miniature scale vapor compression refrigeration for cooling of microelectronic devices. As Table 2.1 shows, Yu-Ting *et al.* obtained maximum cooling capacity of 300 W; moreover, Wu and Du were able to reach up to a COP of 8.5. The theoretical limit for the COP in the study of Wu and Du [23] was $COP_{\text{reversible}} = \frac{1}{\frac{T_H}{T_L}-1} \cong 11$.

The COP values in Table 2.1 should be assessed with caution as the effects of the inclusion of pre- or post-heaters in the cycle are usually omitted or not mentioned in the literature.

Table 2.1 The characteristics of availabe micro refrigeration systems in the literature

Author	**Cooling Capacity (W)**	**Evaporating Temperature (°C)**	**Condensing Temperature (°C)**	**Refrigerant**	**Compressor**	**Condenser**	**Evaporator**	**Overall size of the system**	**Capillary tube**	**Efficiency**
Wu and Du [23]	100 200	20	45	R134a	Aspen Inc. 14-24-000X Dia.58 mm, Height 78 mm 2858 rpm	0.55×0.70×100 mm Wall Thickness 0.26 mm Channel No. 18 Overall Dim. 100×100×16 mm	0.5×4×57 Wall Th. 0.5 Channel No. 60 Overall Dim. 75×9×75	300×230×70 mm Refri. charge 100 g	Inner dia. 0.8 mm Length 1800 mm (1600-2000)	23% to 31% COP 8.5
Yu-Ting, *et al.* [24]	300	21.6	40	R22	Dia.50 mm × 70 mm 1650 rpm Shaft power 95 W	1.2 mm×1.2 mm Overall Dim. 130×140×16 mm Fin Height 8 mm	Spiral-tube Dia.4 mm Wall Thickness 0.75 mm Length 550 mm	260×250× 120 mm (2.85 Kg) Refri. Charge 100 g	Dia. 0.64 mm Length 1000 mm	COP 2.2
Trutass *et al.* [25]	150 - 250	10 -20	40 - 60 Refrigerant subcooling tem. at the outlet 3 -10	R134a	Hitachi XL0623D1 Dia.85mm, Length 166 mm	0.62×0.33 Overall Dim. 45×180×25 Inlet air 25,27,35°C	Al 0.8×2.3 mm No. 41 Model CP20G01	100 g (Micro motion model D6S-SS mass flow meter)	Hand operated needle valve	33% to 52%

Table 2.1 (continued)

Mongia *et al.* [26]	-	50 (Pressure 6.85 bar)	90 (Pressure 16.4 bar)	isobutane	-	Inlet air 50°C	0.30 mm × 0.7 mm No.21	0.26 g/s	Inner Dia. 0.4 mm 1100	COP > 2.25 25%- 30%

2.3.4 Techniques for Fabrication of Metal-Based Microchannels

Microchannel heat exchangers fabricated via metal-based manufacturing provide the desired enhancement in high heat transfer coefficients while preserving the required strength. Numerous metal-based microchannel fabrication techniques exist, and there is not a well-established standard in these.

Among the microfabrication techniques micromilling has been employed for complicated 3-D geometries [27-30]. Tools with diameters as low as 50 μm are commercially available while smaller ones may be custom made. This procedure is suitable for use in CNC machines.

Machining with pulsed lasers has been used as a non-contact machining method [31]. About 1μm material removal per pulse with a 10 μm diameter laser beam has been reported [32]. If the surface quality is a concern in the application, further treatment may be necessary in this procedure.

Electro discharge machining (EDM) which can be used for electrically conducting materials are recently used to obtain microstructures [33]. Machining with sinker tool or wire have been used [34]. Micro EDM is a non-contact procedure and enables carving microscale patterns brittle materials. Though the surface roughness is relatively high in micro EDM, the increased roughness may be desired for applications such as boiling heat transfer.

Powder blasting may be listed as another micromachining process where micro abrasives are utilized for etching micro shapes of 100 μm or less in size. With the use of a mask, very difficult patterns can be obtained [35].

Harvinder lal *et al.* compared the surface roughness and machining time achieved using three different micro machining processes, namely, micromilling, slotting saw and wire-cut EDM. The results showed that the surface finish of the microchannel fabricated with wire-cut EDM (surface roughness 1.20-6.90 μm) was observed to be superior than the one made using micromilling (4.12-10.20 μm), followed by that using slotting saw (12.8-20.80 μm). It was observed that the surface roughness value even vary from channel to channel, as the tool/wire will wear as the machining time increases. Moreover, micromilling has the intermediate surface finish due to machining time [36]. Mohammad Yeakub Ali compared the fabrication of

microfluidic channels using micromilling and micro EDM. The size of the microchannels produced by micromilling are 500-800 μm, whereas 100 μm width with aspect ratio of 8 is produced by micro EDM; also very high surface finish (40 nm R_a) achieved with micro EDM machining while the roughness was 100-200 nm for micromilling. Machining of deeper channels with high dimensional accuracy needs layer by layer material removing by thickness of 100-200 μm for micromilling. Burrs are formed at the edges of the microchannels in micromilling that need to be removed by deburring process [37]. Bin Lu *et al*. fabricated microchannels from Cu110 alloy sheets (41 mm × 41 mm × 1.2 mm base sheet and 41 mm × 41 mm × 0.5 mm cover sheet dimensions) by micro EDM. Blade electrodes were selected from different thicknesses of flat carbon steel sheets. An aluminum thin foil (25 μm in thickness) used as an intermediate layer to bond Cu sheets. For bonding, an MTS858 single-axis mechanical testing system was used together with a vacuum chamber and heaters [38].
Some studies which fabricated metal based microchannels by micro EDM and micromilling methods are illustrated in Table 2.2.

Mohamad Yeahuab Ali has made microchannels with aspect ratio of 8 by Micro EDM. In these studies the cross section of the microchannels was rectangular. Fabricating of trapezius and semicircular cross section is also possible by employing EDM machining.

Table 2.2 Manufacturing methods and their parameters for metal based microchannels

Author	Microchannel Dimension (mm)	Method	Material	Tool	Accuracy	Surface Roughness
Vázquez *et al.* (2010) [39]	Width: 0.2 Height : 0.05 and 0.1	Milling (Deckel-Maho© 64V Linear)	Al (21HRB) Cu (72HRB)	Mitsubishi© MS2SSD0020 CRNMSD0020S04		Al: 1.71 µm dry. 0.72 µm wet Cu: 1.507 µm dry. 1.314 wet (Min.)
Harvinder lal *et al.* (2012) [36]	Width : 0.3,0.5,0.6 Height: 2	Wirecut EDM Slotting Saw Micromilling	Al	-Sodick Technologies India Private Limited, Model:AG600L-JP-M2 Universal Milling Machine-Long Reach Mini 2 Flute Micro Mills Z72010 and Z72020		1.20-6.90 µm 12.8-20.8 µm 4.12-10.20 µm
Yeahuab Ali (2009) [37]	Width : 0.5, 0.8 Aspect ratio 1-2 width : 0.12 depth Aspect 1 ratio >8	Micromilling MicroEDM DT-110: Mikrotools Inc. Singapore	Beryllium Copper Alloy	Tungsten Carbide	<1 µm <1µm	180 nm 100 nm 40nm
Lu *et al.* (2010) [38]	Width: 0.183, 0.209, 0.301, 0.540, 0.186 Height: 0.660, 0.609, 0.660, 0.670, 0.636 (70,52,35 channels)	Micro EDM	Cu110 (99%Cu)	Flat carbon steel sheet		
Iwatsuka *et al.* (2012) [40]	Tools Dia. 0.05, 0.1 and 0.5	TG-10A WAIDA Micromilling	SUS316	Carbide 2NT Hitachi		
Woo-Chul Jung *et al.*	Width: 0.200 and 0.400	Micromilling DMU 100T	NAK80 (age-	Tungsten Carbide	Dia. 0.4 has better	R_a = 31 nm, R_a = 44 nm for

Table2.2 (continued)

(2007) [41]	Height: 0.100	hardened mold steel)	shape accuracy than 0.2	curved region
Jang and Bang (2010) [35]	Width: 0.8 Height: 0.3	Steel 316L	Dimension error 0.2	R_a = 0.06-0.08 µm

2.3.5 Surface Roughness Parameters and Related Studies in Flow Boiling in Microchannels

Surface roughness parameters are extensive. Each of these parameters determines a specific property of the surface and it could be the most important for the particular application. The actual surface geometry is so complex that just a few of the parameters cannot characterize a full specification of the surface. Augmentation in the number of parameters results in more accurate description.

Surface roughness parameters generally are categorized into three groups according to its functionality. These groups are defined as amplitude parameters, spacing parameters, and hybrid parameters [42]. Amplitude parameters represent the measurement of the vertical characteristics of the surface deviations. The most universally used roughness parameters are:

- Arithmetical average height (R_a): mean of the absolute ordinate values within a sampling length;

- Ten point height (R_z): The difference in height between the average of the five highest peaks and five lowest valleys along the assessment length of the profile;

- Maximum depth of valleys (R_v): The maximum depth of the profile below the mean line within the assessment length.

Spacing parameters measure the horizontal characteristics of the surface deviations. One of the spacing parameters is mean spacing at mean line (S_m). It defines the mean spacing between profile peaks, the highest point of the profile between upwards and downwards crossing the mean line, at the mean line.

Any changes in either amplitude or spacing can affect the hybrid parameter. In tribology analysis, surface slope, surface curvature and developed interfacial area are considered as important factors of hybrid parameters.

Limited studies are available in the literature which investigate surface characteristics on flow boiling in microchannels.

Jones and Garimella [43] conducted experiments on three microchannel heat sinks with different surface roughness (R_a=1.4 μm, 3.9 μm and 6.7 μm) to compare flow boiling heat transfer and pressure drops. They used deionized water as the coolant. The results show that the surface roughness has not a significant influence on the boiling incipience wall temperature. Furthermore, the saturated boiling heat transfer coefficient for wall heat fluxes below 700 kW/m^2, have a slight differences among the test surfaces. The heat transfer coefficients for heat fluxes above 1500 kW/m^2 have increased 20-35% for surfaces with R_a= 3.9 μm and 6.7 μm compared to those for the surface with R_a= 1.4 μm. The pressure drop measurement depicts that the surface with R_a= 6.7 μm has the drawback of increased pressure drop compared with the surfaces with R_a= 1.4 μm and 3.8 μm.

Some researchers have studied the enhanced surfaces in minichannels and microchannels. Kuo and Peles [44] investigated flow boiling in microchannels with structured reentrant cavities. The enhanced microchannel significantly reduced in the wall superheat required to initiate boiling compared to the plain-wall microchannels. A review by Honda and Wei [45] investigated boiling heat transfer from electronic components immersed in dielectric liquids by the use of surface microstructures. The boiling curves with different surface roughness revealed that the surface roughness enhances nucleate boiling but the heat transfer performance is not directly related to R_a. A new study [46] shows super hydrophilic Si nanowires at inner walls of the microchannel enhances the heat transfer performance extremely, compared to plain-wall microchannel. It promotes thin film evaporation and liquid film renewals over the entire microchannels. The heat transfer coefficient and CHF have increased up to 326% and 317% at a mass flux of 389 kg/m^2·K, respectively.

Chu [47] demonstrated heat transfer performance of microstructured surfaces integrated, silicon micropillars with height of 25 μm, diameter of 5-10 μm and spacing of 5-10 μm, into microchannels of 500 μm×500 μm. The primary results showed the heat flux of 508 W/cm^2 with mass flux of 1530 $kg/m^2 \cdot s$ could be dissipated.

2.4 Experimental and Numerical Studies for Flow Boiling in Microchannels

Vaporized bubble of microscopic size in a microchannel grows rapidly and fills the entire cross section of the microchannel in milliseconds, and eventually, an elongated bubble or slug flow appears in the microchannel. Moreover, at the microscale, the surface tension and evaporation momentum forces are the dominant forces controlling the bubble dynamics [48]. Accordingly, the models and correlations developed for macroscale boiling heat transfer may not be applicable for microscale two phase flows.

2.4.1 Experimental Studies to Investigate the Flow Boiling in Microchannels

Lee and Mudawar [49,50] performed experiments to explore the heat transfer characteristics of a microchannel heat sink employed as an evaporator in a refrigeration cycle. Microchannels with 53 μm and 231 μm wide and 713 μm deep with micro slots carved into the 25.3 × 25.3 mm^2 top surface of an oxygen-free copper block have been used. New correlations for microchannel flow were developed based on the flow visualization studies at different quality values along with heat transfer coefficient and pressure data that were validated for R134a and water. It was concluded that two-phase heat transfer in microchannel heat sinks is related with the quality of flow. Different mechanisms dominate for low, medium and high quality flows. When very low heat fluxes were imposed bubbly flow and nucleate boiling occur only at low qualities ($x < 0.05$). High fluxes produce medium quality ($0.05 < x < 0.55$) or high quality ($0.55 < x < 1.0$) flows depending on flow rate. The results indicated remarkable differences in heat transfer mechanisms among the three quality regions. Then the quality range must be divided into smaller ranges to obtain much more precise correlations considering the flow transitions.

Revellin and Thome [51] illustrated four principal flow patterns (bubbly flow, slug flow, semi-annular flow and annular flow) with their transitions (bubbly/slug flow and slug/semi-annular flow) with R-134a and R- 245fa in 0.50 mm and 0.80 mm circular channels. As the mass flux increases the transitions occur at lower qualities. Since small bubbles quickly coalesce to form elongated ones, the bubbly flow turns in to slug flow. The observations revealed that two phase flow pattern transitions with R-134a did not match well to prior macroscale flow map for refrigerants. Also, the obtained patterns are not similar to those in microscale air–water flows. The flow pattern transitions are not significantly affected by the inlet subcooling, the saturation pressure and the diameter of the channel. Although, the two-phase flow transitions for R245fa and R134a are quite the same, variation of the transitions between flow regimes due to the mass flux for R-245fa is less than that for R-134a.

Agostini *et al.* [52] reported that heat transfer behaves in three different ways for refrigerant R236fa boiling in a silicon microchannel heat sink. Large ranges of heat fluxes, mass velocities and vapor qualities have been adjusted. The heat transfer coefficient increased with vapor quality at low heat fluxes. It increased with the heat flux at medium heat fluxes whereas it decreases at very high heat fluxes. This later trend may be is due to alternating dryout before reaching CHF. The results have a significant difference comparing the macroscale flow boiling. These results contrast significantly with macroscale flow boiling trends, specially, the absence of the convective boiling regime in the microchannels.

Bertsch *et al.* [53] measured the local flow boiling heat transfer coefficient of refrigerant HFC-134a in a copper microchannel evaporator. The low mass fluxes of 20.3 to 81.0 kg/m^2·s, vapor qualities of 0 to 0.8 at pressures of 400–750 kPa were varied. The heat transfer coefficient rose significantly with refrigerant quality up to 0.2 then dropped. The influence of saturation pressure on the heat transfer coefficient was almost negligible. The heat flux enhanced strongly the heat transfer coefficient as reported in the previous studies. It is in contrast to those obtained for the macro scale.

Costa-Party *et al.* [54] studied flow boiling of R236fa and R245fa in a 12.7 mm silicon evaporator with 135 microchannels of 85 μm width and 560 μm height and 46 μm fin thickness. The heat transfer results were uniform in the lateral direction to the flow and a function of the heat flux, vapor quality and mass flux. For wall heat fluxes over 45 kW/m^2, the heat transfer coefficient curves were V-shaped, decreasing for intermittent flow regimes and increasing for annular flow.

2.4.2 Numerical Methods to Simulate the Flow boiling in Microchannels

The experimental efforts are limited due to the small scales, while multiphase CFD techniques are emerging as powerful tools to investigate the fluid dynamics and the heat transfer at such scales.

Zu *et al.* [55] performed a 3-D numerical simulation of bubble formation using the volume of fluid (VOF) method in the commercial CFD software ANSYS FLUENT. In the mentioned study, the bubble generation and growth were simulated based on the concept of pseudo-boiling in which the bubble is generated by the injection of vapor from a hole through the heated side wall of the channel. The hole served as a nucleation site, and the bubble growth was then driven by a constant heat flux.

Dong *et al.* [56] investigated the effect of bubble nucleation, growth and departure on fluid flow and heat transfer in a microchannel via lattice Boltzmann 2-D modeling. A single seed bubble, a cavity, two cavities, one seed bubble and a reentrant cavity were simulated in a microchannel with dimensions of 0.2 mm×5.3 mm.

Sun *et al.* [57] proposed a vapor-liquid phase model in ANSYS FLUENT which considers both superheated and saturated phases. The vapor near the wall got heated and became superheated, which drove the mass transfer at the interface. The vapor stayed motionless while the saturated liquid and the interface were driven away from the wall.

Magnini *et al.* [58] implemented ANSYS FLUENT to investigate in detail the bubble dynamics and the wall heat transfer of flow boiling in a circular microchannel of diameter 0.5 mm. Different refrigerants, namely, R113, R134a and R245fa were investigated with two different saturation temperatures of 31°C and 50°C. The bubble nose acceleration to downstream was in good agreement with a theoretical model [59].

Mukherjee *et al.* [60] studied a vapor bubble growing on a heated wall inside a microchannel with a hydraulic diameter of 229 μm. They solved the continuity, Navier-Stokes and energy equations using the SIMPLER algorithm. Firstly, the water bubble growth rate and the bubble shape were validated by experimental results. Then a parametric numerical study was carried out to analyze the effects of the wall superheat, the inlet liquid flow rate, the surface tension and the contact angle on the bubble growth rate inside the microchannel.

Lee and Son [61] used the level set method along with the phase change and contact angle to study numerically the bubble dynamics and heat transfer during nucleate boiling in a microchannel. By decreasing the channel size to bubble diameter ratio, the bubble growth rate and the heat transfer increased significantly. The heat transfer also increased by the decreasing contact angle.

Zhou *et al.* [62] used the level set two-phase flow model to simulate the nucleate boiling in microchannels. The model for the bubbles in uniformly superheated liquid, and flow boiling regime were identified and validated. Reentrant cavities were formed along the microchannel to compare the performances of the enhanced and plain-wall microchannels. The results demonstrated facilitated nucleation and enhanced critical heat flux. The reentrants were optimized based on which nucleates first under a given set of conditions of rather low superheating.
Akhlaghi Amiri and Hamouda [63] compared the accuracy and running time of two-phase flow through porous media by 2D modeling with conservative level set method (LSM) and Cahn–Hilliard phase-field method (PFM) in COMSOL Multiphysics. It was concluded that the PFM is more successful in capturing physical details. Furthermore, the PFM results, such as, the pressure gradients and the flow profiles in the media were more realistic than those for the LSM and it took less running time for the PFM method. Besides, the LSM needed a thinner interface for convergence compared to the PFM and was unsuccessful in the volume conservation and no slip boundary conditions.

2.5 Contribution of the Present Study

This study employs two numerical methods, arbitrary Lagrangian-Eulerian method and phase-field method to simulate the nucleate boiling in the microchannels. The growth and departure of the nucleated bubbles from the cavity are simulated, for the first time in the literature. Another original contribution is that the effects of the surface roughness on flow boiling of the refrigerant R134a are investigated experimentally in the microchannels. Up to 45% enhancement in two-phase heat transfer coefficient has been achieved by increasing the surface roughness at low to moderate heat flux values.

CHAPTER 3

NUMERICAL MODEL 1: ARBITRARY LAGRANGIAN-EULERIAN METHOD

In this chapter the arbitrary Lagrangian- Eulerian method (ALE) is used to model the hydrodynamics and the heat transfer of an elongated vaporized bubble in a microtube. The Navier-Stokes equations along the energy equation are solved in ALE description as a single fluid with two subdomains and a moving mesh at the interface of the liquid and vapor phases. The numerical framework is the commercial CFD code COMSOL Multiphysics with the finite element method, which has been improved by external functions to the phase changing. In the simulations, the nucleated bubble comes in contact with superheated water and starts growing. The growth rate of the bubble in the proposed model and the thin liquid film between the elongated bubble and the channel wall are in a very good agreement with the analytical solution and the correlation in the literature, respectively. The interactive effects of two elongated bubbles also are presented [64,65].

3.1 Arbitrary Lagrangian-Eulerian Method

The numerical simulation of two phase flow with phase change often requires dealing with strong distortions of the continuum while there are free surfaces, fluid–fluid and fluid–solid interfaces. The two classical descriptions of motion, namely the Lagrangian and the Eulerian descriptions are usually used in the continuum mechanics. In Lagrangian formulation each individual node of the computational mesh follows the associated material particle during motion. Then it is easy to track the free surfaces and the interfaces between different materials. That denotes a significant advantage in problems involving materials with historical dependent behavior. On the other hand the large distortion of the computational domain loses in accuracy, and may even be unable to conclude a calculation. In Eulerian formulation the computational mesh is fixed and the continuum moves with respect to the grid. The large distortions of the computational domain are easily attainable but generally at the expense of precise interface definition and the resolution of flow details.

Due to the shortcomings of purely Lagrangian and purely Eulerian formulations, the arbitrary Lagrangian-Eulerian (ALE) description has been developed that succeeds in combining the best features i.e. greater distortions of the continuum with more resolution than both of the Lagrangian and the Eulerian approaches. The nodes of the computational mesh may be moved with the continuum in Lagrangian method, or be fixed in Eulerian method or be moved in some arbitrarily specified way [66].

3.2 Domain Equations and Boundary Conditions

Two phase flow with moving mesh interface is a predefined physics coupling between the single flow and the moving mesh method. The whole flow fills a domain. The domain is decomposed into two subdomains filled with the individual phases. Within the domains corresponding to individual phases the fluid flow is solved using the governing equations, namely, momentum and conservation of mass and energy over the whole domain. The Navier-Stokes equations for an incompressible flow are written:

$$\frac{\partial \rho}{\partial t} + \nabla \cdot \; \rho u \; = 0 \tag{3.1}$$

$$\rho \frac{\partial u}{\partial t} + \rho \; u \cdot \nabla \; u = \nabla \cdot \; -pI + \tau \; + F \tag{3.2}$$

where ρ, u, p, F and τ are density [kg/m^3], velocity vector [m/s], pressure [Pa], volume force vector [N/m^3] and the viscous stress tensor, respectively.

For a Newtonian fluid the viscous stress tensor, τ, is given by

$$\tau = 2\mu S - \frac{2}{3}\mu \ \nabla \cdot u \ I \tag{3.3}$$

The dynamic viscosity μ [Pa·s] is allowed to depend on the thermodynamic state but not on the velocity field.

The energy equation is written in the general form of

$$\rho C_P \frac{\partial T}{\partial t} + \rho C_P \ u \cdot \nabla \ T = \nabla \cdot k\nabla T \tag{3.4}$$

In this equation, *Cp* [J/kg·K] and *k* [W/m·K] are the specific heat and the thermal conductivity, respectively.

We assume that without the phase change at the interface, *S*, fluid velocities on both sides of the interface are the same as

$$u_1 = u_2 \tag{3.5}$$

Then the interface velocity will be equal to the normal velocity, the same on both sides of the interface:

$$V = u_1 \cdot n = u_2 \cdot n \tag{3.6}$$

where *V* and *n* are the normal velocity on each point of *S* and the unit normal to the interface, respectively.

If the phase change occurs at the interface, the mass will transfer from one phase to another. To connect the mass flow to the velocities on both sides of the interface we consider the frame of reference where the interface is at rest. The normal velocities in that frame of reference are [67]

$$u' = u \cdot n - V \tag{3.7}$$

The amount of mass, M_f [kg/m^2·s], which is transferred from phase *1* to phase *2* must be the same on both sides of the interface (conservation of mass)

$$\rho_1 u'_1 = \rho_2 u'_2 = M_f \tag{3.8}$$

Then, in the general frame of reference

$$\rho_1(u_1 \cdot n - V) = \rho_2 \;\; u_2 \cdot n - V \;\;\; = M_f \tag{3.9}$$

Hence, if there is no phase change, i.e. $M_f = 0$, Equation (3.6) is retrieved.
Then the boundary conditions applied at an interface between two immiscible fluids, fluid 1 and fluid 2 are given as

$$u_1 = u_2 + (\frac{1}{\rho_1} - \frac{1}{\rho_2}) M_f n_i \tag{3.10}$$

$$u_{mesh} = (u_1 \cdot n_i - \frac{M_f}{\rho_1}) n_i \tag{3.11}$$

$$\mathrm{n_i} \cdot \tau_2 = \mathrm{n_i} \cdot \tau_1 + \mathrm{f_{st}} \tag{3.12}$$

where u_{mesh} is the velocity of the mesh at the interface between the two fluids, τ_1 and τ_2 are the total stress tensors in domains 1 and 2 respectively and f_{st} is the force per unit area due to the surface tension.
The mass flow for evaporation can be evaluated from the conductive heat flux as:

$$M_f = C \rho_L \frac{T - T_{sat}}{T_{sat}} \tag{3.13}$$

C is set to be 0.1 [m/s] as in the literature [68].
To obtain additional insight into the boundary condition, it is helpful to re-write Equation (3.7) as

$$n\cdot\left[(p_1-p_2)I-\mu_1\left(\nabla u_1-(\nabla u_1)^T\right)+\mu_2\left(\nabla u_2-(\nabla u_2)^T\right)\right]=\sigma(\nabla_s\cdot n)n-\nabla_s\sigma \quad (3.15)$$

where ∇_s is the surface gradient operator ($\nabla_s=(I-nn^T)\nabla$) where I is the identity matrix and σ is the surface tension at the interface. Assuming Newtonian fluids with viscosities μ_1 and μ_2 for fluids 1 and 2 respectively and that p_1 and p_2 are the pressures in the respective fluids adjacent to the boundary. This equation expresses the equality of two vector quantities.

The heat generated from the transformation of the liquid to the vapor is applied to the boundary condition at the interface as

$$-n\cdot(-k\nabla T)=M_f h_{lg} \quad (3.16)$$

where h_{lg} [J/kg] is the latent heat.

3.3 Validation of the Model

For the validation of the model, it is assumed that a spherical vapor bubble of radius 10 μm has been placed at the center of the superheated water of infinite medium. The temperature of the bubble is set to the saturation temperature. COMSOL Multiphysics™, the commercial finite element software, has been employed for the simulation.

All the walls have been set as an outflow condition in which the pressure and the temperature have been set at the atmospheric pressure and the superheated temperature, respectively.

The growing rate of the vapor bubble has been validated by the analytical solution in the literature [69]. Figure 3.1 compares the bubble growth rates obtained by the present simulation and the analytical procedure which is calculated as

$$R=2\beta\sqrt{\frac{k}{\rho C_L}t} \quad (3.17)$$

where β is

$$\beta = \sqrt{\frac{3}{\pi}} \frac{\Delta T}{\frac{\rho_G}{\rho_L}\frac{h_{lg}}{C_{pL}} + \frac{C_{pL} - C_{pG}}{C_{pL}}\Delta T} \tag{3.18}$$

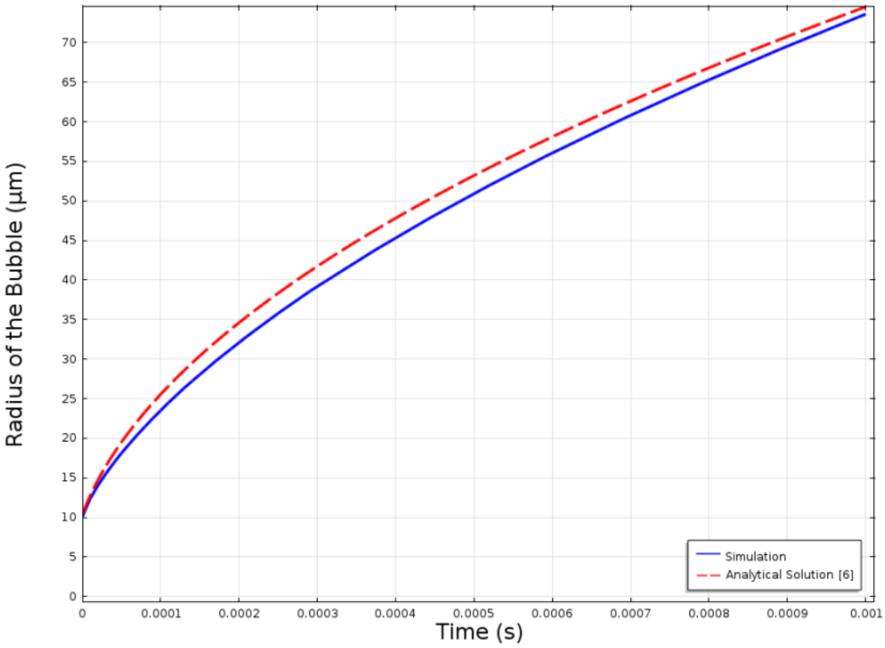

Figure 3.1 The comparison of the bubble growth rates of the simulation and the analytical solution

It can be seen that the numerical model for the growth of the vapor bubble is in good agreement with the analytical solution.

3.4 Simulation of the Nucleated Bubble in the Microtube

For analyzing the local hydrodynamics and heat transfer of the vapor bubble inside the microchannel in detail, it is assumed that a bubble of 10 μm diameter starts growing in a microchannel of 200 μm diameter. The water inlet and initial temperatures, and the wall temperature are set to 102$°C$ and the initial temperature of the bubble is 100°C (saturation temperature). This way, the effect of convective heat transfer between the wall and water has been eliminated. Only the boiling heat transfer effect is maintained. It should be noted that this excess temperature needed for bubble nucleation is based on available microchannel experiments. Water flows through the microchannel with Reynolds number *Re* = 69 at saturation temperature. The wall is no-slip. The simulations were performed in two dimensional axisymmetric space to save computational power and time.

3.5 Results and Discussions of the Simulation for Single Bubble and Two Successive Bubbles

Figure 3.2 shows the time based growth of the bubble in the microchannel. The bubble elongates, and eventually the diameter of the bubble increases up to the diameter of the microchannel. Figure 3.3 depicts the mesh distribution in the microchannel during the simulation. The maximum element size in the domain 1 (inside the bubble) and domain 2 (outside the bubble) are 0.5 μm and 3 μm, respectively (Figure 3.3a). In Figure 3.3b the deformation of the grids can be seen in the close up view. Figure 3.3c shows the remeshed distribution of the grids at the same time.

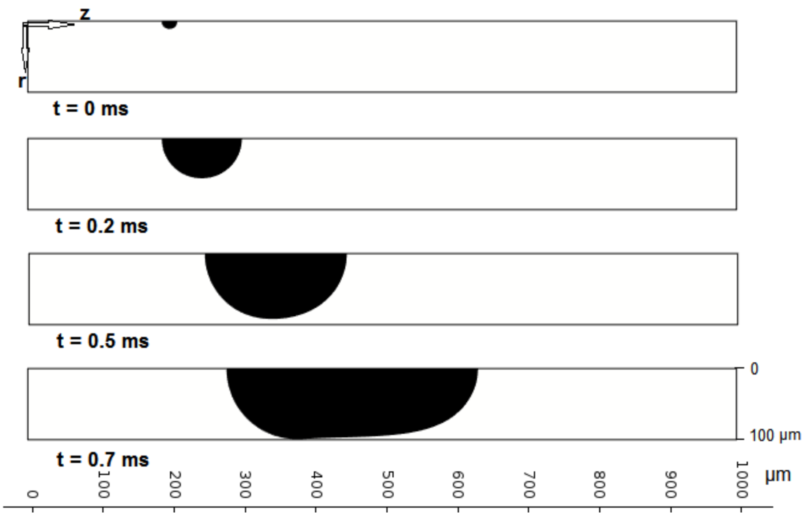

Figure 3.2 The bubble growth in the microtube

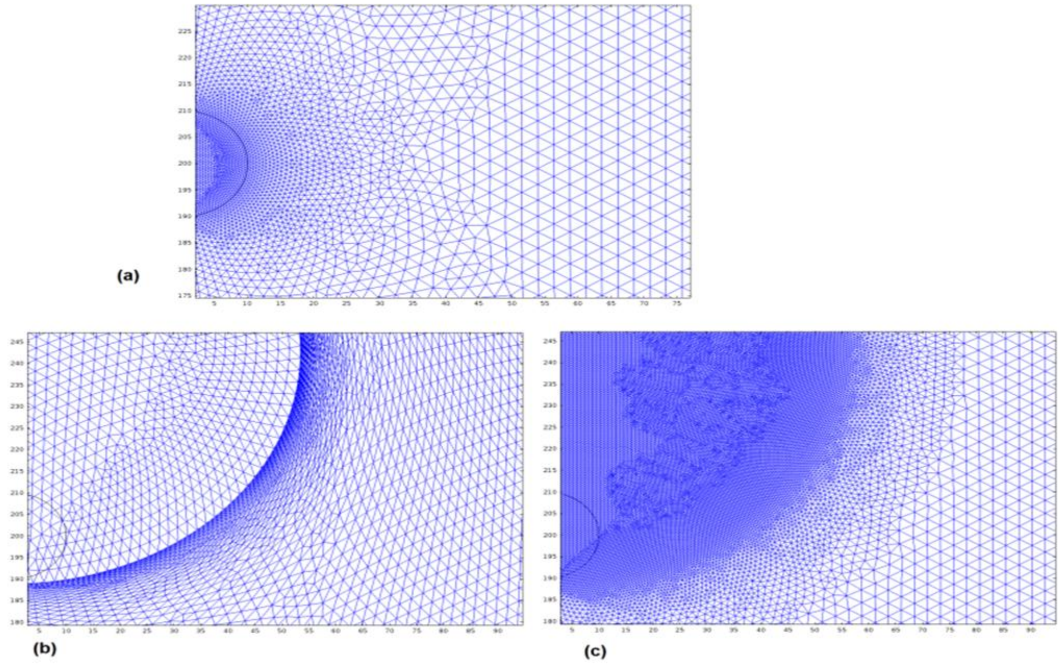

Figure 3.3 (a) Grid distribution at the initial time (b) deformed mesh at t = 0.19 ms and (c) remeshed grids at t = 0.19 ms

Figure 3.4 illustrates the velocity distribution inside and around the elongated bubble. The downstream velocity increases whereas the upstream velocity remains low at about 0.1 m/s. It may be inferred that the liquid is pushed forward at a faster rate downstream due to the bubble growth.

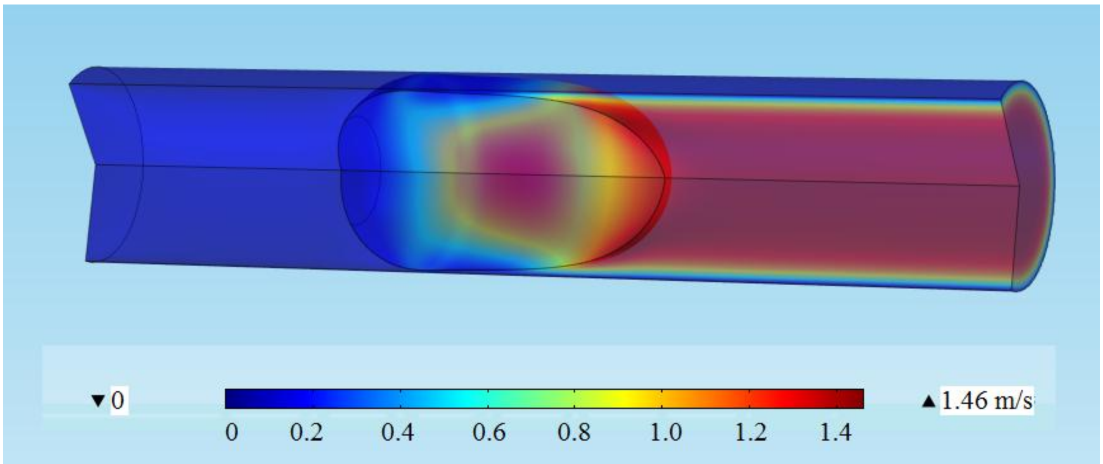

Figure 3.4 Velocity distribution at t = 0.7 ms

The thickness of the liquid film left behind the elongated bubble would be predicted by the empirical correlation provided in [70] as

$$\frac{h}{r} = \frac{1.34Ca^{2/3}}{1 + 1.34\ \times 2.5Ca^{2/3}} \tag{3.19}$$

where h is the remaining thickness of the liquid film, r is radius of the microtube and Ca is the capillary number.

Corresponding to the velocity of the bubble at the thinnest part of the liquid film, u = 0.375 *m/s*, and radius of the microtube, r = 100 µm, h is estimated as 1.86 µm by Equation (3.19).

h is found as 1.79 µm from the simulations which is in good accordance with the foregoing prediction.

Figure 3.5 shows the temperature distribution inside and around the elongated vapor bubble. The temperature inside the bubble remains at the saturation temperature due to the thin saturated liquid film between the bubble and the side walls.

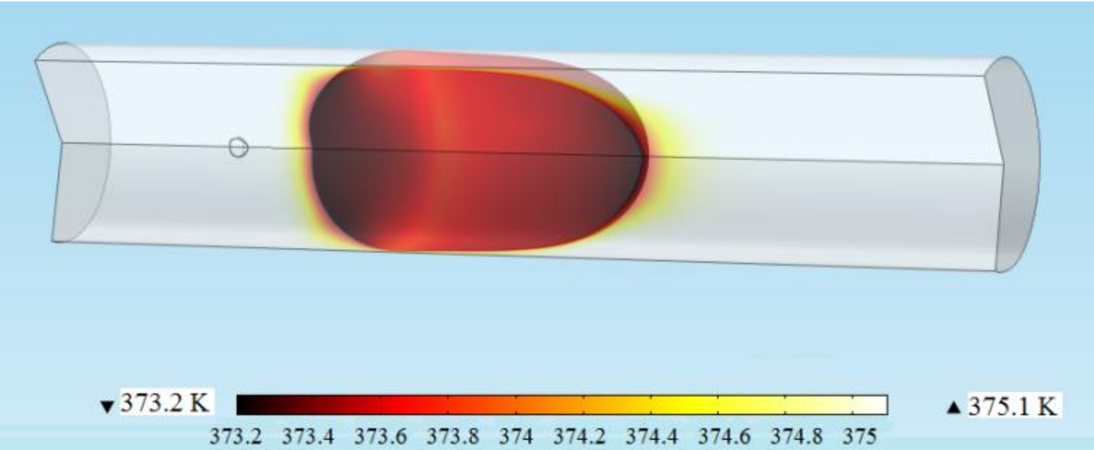

Figure 3.5 Temperature distribution inside and around the vapor bubble at t = 0.7 ms

As the bubble grows into an elongated one, the temperature gradient increases in the thermal boundary layer developed on the wall. This increases the local heat flux as well. Figure 3.6 demonstrates the local heat transfer coefficient along the wall of the microchannel at t = 0.7 ms. It is observed that the evaporation heat transfer coefficient increases to 220 kW/m^2 ·K at L = 400 μm, where the thickness of the thin liquid layer between the bubble and the wall is the smallest. Since the liquid and the wall are at the same temperature (102˚C), there is no temperature gradient from the wall to the liquid. Hence the local heat transfer coefficient remains zero.

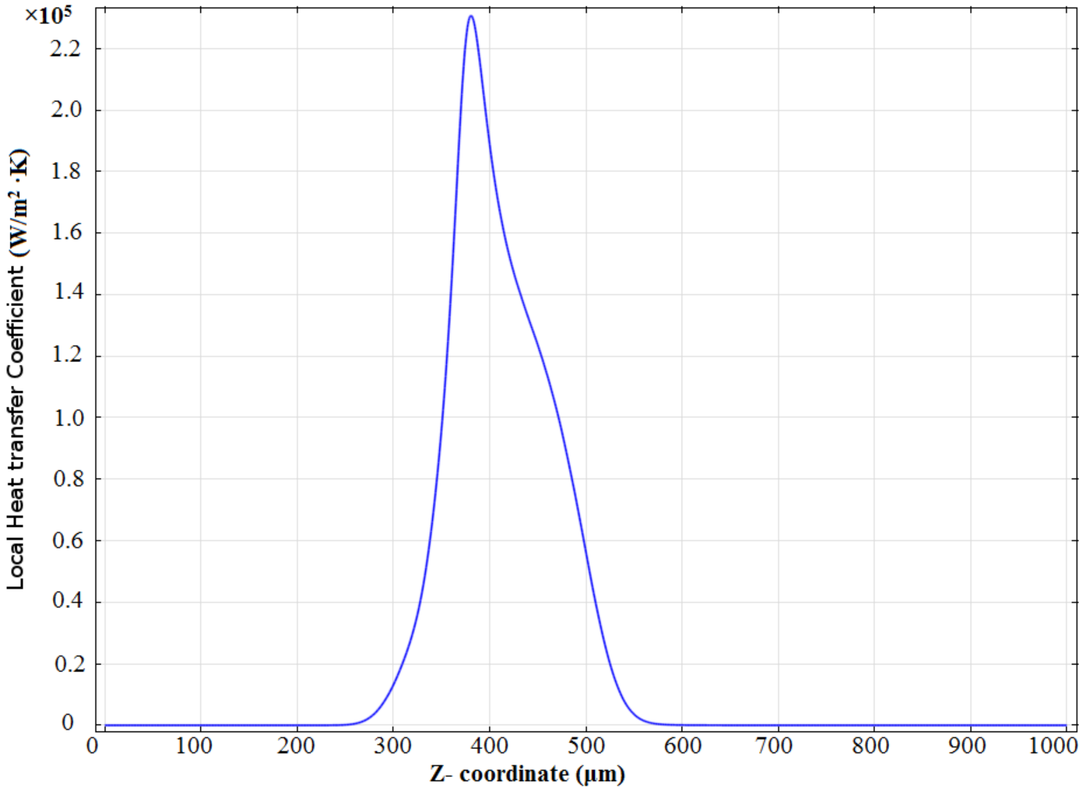

Figure 3.6 Local heat transfer coefficient along the wall of the microchannel for elongated bubble at t = 0.7 ms

The pressure distribution inside the microchannel at various time steps is shown in Figure 3.7. As the bubble expands, the pressure of the vapor decreases gradually until the bubble touches the tube wall. The pressure at t = 0.1 ms is about 105 kPa which reduces to 103 kPa at t = 0.5 ms. It reaches a stable value of about 104 kPa when the bubble starts to elongate. The maximum pressure difference between the upstream and downstream of the bubble is less than 500 *Pa*. However, when the diameter of the bubble reaches the diameter of the microchannel the pressure difference increases up to 2 kPa.

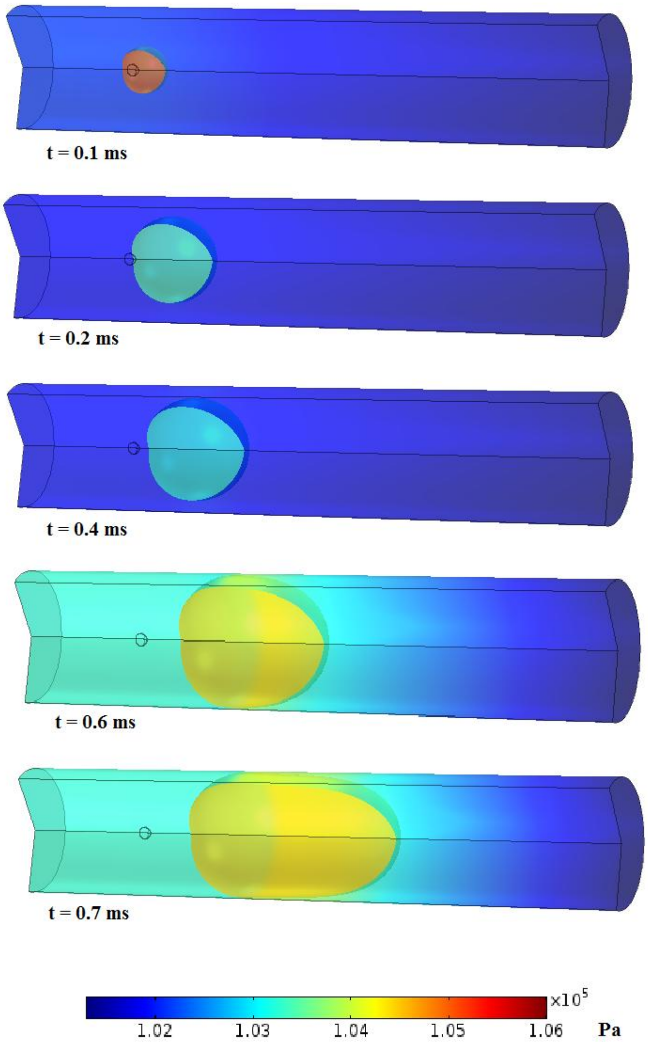

Figure 3.7 Pressure distribution at different time steps

To investigate the interactive effects of the bubbles in a microchannel, it is presumed that two nucleated bubbles with diameters of 10 μm have been placed at an arbitrarily chosen 400 μm far from each other along the channel.

Figure 3.8 demonstrates the velocity, pressure and temperature distributions inside the microtube at t = 57 ms.

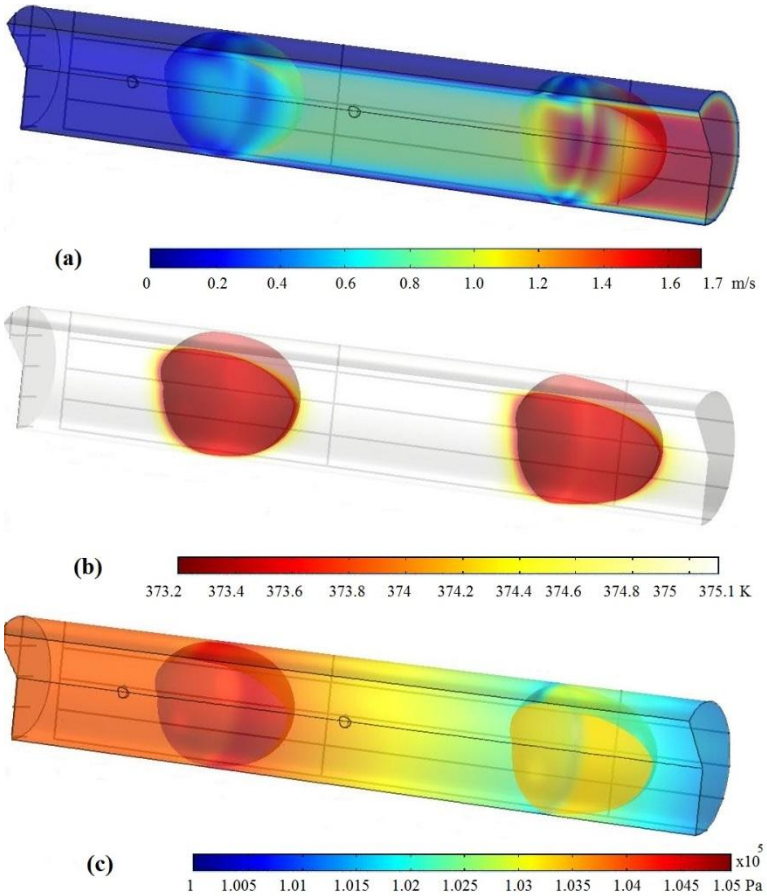

Figure 3.8 (a) Velocity distribution, (b) temperature distribution, and (c) pressure distribution of two elongated bubbles in the microtube at t = 0.57 ms

It may be observed from Figure 3.8a that the accelerated slug liquid by the trailing bubble pushes the rear of the leading bubble, and the leading bubble moves with a higher velocity than the trailing bubble. Hence, the dynamics of the leading bubble is affected by the trailing bubble.

Figure 3.8b illustrates the temperature distribution inside the microtube. As in the case for a single bubble, the vapor temperature always remains very close to the saturation temperature. The transit of the evaporating leading bubble changes the thermal boundary layer some tens of micrometers. However, it does not affect the trailing bubble thermally, due to the long length of the slug liquid between the bubbles.

It may be inferred from Figure 3.8c that the pressure difference between the inlet and the outlet of the microtube with two elongated bubbles remains around 2 kPa, the same as that for a single bubble. The leading bubble takes act as a moving obstacle for the trailing bubble. Furthermore, the trailing bubble is located at the upstream of the leading bubble which has higher pressure than the downstream. Then the pressure inside the trailing bubble becomes about 1.5 kPa more than that in the leading bubble.

Heterogeneous nucleation occurs in small cavities on surfaces which leads to flow boiling in microchannels. The size ranges of active cavities may be demonstrated by surface roughness parameters. To achieve this goal, the Arbitrary Lagrangian-Eulerian method may be extended to include the solid wall in the computations as the third phase in addition to the liquid and vapor phases. However, it gets complicated to handle the moving meshes when the solid parts are included. Hence, the Cahn-Hilliard phase-field method, an alternative numerical method is considered in the next section for the simulation of bubble nucleation out of cavities.

CHAPTER 4

NUMERICAL MODEL 2: PHASE-FIELD METHOD

In this chapter Cahn-Hilliard phase-field method is introduced to simulate the boiling in the microchannels. The simulations performed maybe presented in two sections. Firstly, the hydrodynamics and heat transfer characteristics of a vaporized elongated bubble in contact with the superheated water is investigated in a rectangular microchannel. Then subcooled water boiling in which nucleation initiates from an artificial cavity on the inner surface of a microchannel is simulated. Unlike the previous numerical studies in the literature, which presumed a generated bubbles at the beginning of the simulations or a pseudo-boiling in which bubbles are generated by the injection, the boiling initiates from a cavity and the growth and departure of the nucleated bubbles from the cavity are simulated. Numerical simulations of single bubble shape are qualitatively compared with experimental data. The bubble growth rate is quantitatively compared with the experimental result. Finally, three microchannels with different sizes of cavities are compared to investigate the surface roughness on boiling [71,72,73].

4.1 Cahn-Hilliard Phase-Field Method

The interface of two immiscible fluids often needs special consideration. One method of handling moving boundaries is to keep track of the motion of material points residing on the interface. Numerically, this may be realized by using grid points moving either with the local fluid velocity or a mesh velocity. This Lagrangian approach is often known as interface tracking. However, interfacial deformation causes some difficulties as remeshing and interpolation increasing the computational cost and error. An alternative to interface tracking is to track the fluid flow of both components on a fixed Eulerian grid, with the interface being determined or reconstructed at each time step by using a scalar indicator function. Examples of this class of methods are the volume of fluid (VOF) method, the level-set method (LS) and the phase-field method [74]. The diffuse interface models for a wide variety of interfacial phenomena such as binary fluids are addressed in literature [75,76,77]. The interface topology is estimated poorly by the volume of fluid approach used to calculate the surface tension force [61]. The phase-field method not only convects the fluid interface as in the level set method, but it also ensures that the total energy of the system diminishes correctly.

The phase-field based models replace sharp fluid-material interfaces by thin but nonzero thickness transition regions in which the interfacial forces are smoothly distributed [78]. The phase-field method has been broadly used in physics, material science [79], fracture mechanics [80] and multiphase flow [81,82]. The basic idea is to introduce an order parameter or phase-field that varies continuously over thin interfacial layers and is mostly uniform in the bulk phases. The order parameter has a physical meaning, and can be applied to different phase change phenomena by a proper modification of the free energy. An extremely thin interface layer is required to properly model the physics of the problem. In addition, relatively high computational resolution is required to handle the large gradients at the interface [83].

The interface has a small but finite thickness which contains two mixed components (phases), and stores a mixing energy. The free energy density of an isothermal mixture of two immiscible fluids is the sum of the mixing energy and the elastic energy. The mixing energy may be expressed as [74]

$$f_{mix}\left(\emptyset, \nabla\emptyset\right) = \frac{1}{2}\lambda\left|\nabla\emptyset\right|^2 + \frac{\lambda}{4\epsilon^2}(\emptyset^2 - 1)^2 \tag{4.1}$$

where ϕ is the dimensionless phase-field variable defined such that the volume fraction of the components of the fluid are $(1+\phi)/2$ and $(1-\phi)/2$. The quantity λ [N] is the mixing energy density, and ϵ [m] is a capillary width that scales with the thickness of the interface.

The evolution of the phase-field variable ϕ is governed by the Cahn-Hilliard equation, which is a 4th-order partial differential equation in the form of

$$\frac{\partial \phi}{\partial t} + \boldsymbol{u} \cdot \nabla\phi = \nabla \cdot \gamma\nabla G \tag{4.2}$$

where $\boldsymbol{u}$ and γ are the velocity vector [m/s] and the mobility [m^3·s/kg], respectively, and G [Pa] is the chemical potential which is defined as

$$G = \lambda \ \ -\nabla^2\phi + \frac{\phi(\phi^2 - 1)}{\epsilon^2} \tag{4.3}$$

The mixing energy density, λ, and the capillary width, ϵ, are related to the surface tension coefficient, σ [N/m], through Equation(4.4) [74].

$$\sigma = \frac{2\sqrt{2}}{3}\frac{\lambda}{\epsilon} \tag{4.4}$$

The interface thickness is assumed to be the half of the mesh element size at the interface. Then the capillary width, and consequently, the mixing energy density may be found using Equation (4.4). For instance, if the mesh size at the interface is 0.8 µm, the capillary width will be $\epsilon = 0.4$ µm and for water with a surface tension of σ = 0.0588 N/m, the mixing energy density will be $\lambda = 0.25\times10^{-6}$ N.

The Cahn-Hilliard equation forces ϕ to take a value of 1 or −1 except in a very thin region at the fluid-fluid interface.

The phase-field interface decomposes Equation (4.2) into two second-order partial differential equations as

$$\frac{\partial \phi}{\partial t} + \boldsymbol{u} \cdot \nabla\phi = \nabla \cdot \frac{\gamma\lambda}{\epsilon^2}\nabla\psi \tag{4.5}$$

$$\psi = -\nabla \cdot \epsilon^2\nabla\phi + (\phi^2 - 1)\phi \tag{4.6}$$

where ψ is the phase-field help variable.

Generally, the well-known Navier-Stokes equations describe the velocity and pressure fields for the liquid phase as follows

$$\rho_L \frac{\partial \boldsymbol{u_L}}{\partial t} + \rho_L (\boldsymbol{u_L} \cdot \nabla) \boldsymbol{u_L} = \nabla \cdot \left[-p_L \mathbf{I} + \mu_L \left(\nabla \boldsymbol{u_L} + (\nabla \boldsymbol{u_L})^T \right) \right] + \rho_L \boldsymbol{g} + \boldsymbol{F} \tag{4.7}$$

$$\nabla \cdot \boldsymbol{u_L} = 0 \tag{4.8}$$

where L and V denote the liquid and vapor phases, respectively. $\boldsymbol{g}$ [m/s^2], $\boldsymbol{F}$ [N/m^3], p [Pa] and μ [Pa·s] are the gravitational acceleration vector, the surface tension force per unit volume, the pressure and the viscosity, respectively.

For the vapor phase, the weakly compressible Navier-Stokes equations are solved

$$\rho_V \frac{\partial \boldsymbol{u_V}}{\partial t} + \rho_V (\boldsymbol{u_V} \cdot \nabla) \boldsymbol{u_V} = \nabla \cdot \left[-p_V \mathbf{I} + \mu_V \left(\nabla \boldsymbol{u_V} + (\nabla \boldsymbol{u_V})^T \right) - \frac{2}{3} \mu_V (\nabla \cdot \boldsymbol{u_V}) \boldsymbol{I} \right] + \rho_V \boldsymbol{g} + \boldsymbol{F} \tag{4.9}$$

$$\frac{\partial \rho_V}{\partial t} + \nabla \cdot (\rho_V \boldsymbol{u}_V) = 0 \tag{4.10}$$

The vapor density is determined through the ideal gas law.

Since the temperature at the liquid-vapor interface is set to the saturation temperature, a constant temperature throughout the entire vapor is obtained by solving the conservation of energy equation which, in this case, is the heat conduction equation.

$$\rho_V C_P \frac{\partial T_V}{\partial t} + \rho_V C_P (\boldsymbol{u_V} \cdot \nabla) T_V = \nabla \cdot (k_V \nabla T_V) \tag{4.11}$$

In this equation, C_p [J/kg·K] and k [W/m·K] are the specific heat and the thermal conductivity, respectively.

4.2 Numerical Model and Governing Equations

To investigate the evolution of the interface as well as the bulk fluid, the phase-field method is coupled with the foregoing conservation equations for the mass, momentum and energy. For this reason, the use of any special algorithm for tracking the interface or satisfying sharp interface balances is not required.

The Cahn-Hilliard Equation (4.2) for the phase-field variable is modified to include the phase change as

$$\frac{\partial\phi}{\partial t} + \boldsymbol{u}\cdot\nabla\phi - m\delta\left(\frac{V_{f,V}}{\rho_V} + \frac{V_{f,L}}{\rho_L}\right) = \nabla\cdot\frac{\gamma\lambda}{\epsilon^2}\nabla\psi \tag{4.12}$$

where $V_{f,L}$ and $V_{f,V}$ are the volume fractions of the liquid and the vapor, respectively. The quantity δ [1/m] is a smoothed representation of the interface between the two phases. It is defined as

$$\delta = 6V_{f,L}(1 - V_{f,L})\frac{\nabla\phi}{2} \tag{4.13}$$

The surface tension force appears as a volumetric body force in the momentum Equation (4.7) as

$$\rho\frac{\partial\boldsymbol{u}}{\partial t} + \rho\;\boldsymbol{u}\cdot\nabla\;\boldsymbol{u} = \nabla\cdot\;-p\boldsymbol{I} + \mu\;\nabla\boldsymbol{u} +\;\nabla\boldsymbol{u}^{\;T}\;\; + \rho\boldsymbol{g} + G\nabla\phi \tag{4.14}$$

The continuity Equation (4.8) is also modified to include the effect of the phase change from liquid to vapor [84]

$$\nabla\cdot\boldsymbol{u} = m\delta\left(\frac{1}{\rho_V} - \frac{1}{\rho_L}\right) \tag{4.15}$$

The mass flux leaving the interface can be evaluated from the conductive heat flux as

$$m = -\frac{k_V \nabla T}{h_{lg}} \tag{4.16}$$

Due to the large differences in the thermophysical properties across the interface, a more suitable correlation for the mass transfer rate is

$$m = \begin{cases} rV_{f,L}\rho_L \dfrac{T - T_{sat}}{T_{sat}} & T › T_{sat} \\ -rV_{f,V}\rho_V \dfrac{T_{sat} - T}{T_{sat}} & T ‹ T_{sat} \end{cases} \tag{4.17}$$

At the interface where the liquid is superheated ($T › T_{sat}$), the mass transfers from the liquid to the vapor and is positive. Inversely, where in the liquid is subcooled ($T ‹ T_{sat}$) the mass transfers from the vapor to the liquid.

r is a constant which is set equal to 0.1 by Lee [85] and 100 by Yang *et al.* [86]. In the present study, $V_{f,L}$ and $V_{f,V}$ are included in Equation (4-13) for δ, and the mass flux is calculated as

$$m = \begin{cases} R\rho_L \dfrac{T - T_{sat}}{T_{sat}} & T › T_{sat} \\ -R\rho_V \dfrac{T_{sat} - T}{T_{sat}} & T ‹ T_{sat} \end{cases} \tag{4.18}$$

where *R* [m/s] is a constant , and should be sufficiently large to keep the interface at the saturation temperature. In this study, the results numerically diverge for *R* values greater than 0.2. In addition, *R* values less than 0.06 yield an increased deviation of the interface temperature from the saturation temperature. The value of *R* is set to 0.1 m/s which is optimized based on the minimization of the error between the experimental data [60] and the simulations.

The mass flux added in the energy Equation (4.11) to include the effect of the generated latent heat at the interface as

$$\rho C_P \frac{\partial T}{\partial t} + \rho C_P \ \boldsymbol{u} \cdot \nabla \ T = \nabla \cdot \mathrm{k} \nabla T - m \delta h_{lg} \tag{4.19}$$

where h_{lg} [J/kg] is the latent heat. The thermal conductivity and the specific heat are calculated as functions of the volume fraction of the two phases as follows

$$k = \ k_L - k_V \ V_{f,L} + k_V \tag{4.20}$$

$$C_p = \ C_{p,L} - C_{p,V} \ V_{f,L} + C_{p,V} \tag{4.21}$$

4.3 Simulation of the Nucleated Bubble in the Superheated Fluid in the Microchannel

4.3.1 Geometry and Computational Domain

The growing rate and the shape of the vapor bubble inside the microchannel have been validated by the experimental data of Mukherjee *et al.* [60] for a microchannel of 229 μm hydraulic diameter. The temperatures of the side walls and the bottom wall are set to 102.1°C. The top wall is adiabatic. Water flows through the microchannel with Reynolds number *Re* = 100 at saturation temperature. The contact angle at the walls is $\theta = 30°$. Initially it is presumed that a nucleated bubble of 40 μm diameter exists inside the microchannel on the bottom wall with its center located at $x = 0$, $y = 229$ μm, and $z = 20$ μm as shown in Figure 4.1. The simulations have been performed by using finite element software, COMSOL Multiphysics™. The mesh convergence analysis, and the vapor bubble growth rate and shape are presented next.

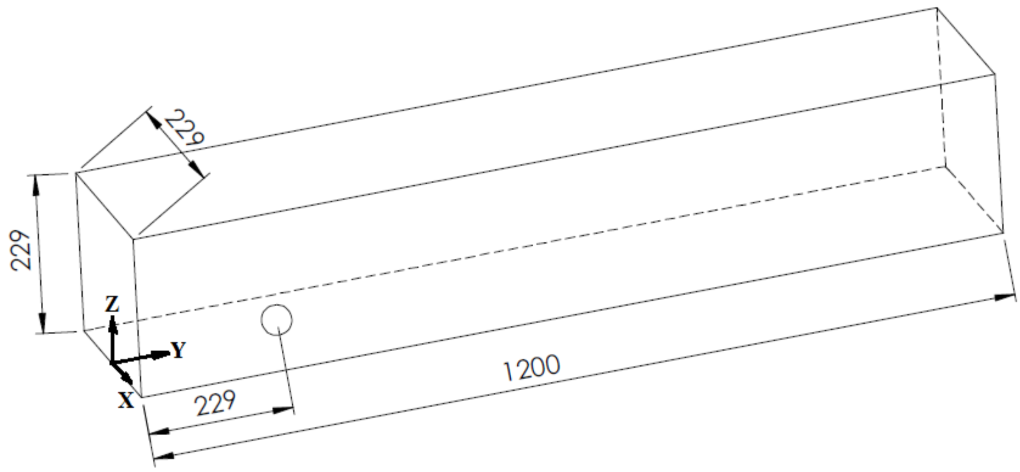

Figure 4.1 The computational domain (dimensions in μm)

4.3.2 Mesh Convergence Analysis

At the thin interface, high gradients of the investigated parameters exist. For this reason, finer grids are required at the interface compared to the remaining regions of the model. Figure 4.2 shows the distribution of the grids inside and around the bubble for the initialization of the simulations. The interface thickness is adjusted as half of the mesh element size in the region where the interface passes. Different triangular mesh sizes are used to calculate the bubble growth rate for the optimization of the numerical accuracy and the computational time. With an Intel® Xeon® CPU E5-16200 @ 3.60 GHz processor with 32 GB RAM, the computation times were about 40, 681 and 7326 minutes, for coarse grids (18682), fine grids (88814) and finer grids (355256), respectively. Figure 4.3 illustrates the equivalent diameter of the bubble for the three different grid sizes at various time steps. With the two finer meshes, about 0.07 ms time difference occurred for the bubble to grow to a diameter of 0.2 mm, and a maximum difference of 4.2% has been observed between the bubble diameters obtained at the same instant. The difference in the bubble diameter has reached 26.4% for the two coarser meshes. Hence, the simulations have been continued with 88814 meshes. At the interface between the liquid and vapor domains, the mesh sizes vary between 0.03 µm to 1 µm. The mesh size grows up to 2.9 µm far from the interface.

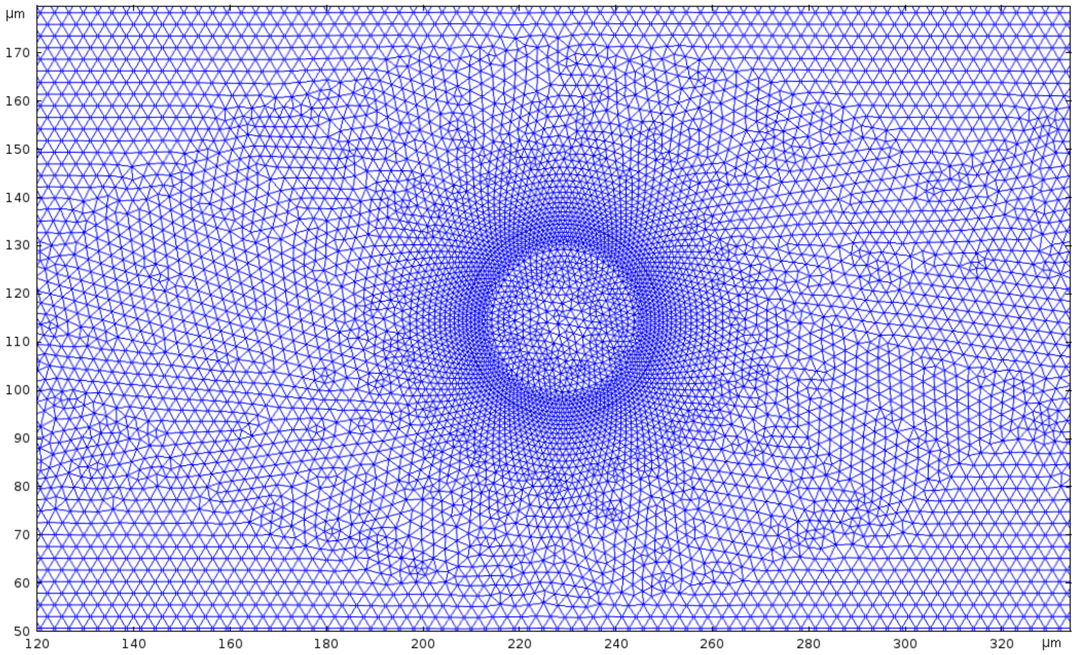

Figure 4.2 The close up view of the computational mesh inside and around the initial bubble

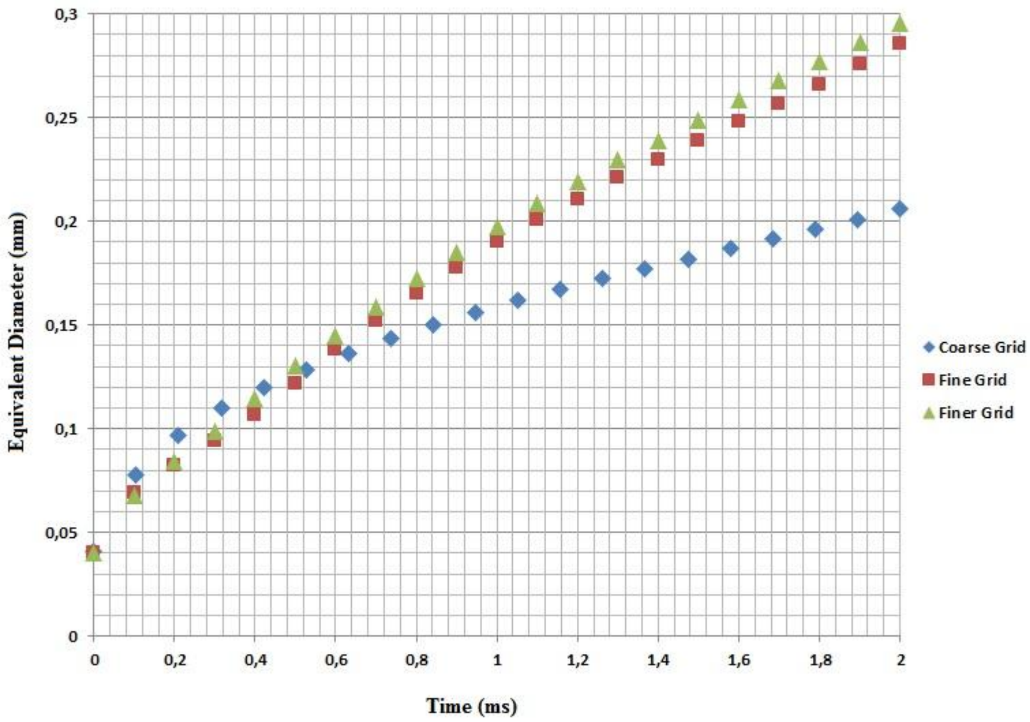

Figure 4.3 Equivalent diameter of the bubble with three different grid sizes

4.3.3 Validation of the Model

The simulations were performed in a two dimensional (2D) domain to save computational power and time. The gravitational force is employed along the side plane (in *z*-direction). The equivalent diameter of the nucleated vapor bubble is calculated along the top plane (the central horizontal XY plane) and the side plane (the central vertical ZY plane) of the microchannel.

Figure 4.4 compares the bubble growth rates obtained by the present simulations and the experimental data [60]. The results of the simulation are in very good agreement with the experimental data. The temporal evolution of the bubble shape is also compared with the same experimental study [60] as illustrated in Figure 4.5. There are deviations in the growth rate and shape of the bubble from those of the experimental study with increase in time. The maximum deviation is 18%.

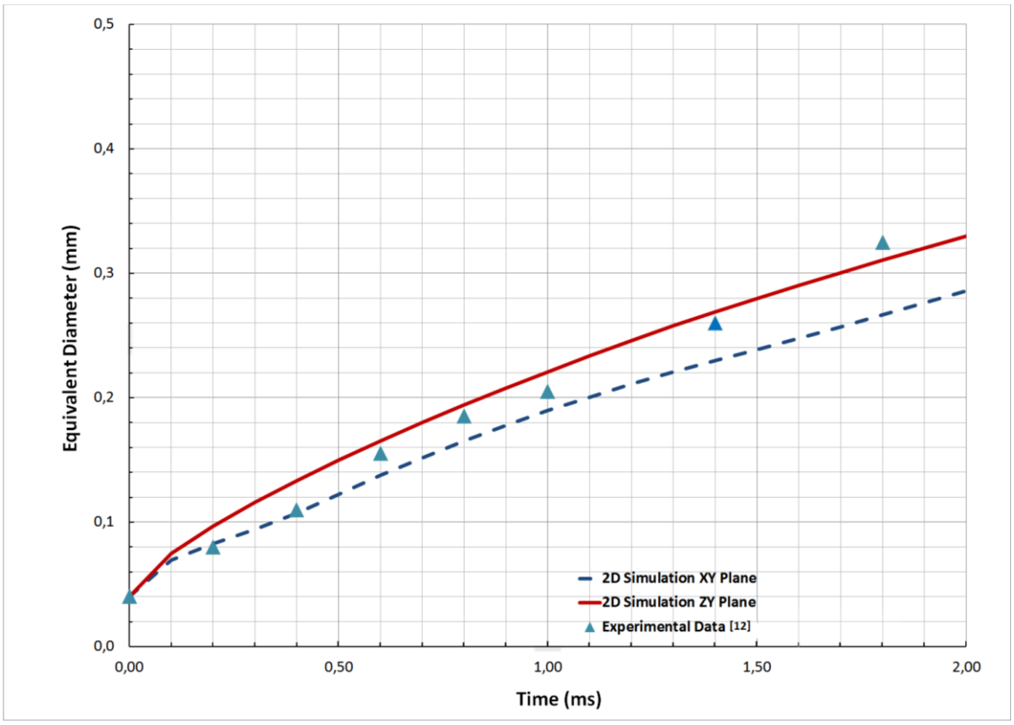

Figure 4.4 The comparison of the bubble growth rates of the present numerical simulation and the experimental data [60]

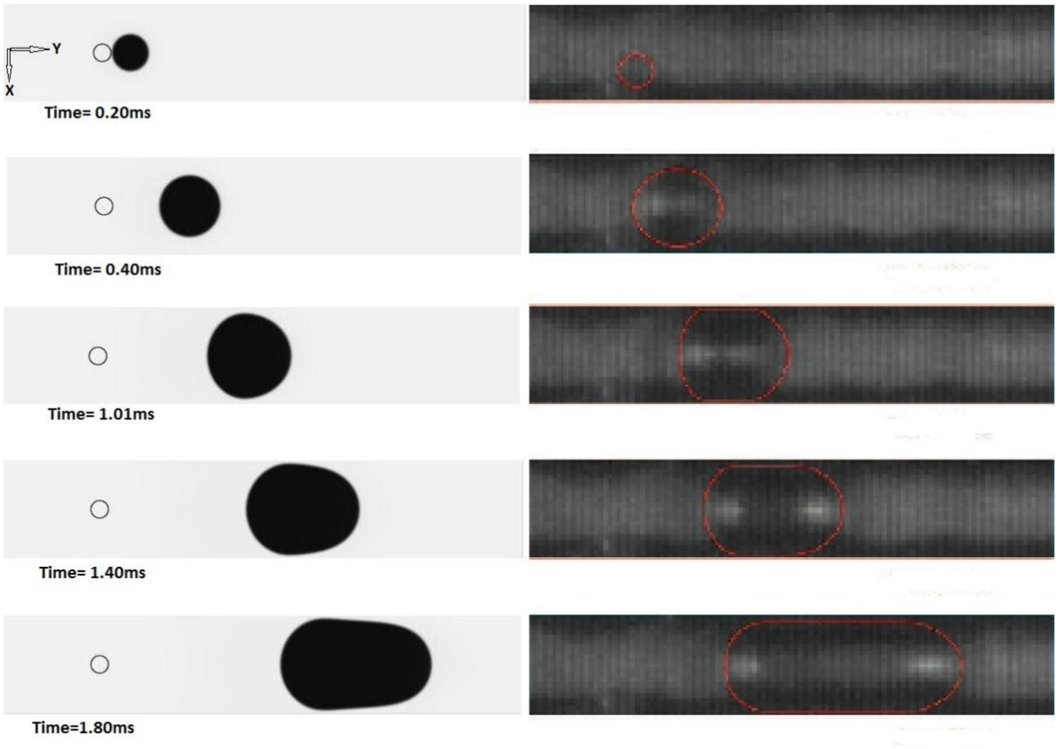

Figure 4.5 The comparison of the bubble shapes of the present numerical study (left) and the experimental study [60] (right), at the same instant.

To investigate the reasons for the deviations, the total free energy of the system has been calculated using the surface tension, Equation (4.22), as well as the mixing energy (Equation (4.23)) [74].

$$F_1 = \quad \sigma dA \tag{4.22}$$

$$F_2 = \quad (\frac{1}{2}\lambda \ \nabla\phi \ ^2 + \frac{\lambda}{4\varepsilon^2}(\phi^2 - 1)^2)dV \tag{4.23}$$

Figure 4.6 indicates the difference, which may be attributed to the mass losses that occur during the bubble growth with increasing time.

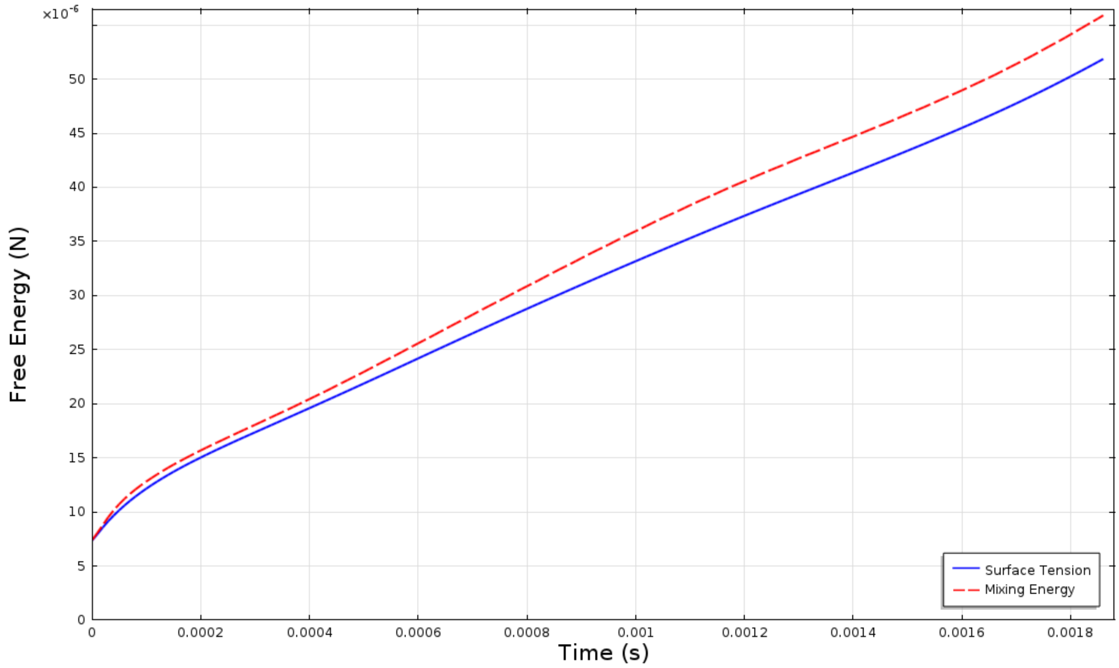

Figure 4.6 The surface tension and mixing energy in the bubble interface

4.3.4 Results and Discussion

For analyzing the local hydrodynamics and heat transfer of the vapor bubble inside the microchannel in detail, the water inlet and initial temperatures and the wall temperature are set to 102.1°C. This way, the effect of convective heat transfer between the wall and water has been eliminated. Only the boiling heat transfer effect is maintained. Figure 4.7 depicts the velocity distribution inside and around the elongated bubble in the central horizontal XY plane and the central vertical ZY plane, respectively. Both distributions were captured at time t = 1.8 ms.

Figure 4.7a shows that the downstream velocity increases up to 0.54 m/s whereas the upstream velocity remains low at about 0.13 m/s. It may be inferred that the liquid is pushed forward at a faster rate downstream due to the bubble growth. The high rate of evaporation at the nose of the bubble, which is indicated by the greater velocities around the interface, accelerates the bubble nose movement. As a result, and based on the conservation of mass, the velocity of the vapor inside the bubble increases up to 0.8 m/s near the nose. It can also be observed that the thin liquid film between the wetted walls and the bubble downstream has higher velocity which increases the rate of evaporation.

Figure 4.7b illustrates higher velocity downstream compared to the upstream of the bubble. The downstream velocity is 0.58 m/s while the upstream velocity is about 0.13 m/s. A high rate of evaporation is indicated in the regions of high velocity gradients, namely, the bubble nose, and the liquid film between the bottom wall and the bubble nose. Since the top wall is adiabatic, there is no heat flux from the top wall into to the microchannel. Hence, the evaporation rate at the top of the bubble is lower.

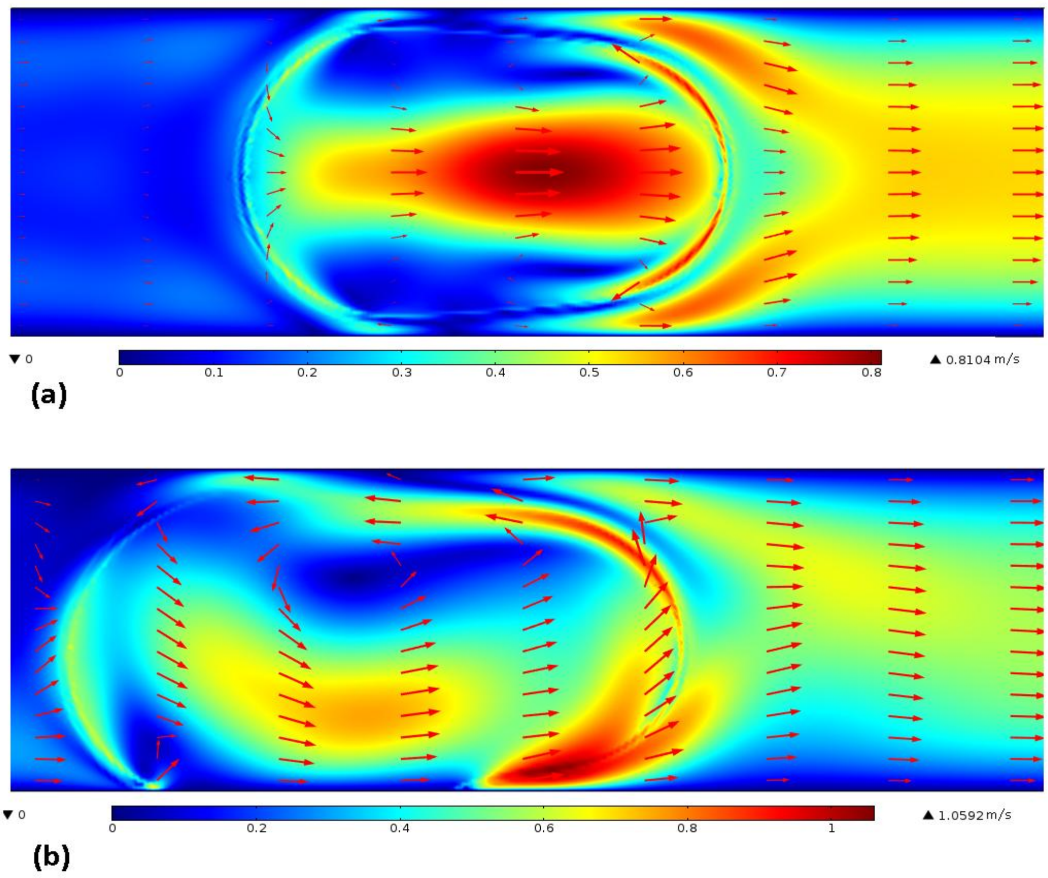

Figure 4.7 The velocity distribution inside and around the elongated vapor bubble (a) XY plane and (b) ZY plane at t = 1.8 ms

Figure 4.8 illustrates the temperature distribution inside and around the elongated vapor bubble in the central horizontal XY plane and the central vertical ZY plane, respectively. Figure 4.8a shows that the temperature inside the bubble remains at the saturation temperature due to the thin saturated liquid film between the bubble and the side walls. As the bubble evolves into an elongated one, the temperature gradient increases in the thermal boundary layer developed on the side walls. This increases the local heat flux as well. Figure 4.8b indicates that the adiabatic top wall remains at the saturation temperature where it meets the elongated vapor bubble. On the other hand, the part of the bubble touching the bottom wall is at the superheated temperature.

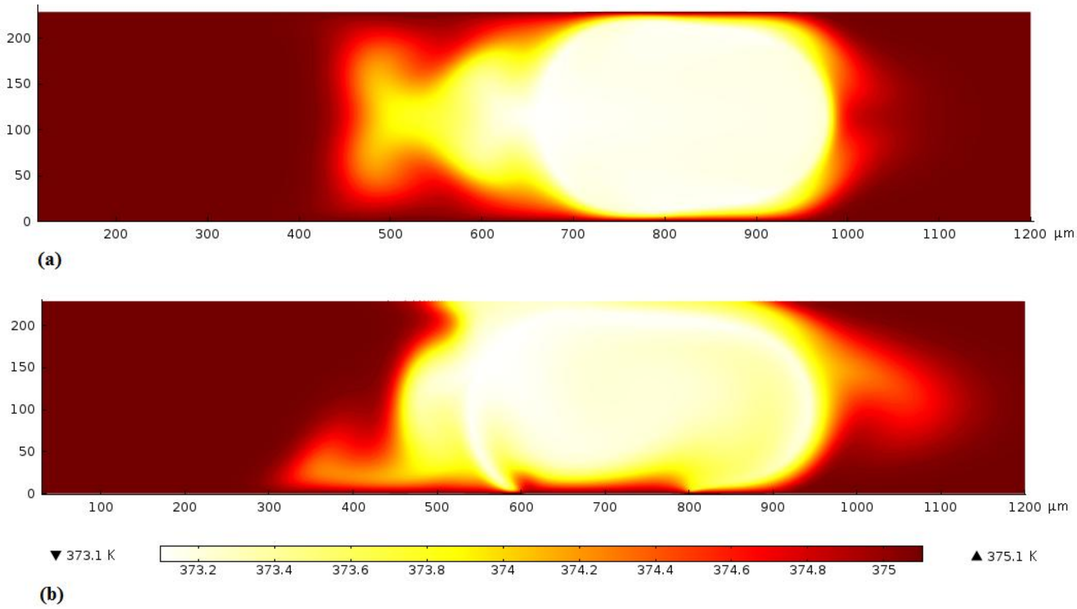

Figure 4.8 The temperature distribution inside and around the elongated vapor bubble (a) XY plane and (b) ZY plane at t = 1.8 ms

Figure 4.9a demonstrates the local heat transfer coefficient and the heat flux along the side wall of the microchannel. It is observed that the evaporation heat transfer coefficient increases to 91200 W/m^2 ·K at L = 700 μm, where the thickness of the thin liquid layer between the bubble and the wall is the smallest. The corresponding maximum heat flux is 182 kW/m^2.

Figure 4.9b shows the local heat transfer coefficient and the heat flux along the bottom wall of the microchannel where the nucleated vapor bubble lies on it. The local heat transfer coefficient increases up to around 137000 W/m^2 ·K at locations where the liquid film, the bubble and the wall are all in contact. When the bubble touches the bottom wall on the other hand, the heat transfer coefficient drops significantly due to diminishing temperature gradients. It can be observed from Figure 4.9b that a maximum heat flux of 270 kW/m^2 could be dissipated from the bottom wall.

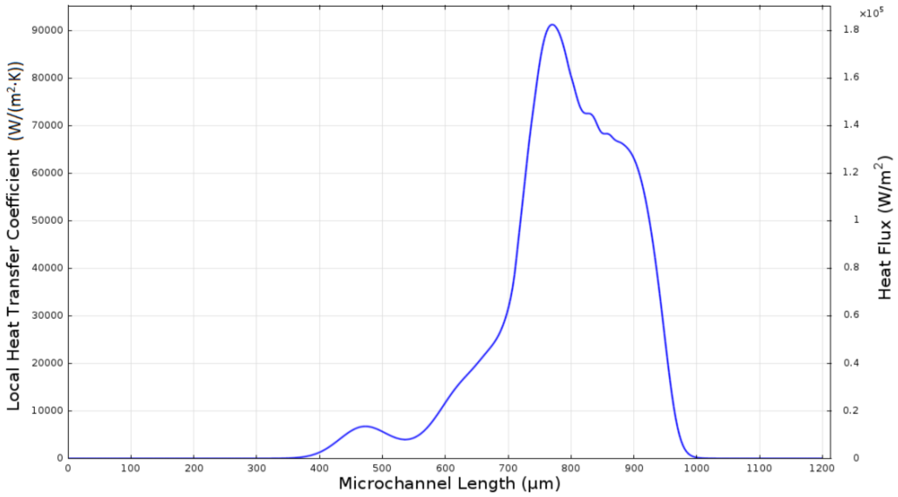

(a)

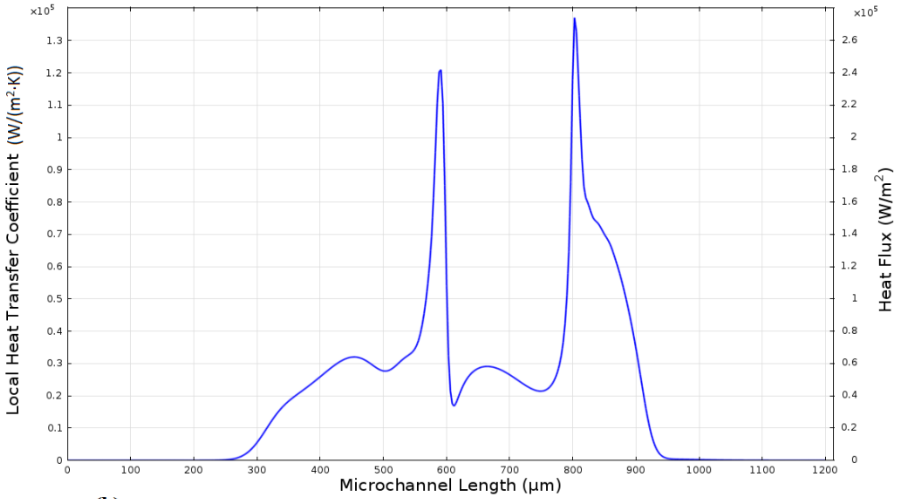

(b)

Figure 4.9 The local heat transfer coefficient and the heat flux on (a) the bottom wall and (b) the side wall at t = 1.8 ms

The average heat transfer coefficients of the bottom and side walls are illustrated in Figure 4.10. Since the bubble nucleates on the bottom wall initially, the heat transfer coefficient at the bottom wall is not zero at the initial time. At about 1 ms the bubble starts to elongate and the average heat transfer increases linearly.

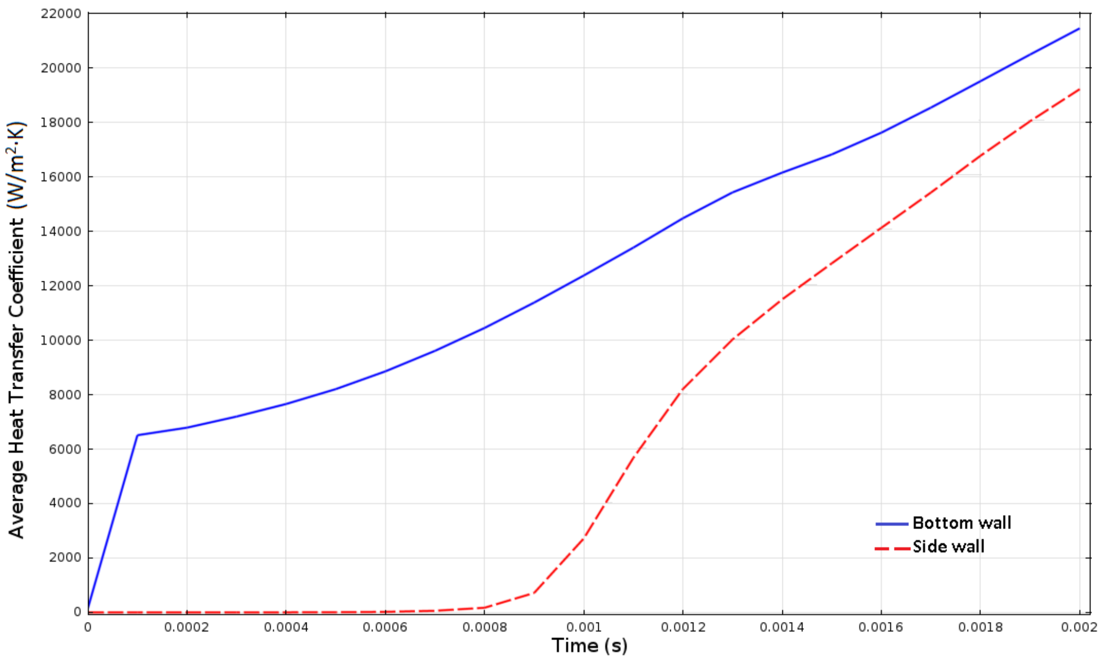

Figure 4.10 The average heat transfer coefficients over the side walls and the bottom wall

Figure 4.11displays the pressure inside and around the elongated vapor bubble at the central XY and ZY planes. The pressure inside the bubble is 101.95 kPa which is about 450 Pa higher than that of the liquid around it. The mass flux leaving the liquid surface leads to the increase in the vapor pressure, and to the expansion of the vapor region. The difference between the downstream and upstream pressures is about 100 Pa. At the interface, especially around the nose of the bubble, higher pressure gradients exist, which is a similar trend to that observed in the velocity plots of Figure 4.7. The presence of the surface tension force leads to this discontinuity in pressure across the interface.

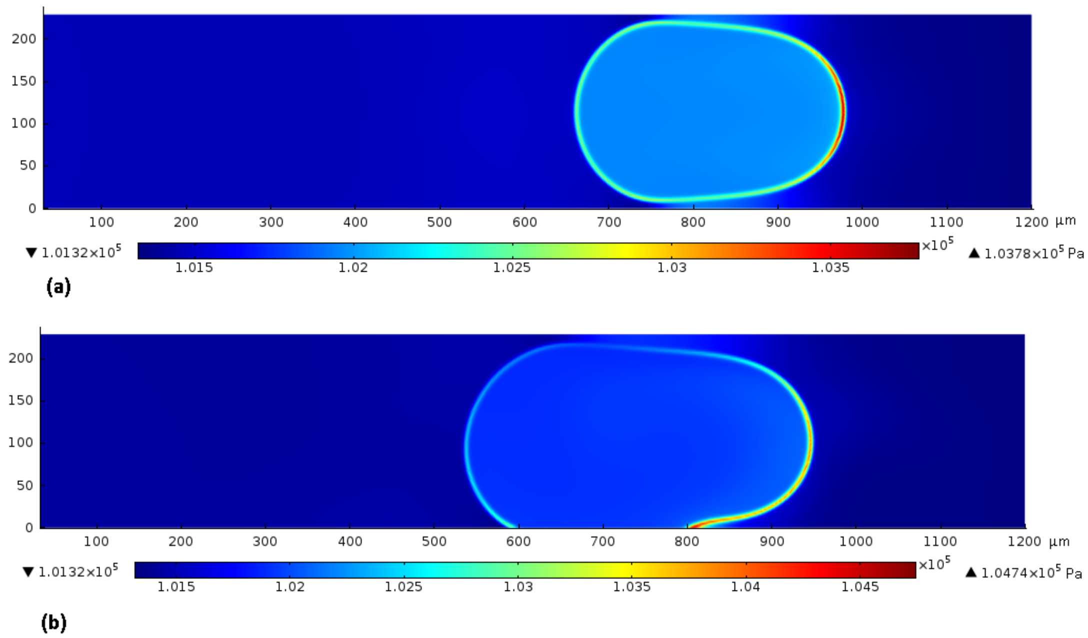

Figure 4.11 The pressure distributions of the central XY plane (a) and the central ZY plane (b) at t = 1.8 ms

To investigate the influence of the contact angle on the bubble shape, and eventually on the heat transfer performance, four different contact angles, namely, 20˚, 30˚, 40˚ and 80˚ have been considered. The respective simulations have been conducted at various inlet velocities of 0.0645 m/s (*Re* = 50), 0.129 m/s (*Re* = 100), and 0.258 m/s (*Re* = 200) in order to include the simultaneous effects of the inlet velocity and the contact angle. Figure 4.12,13,14 compare the average heat transfer coefficient over the bottom wall as a function of time for different contact angles.

Figure 4.12 illustrates that at the lowest inlet velocity of 0.0645 m/s, the heat transfer coefficient gradually increases with time for the contact angles of Θ = 30˚, 40˚ and 80˚. For Θ = 20˚, on the other hand, the average heat transfer coefficient fluctuates with time. The reason may be that the bubble cannot stay attached to the bottom wall as it elongates along the microchannel length due to the low contact angle. This behavior is also observed at higher inlet velocities.

When the inlet velocity is doubled as demonstrated in Figure 4.13, the average heat transfer coefficient also increases for all contact angles. For Θ = 30˚, the amount of the thin liquid layer between the wall and the bubble nose increases with increased velocity. It is for this reason that the heat transfer coefficient is the highest for Θ = 30˚ and keeps increasing with increased inlet velocity as shown in Figure 4.14. For all velocities, the bubble is elongated the most for Θ = 30˚. The increased evaporation surface area of the longer bubble also supports the increased heat transfer rate.

As the inlet velocity is further increased, as illustrated in Figure 4.14, the heat transfer coefficient increases sharply for the lower contact angles of Θ = 20˚ and Θ = 30˚. On the other hand, the increase is more gradual, and relatively lower heat transfer coefficients are attained for Θ = 40˚ and Θ = 80˚.

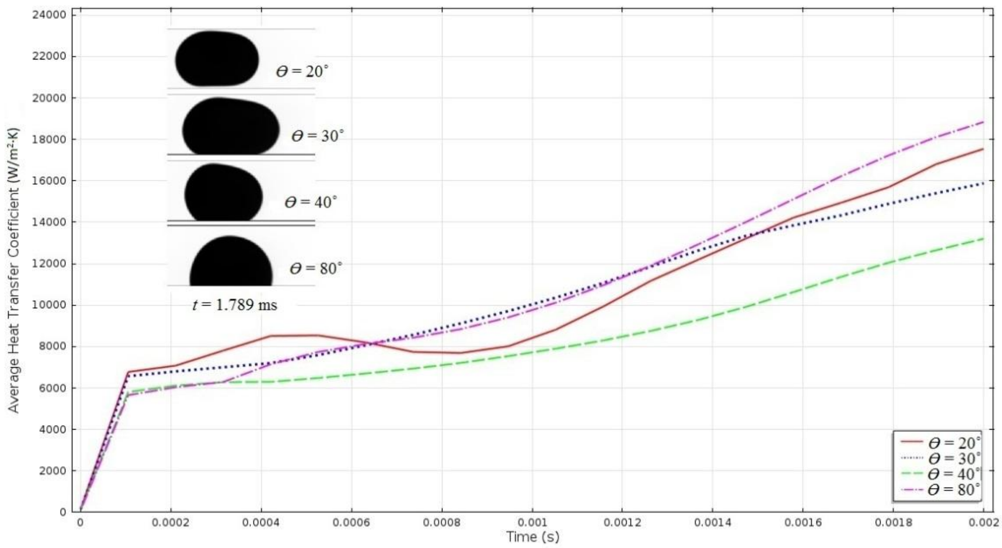

Figure 4.12 The effect of the contact angle on the average heat transfer coefficient for the inlet velocity of 0.0645 m/s

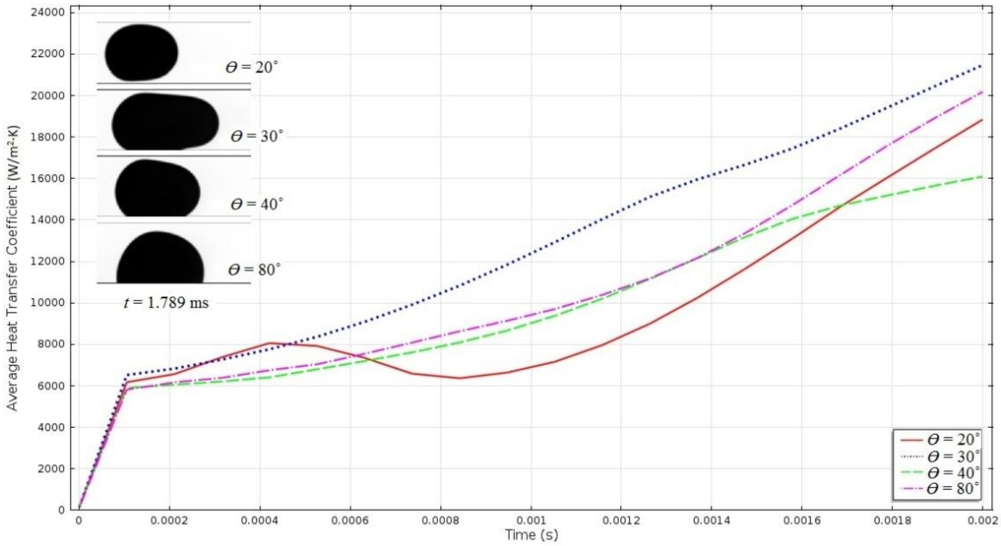

Figure 4.13 The effect of the contact angle on the average heat transfer coefficient for the inlet velocity of 0.129 m/s

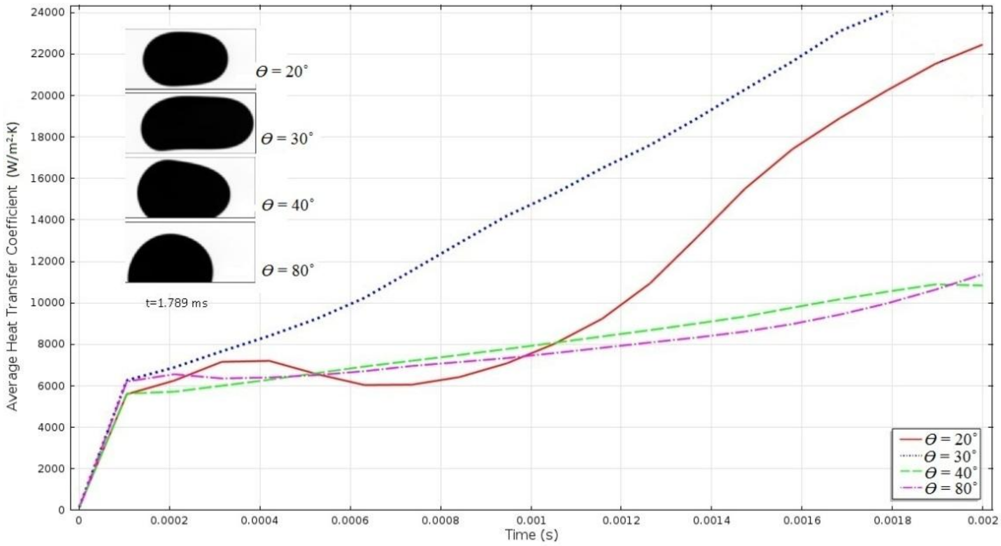

Figure 4.14 The effect of the contact angle on the average heat transfer coefficient for the inlet velocity of 0.258 m/s

4.4 Simulation of the Nucleation from an Artificial Cavity of the Subcooled Water into the Microchannel

4.4.1 Geometry and Computational Domain

To be able to compare the bubble growth rate and the bubble shape, the computational domain is selected such that it represents the experimental conditions of Lee *et al*. [87]. The microchannel length is equal to 64 mm and the cross section is 100 μm × 100 μm. The coolant is water with properties at 1 atm and the subcooled inlet temperature is maintained at 24±1°C. An artificial cavity is located at one-third of the microchannel length measured from the inlet (21.4 mm). The cavity has a conical inlet of 25 μm diameter, a cylindrical body of 15 μm diameter and a depth of 13 μm. The simulations have been performed in a two dimensional (2D) domain and non-uniform grids have been used to save computational power and time. Since high gradients of the investigated parameters exist at the interface, the grid size inside and around the cavity is finer (0.2 μm-1 μm) than that in the remaining region of the microchannel (4.5 μm-8.0 μm). The bottom wall temperature is set to T_{sat} + 2°C and the top wall is assumed adiabatic. Figure 4.15 shows the dimensions of the cavity, the boundary condition and the initial condition for the flow.

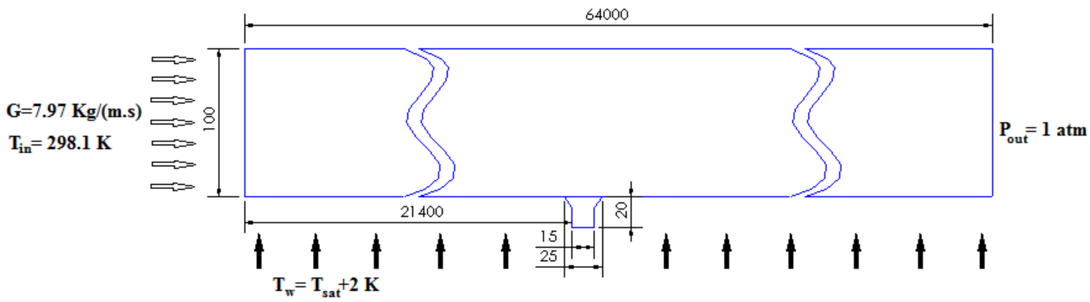

Figure 4.15 Computational domain, initial and boundary conditions (dimensions in μm's)

4.4.2 Results and Discussion

The simulations have been performed by COMSOL Multiphysics™, a robust finite element solver. The simulation starts in single phase and continues until the thermal boundary layer changes to a few microns at the bottom wall where the cavity exists.

It means the temperature of the water at the top of the cavity is equal at least to the saturation temperature. At this time, as illustrated in Figure 4.16, it is presumed that the vapor embryo is created at the bottom of the cavity (t = 0). Also the attained thermal and hydraulic boundary layers are employed as initial conditions to simulate the two phase evaporation. Results indicate that the vapor embryo begins growing rapidly due to heat transfer from the superheated wall layer (t = 0.1 ms), and a single bubble is formed at the mouth of the cavity (t = 0.5 ms). Then the bubble grows to the size of the hydraulic diameter and expands as a capillary bubble (t = 2 ms). By the growth of the bubble and its detachment from the cavity, the remaining vapor inside the cavity serves as a nucleus for the next cycle of the bubble growth (t = 3.5 ms), and a slug flow is observed (t = 10 ms). The bubble grows longitudinally moving through the microchannel.

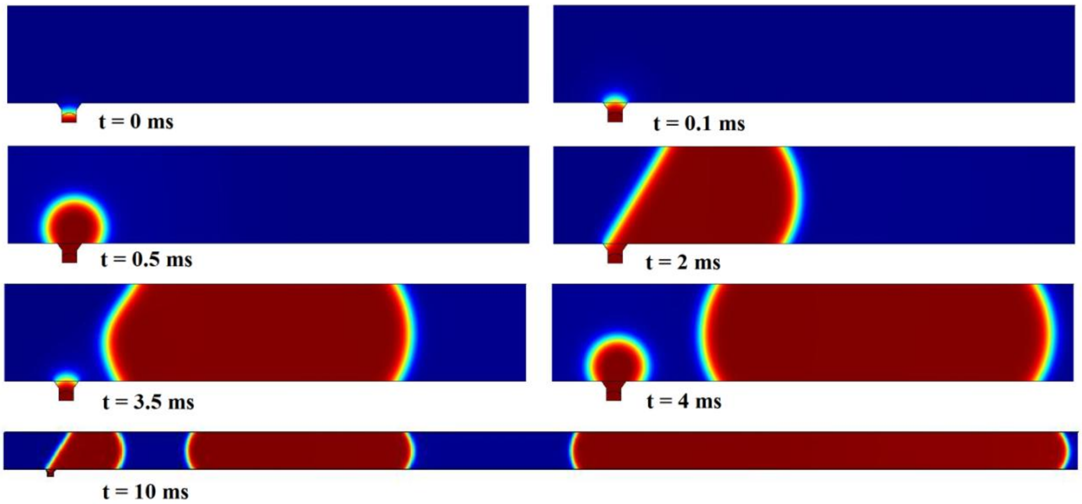

Figure 4.16 The bubble formation and departure from the microcavity

Figure 4.17 shows the comparison of the bubble growth rate obtained with the present simulation and with the experiments conducted by Lee *et al*. [87]. The time scale for the experimental results is a hundred times greater than that of the simulations. Lee *et al.* reported the same bias between their experimental results and the analytical solution of Mikic and Rohsenow [88] which is illustrated by the black bold line marked as $R_b \sim t^{0.5}$. Considering the difference in the time scales, there is a good agreement for the bubble radius between the present simulations and the experimental results [87] with a maximum deviation of 30.4%. The bubble shape obtained from the simulation and the experiments at different instants are shown in the Figure 4.18. Since the simulation has been conducted in a two dimensional coordinate system and the cross section of the microchannel is a square, it is assumed the bubble grows uniformly at the cross section. Hence, the shape of the bubble from the side view is compared with the experimental results which are captured by a camera from the top view. It is observed that the displacement of the simulated bubble is more than that of the experimental one at the same instant. The reason is believed to be neglecting the viscosity effect on the lateral sides of the bubble due to the two dimensional simulation. In spite of these shortcomings, the shape of the simulated bubble is in agreement with the experimental one.

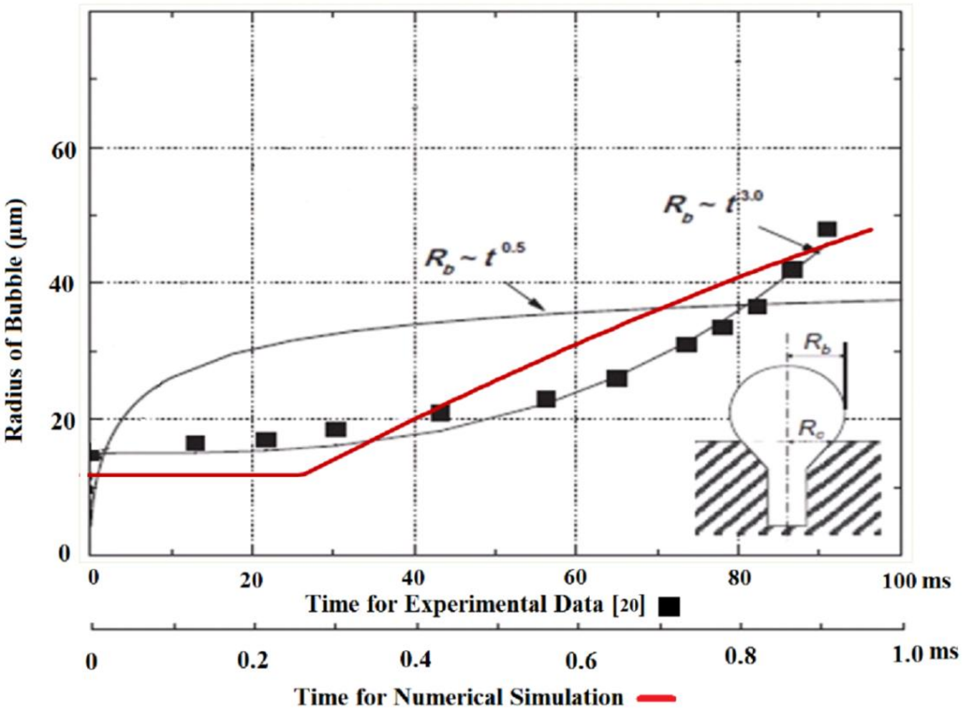

Figure 4.17 Comparison of the bubble radius obtained by the present numerical study and available experimental data [87]

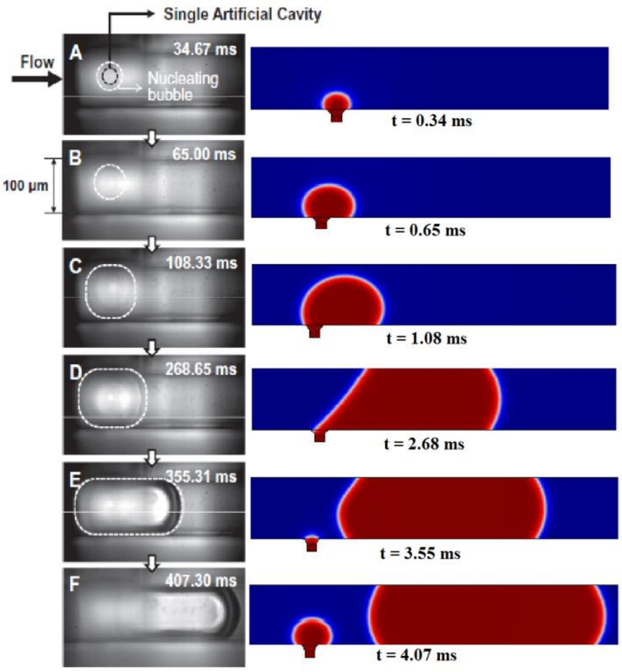

Figure 4.18 Comparison of the bubble shape at different times obtained by the present numerical study (right) and the experimental data (left) [87]

Figure 4.19 demonstrates the velocity distribution of the flow inside the microchannel at different time steps. At t = 0 ms the velocity distribution is uniform. The evaporation pushes the liquid around the bubble and the velocity at the interface increases (t = 0.5 ms). Eventually, the nose of the bubble accelerates downstream while the rear of the bubble remains at the inlet velocity. As a consequence, the liquid in the region ahead of the bubble accelerates strongly. The velocity at the downstream rises up to 0.2 m/s which is more than twenty times higher than the inlet velocity (t = 2 ms). While the second elongated bubble forms, the flow accelerates much more compared to the case with just a single bubble. At t = 2 ms, the velocity becomes forty times higher than the inlet velocity and this trend continues by the merging of the new bubbles (t = 10 ms).

Figure 4.20 exhibits the temperature inside and around the cavity in the microchannel. At time t = 0 the temperature is uniformly distributed from the heated bottom wall to the top adiabatic wall along the microchannel. As the evaporation begins, the isotherms are crowded between the bubble and the liquid which infers the existence of the high heat flux at the interface between the saturated vapor and the liquid (t = 0.5 ms). Since the growth of the bubble accelerates the liquid at the downstream, as illustrated in the Figure 4.19, the temperature of the liquid at the downstream increments compared to the upstream. It is apparent that the temperature of the vapor remains at the saturation temperature except where the vapor touches the bottom heated wall which is at superheated temperature.

The pressure distribution inside the microchannel at various time steps is shown in Figure 4.21. The pressure inside the bubble decreases gradually as the bubble grows. For instance, the pressure is P = 109.85, 106.63 and 105. 94 kPa at t = 0.5, 1 and 2 ms, respectively. By the merging of a new bubble the pressure increases again. It may be concluded that the merging of the new bubble pushes the liquid further, then the pressure at the upstream of the elongated bubble increases. A force balance along a diametric plane through the bubble yields the following equation [89]

$$p_V - p_L = \frac{2\sigma}{R_b} \tag{4.24}$$

According to the Equation (4.24), the pressure inside the elongated bubble increases as well.

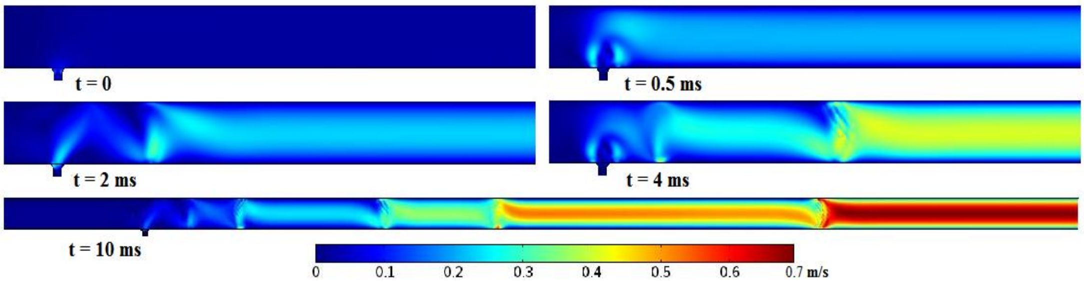

Figure 4.19 Velocity distribution in the two-phase section of the microchannel

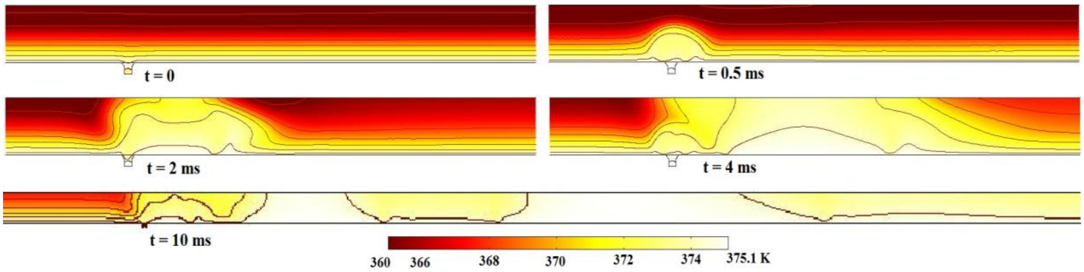

Figure 4.20 Temperature distribution in the two-phase section of the microchannel

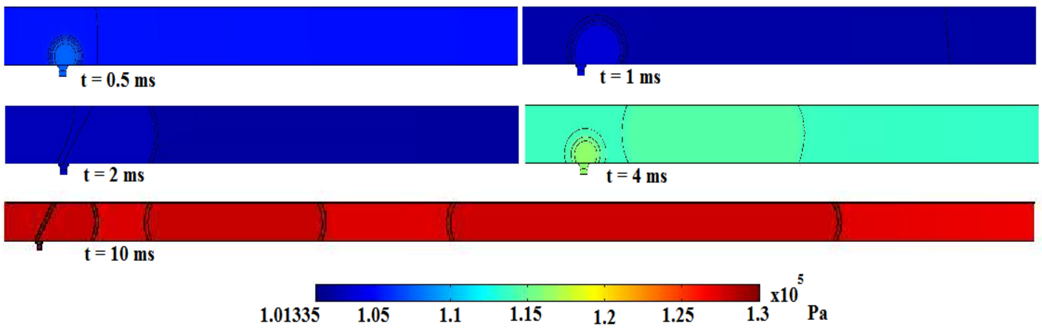

Figure 4.21 Pressure distributions in the two-phase zone of the microchannel at various time steps

To investigate the effect of mass flux on the flow patterns and the heat transfer performance of the microchannel, various mass fluxes are imposed at the inlet. Figure 4.22 illustrates the two phase flow distribution for six different mass fluxes from a low mass flux of G = 7.97 kg/m^2·s to a high mas flux G = 255.04 kg/m^2·s at t = 10 ms. It indicates that the bubble generation accelerates by increasing the mass flux up to 63.76 kg/m^2·s. This trend stops by increased mass flux as steady-state conditions are reached. Although the elongated bubble span changes slightly for the mass fluxes of 63.76, 127.52 and 255.04 $kg/m^2 \cdot s$, the trapped liquid between subsequent bubbles increase as well as the mass flux.

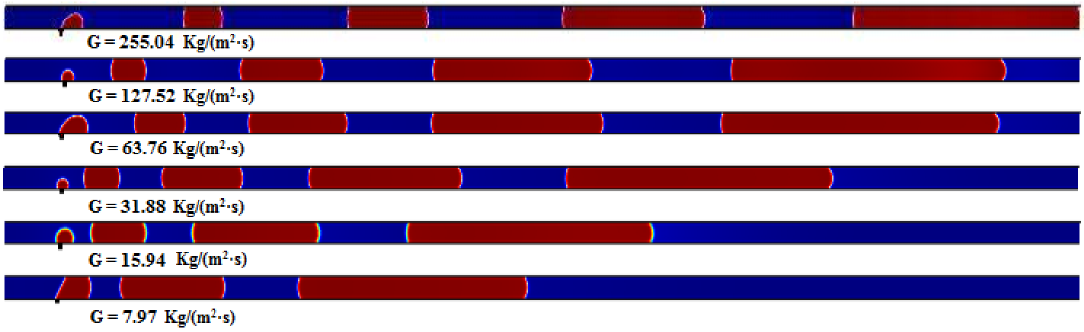

Figure 4.22 The flow pattern for different inlet mass fluxes at t = 10 ms

Figure 4.23 depicts the heat transfer performance of the heated wall of the microchannel as the flow develops thermally along the microchannel. It shows the variation of the local heat transfer coefficient and the local heat flux along the channel axis for mass fluxes of G = 32 $kg/m^2 \cdot s$ and G = 255 $kg/m^2 \cdot s$ at t = 10 ms. Generally, the removed heat flux and in accordance with that the local heat transfer coefficient are the highest around the cavity where the vapor bubble nucleates. The removed heat flux rises to more than eight times of that removed by the liquid phase alone. In contrary, at the channel locations where the elongated bubbles touch the wall, due to the low thermal conductivity of the vapor, and the very low temperature gradient, as illustrated in Figure 4.20, the removed heat flux reduces to its lowest value. The local heat flux is calculated as

$$q^{"} = -k_L \frac{\partial T}{\partial y} \tag{4.25}$$

where k_L is the thermal conductivity of the liquid.

The acceleration of the liquid slug ahead of the generating bubble from the cavity enhances the liquid-wall heat convection compared with that by the single phase liquid at the upstream. However, this effect reduces in the regions of the liquid slugs between the leading bubbles. Moreover, Figure 4.23 displays that the boiling heat transfer decreases as the flow develops thermally in the streamwise direction by decreasing the removed heat flux and the local heat transfer coefficient.

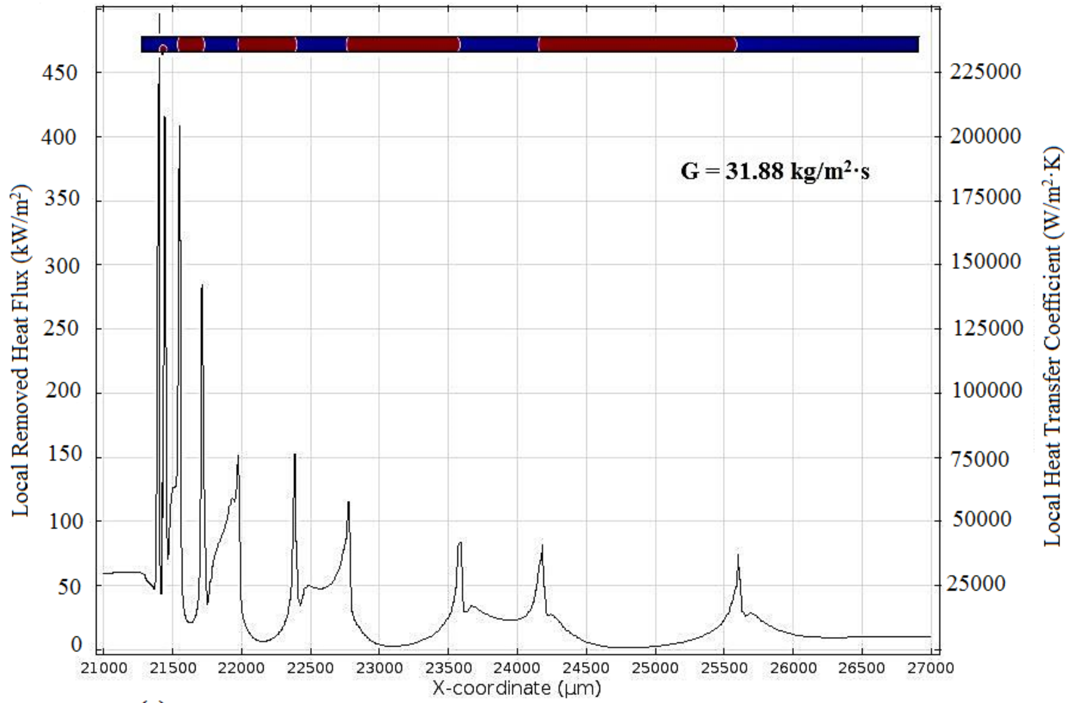

(a)

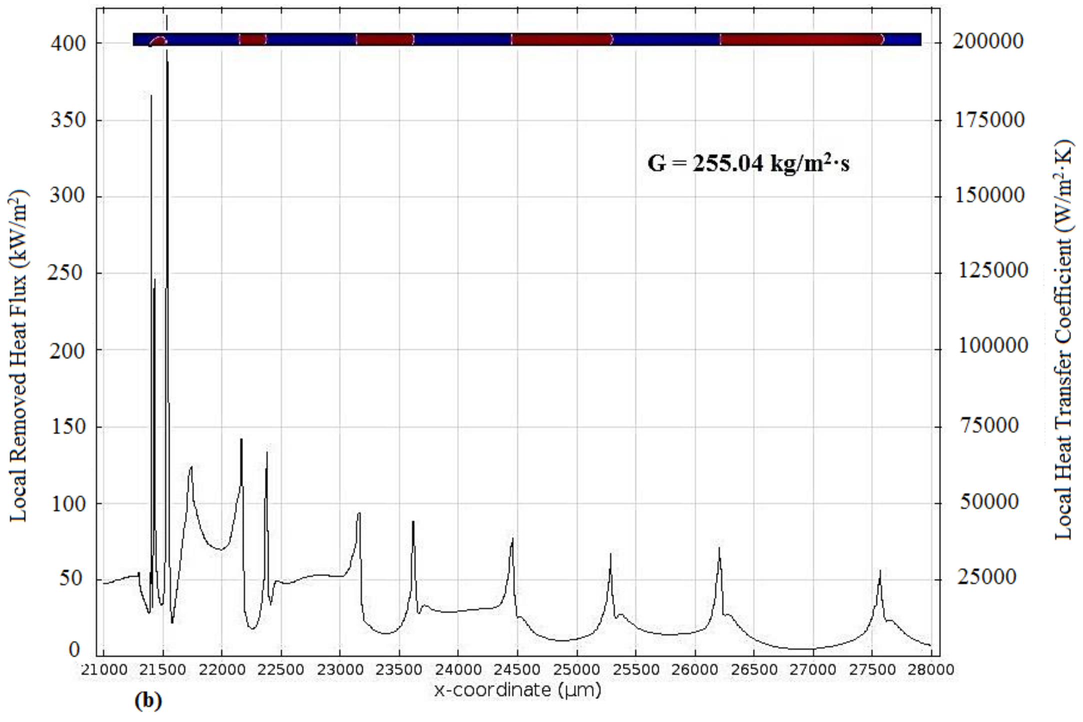

(b)

Figure 4.23 The local removed heat flux and heat transfer coefficient for the bottom wall in the flow streamwise direction for mass fluxes of (a) G = 32 kg/m$^{2}\cdot$ s and (b) G = 255 kg/m$^{2}\cdot$s at t = 10 ms

To illustrate the variation of heat transfer from the heated wall as time elapses, the heat flux and the heat transfer coefficient are plotted in Figure 4.24 at the axial location of x_p = 22000 μm. Two different mass fluxes G = 32 kg/m^2·s and G = 255 kg/m^2·s are imposed to display the effect of the inlet mass flux as well. Figure 4.24a illustrates the case of the low mass flux, G = 32 kg/m^2·s. As bubble 1approaches the axial location under investigation, the accelerated liquid ahead of the bubble enhances the liquid-wall convection and the local heat flux increases accordingly by 75%. As the nose of bubble 1 crosses x_p, the trapped liquid film between the bubble nose and the wall increases the heat transfer sharply. The heat flux falls while the bubble is crossing the desired location (x_p). At the transit of the rear of the bubble, the existence of the very thin liquid between the bubble and the wall improves the heat transfer performance again. Immediately after the transit of the bubble, the wall heat flux decreases to about half of its value for single phase flow at the beginning as the liquid slug crosses the desired location. This downward trend continues until the second bubble (Bubble 2) approaches the desired location. The process repeats periodically. The only difference appears to be the duration of the liquid slug which increases as time elapses. The evaporation from the cavity increments the pressure inside the microchannel as illustrated in Figure 4.21, and this can prolong the nucleation of the next bubble. Thus the distance between subsequent bubbles that is filled with liquid slug increases.

At the higher mass flux of G = 255 kg/m^2·s, as Figure 4.24b indicates, the accelerated liquid ahead of the evaporating Bubble 1 enhances the heat transfer more than twice. It is illustrated that the convection predominates at high mass fluxes due to increased heat removal by the liquid slugs compared to that at low mass fluxes. However, because the transit of the bubbles is much faster at high mass fluxes, the thermal boundary layer does not have enough time to rearrange to the steady-state conditions, and the heat transfer starts decreasing as time elapses.

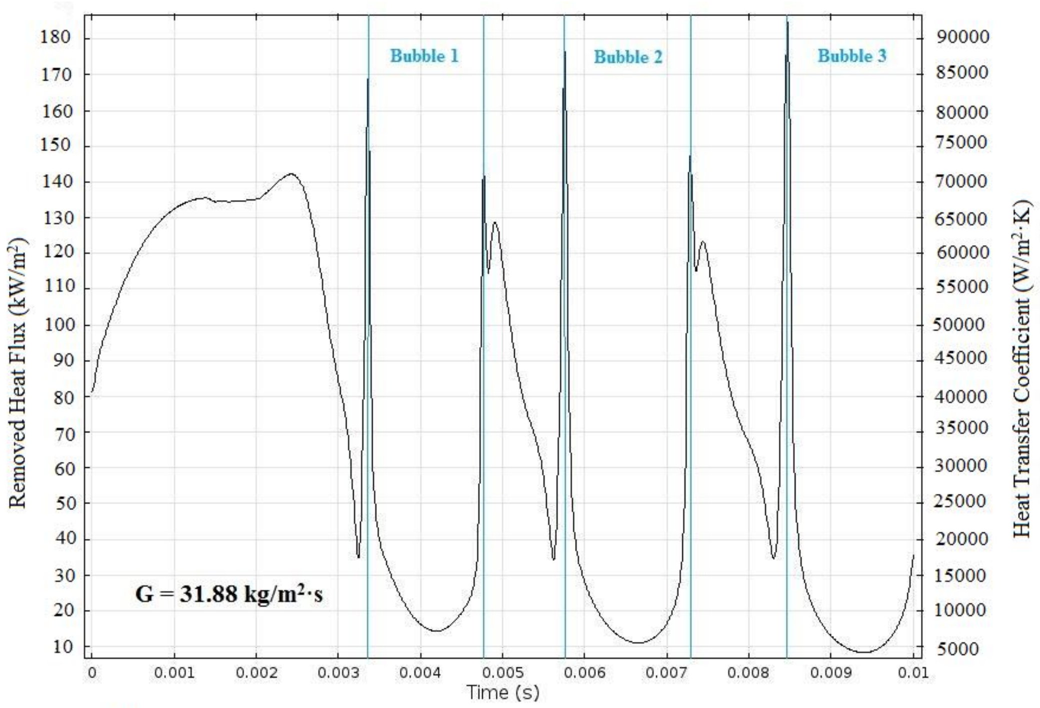

(a)

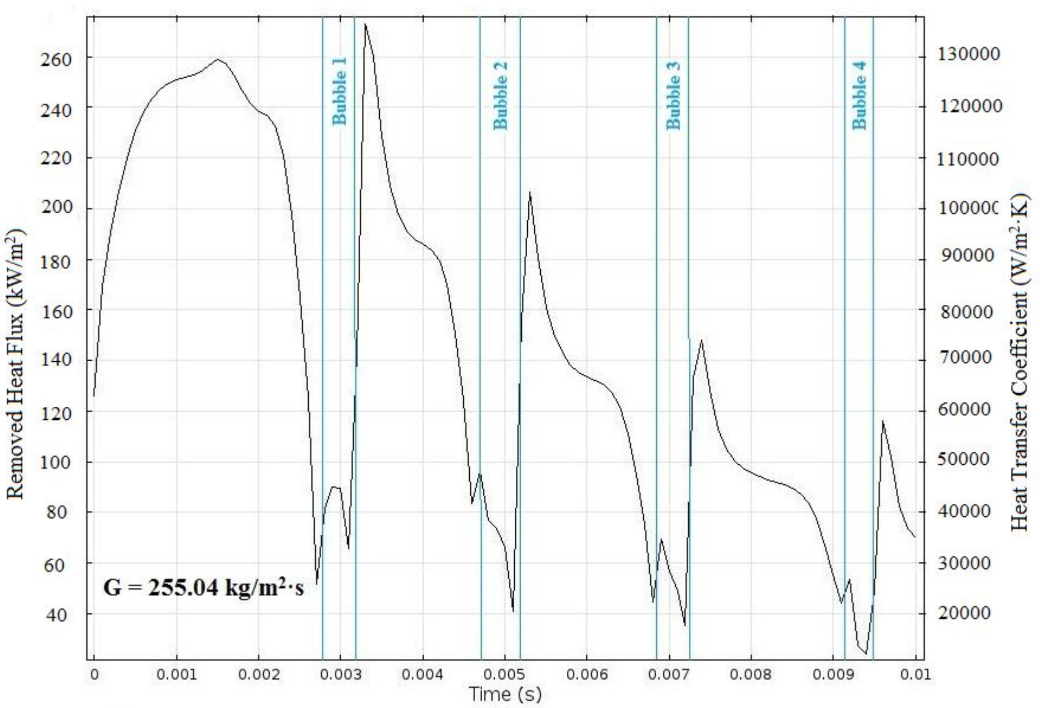

(b)

Figure 4.24 Heat transfer coefficient and removed heat flux from the bottom heated wall at x = 22 mm with two different mass fluxes of (a) G = 32 kg/m^2·s and (b) G = 255 kg/m^2·s

4.5 Simulation of the Surface Roughness Effect on Evaporation with Multi-Cavities in the Microchannels

The generated code in section 4.4 has been employed for a preliminary simulation of the surface roughness effect. Successive cavities in the shape illustrated in Figure 4.15 have been created on the bottom wall of the microchannel as shown in Figure 4.25a. Geometries of three different cavities are illustrated in Figure 4.25b. Eighty five cavities have been embedded over the total length of 1260 μm at the end of the microchannel.

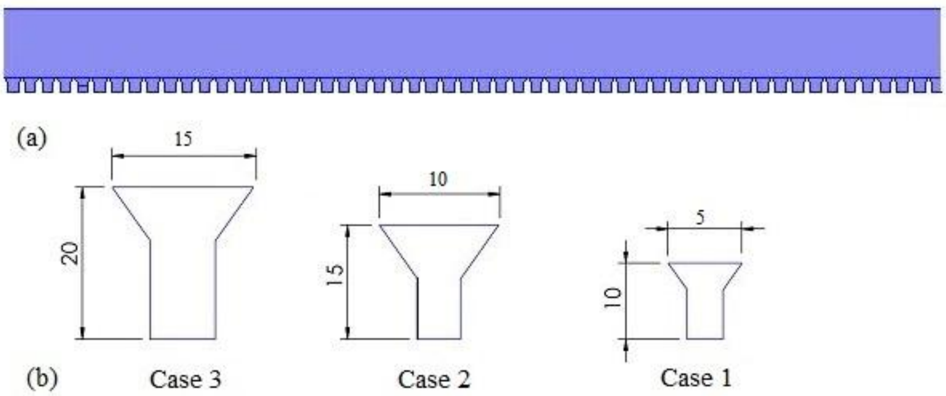

Figure 4.25 (a) Microchannel with multi-cavities (b) geometry and dimensions (μm) of three different cavities

Dimensions, initial conditions and boundary conditions are the same as the presumed parameters in the previous section, except the inlet velocity which is equal to 0.1 m/s. The simulation results show that the wall superheated is not high enough to nucleate vapor bubbles in the microchannel with the smallest cavities in case 1. On the other hand, slug flow is resulted from the generation of the elongated bubbles in two microchannels with the larger cavities. Moreover, the vaporized bubble generation rate in the microchannel with large cavities in case 3 is a little high than that in the microchannel with smaller cavities in case 2. Figure 4.26 displays the condition of the fluid flow in the microchannels at t = 15 ms. To compare the heat transfer performance of the three microchannels, quantitatively, average removed heat flux at the bottom wall of the micro channels and the pressure drop are calculated. Table 4.1 displays the results.

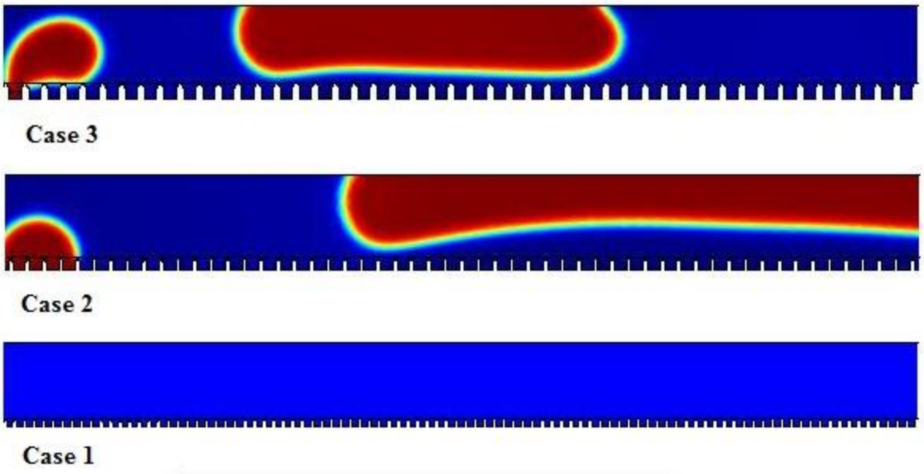

Figure 4.26 Bubble generation and movement along the microchannel for three different cavity geometries

Table 4.1Comparison of the removed heat flux at the bottom wall and pressure drop in three microchannels with different surface roughness

Microchannel	Removed Heat Flux (kW/m^2)	Pressure Drop (Pa)
Case 1	508	45
Case 2	713	45
Case 3	738	45

It is concluded from the results that the pressure drop have not changed for all of the cases. The cavities have been embedded at the end of the microchannels of length 17 mm. Hence, 1260 μm is very short compared to the whole length of the channel. Then, because of the equal boundary conditions for all of the cases, pressure drop has not altered significantly.

CHAPTER 5

FABRICATION OF MICROCHANNEL HEAT EXCHANGERS

The aim of this chapter is to describe the fabrication of microchannels to be used in heat sinks with different surface roughness. The set of specified process parameters in the WEDM are combined with the Taguchi method. The S/N ratio, ANOVA and F-test are performed to identify the significance of control factors on responses. An artificial neural network models the variation of the surface roughness based on process parameters. Furthermore, the optical microscope and SEM images of the microchannels are presented for the qualitative evaluation of the surface textures for the different surface roughness values [6690].

5.1 Micro-Evaporator Fabrication

5.1.1 The Machine Specifications

The wire cut EDM, Sodick AP250L, has been employed to carry out the experiments as shown in Figure 5.1. The machining process is divided in two sections. Initially, rough machining is performed, then finishing is done to reach the desired tolerance and surface roughness. The machining parameters are arranged automatically based on the material, surface roughness, etc. However, as the allocated surface roughness values are restricted to a few low values of R_a, the finishing operation is eliminated and the adjustable machining parameters are modified to attain different surface roughness by a roughening operation.

Figure 5.1 Sodick AP250L WEDM machine used to fabricate the micro channels (Courtesy of Center for Microsystem Design and Manufacturing Center, Bilkent University)

5.1.2 Process Parameters

The adjustable and fixed parameters of machining are shown in Table 5.1. The oxygen free copper of 99.99% purity is selected to fabricate the microchannels. A brass wire of 100 μm diameter is employed as the tool. There are different reasons for the selection of the fixed machining parameters. The wire tension has a negligible effect on the results in the literature [91,92]. The flow rate of the dielectric is not completely controllable. The low flow rates cause the short cut of the electricity because of the aggregation of the debris in the gap between the wire and the workpiece. The wire vibrates at very high flow rates. The discharge current at the gap is proportional to the capacity of a capacitance which is in the parallel circuit to the gap. Then the discharge current is eliminated from the evaluations.

Table 5.1 Adjustable and fixed parameters of machining

Adjustable parameters	Fixed Parameters
Pulse On (T_{on})	Wire Tension
Pulse Off (T_{off})	Flow Rate of the Dielectric
Main Power Supply Peak Voltage (V)	Wire Material
Feed Rate or Servo Speed (SF)	Wire Diameter
Capacitance (C)	
Wire Speed (WS)	

5.1.3 Surface Roughness Parameters

The surface roughness parameters are different and extensive. Each of these parameters determines a specific property of the surface which could be the most important one for the particular application. The surface roughness parameters are generally categorized into three groups according to their functionality: the amplitude parameters, the spacing parameters, and the hybrid parameters [42].

The amplitude parameters represent the measurement of the vertical characteristics of the surface deviations. The most universally used roughness parameters are R_a and R_z. The arithmetical average height (R_a) is the mean of the absolute ordinate values within a sampling length, and its mathematical definition is as follows:

$$R_a = \frac{1}{l}\int_0^l y(x)\ dx \tag{5.1}$$

The ten point height (R_z) is the difference in heights between the average of the five highest peaks and five lowest valleys along the assessment length of the profile. The international ISO system defines this parameter as:

$$R_z = \frac{1}{n}\sum_{i=1}^{n} p_i - \sum_{i=1}^{n} v_i \tag{5.2}$$

Since R_a and R_z are the most common parameters which are used to obtain a preliminary idea about the surface roughness, these parameters are measured in the experiments.

Furthermore, R_v has been defined as the maximum depth of the valleys. This parameter identifies the depth of potential cavities on the surface promoting evaporation.

The spacing parameters measure the horizontal characteristics of the surface deviations. For example, the mean spacing at the mean line (S_m) defines the mean spacing between profile peaks, the highest point of the profile between the peaks and valleys crossing the mean line, at the mean line. This parameter can be calculated from the following equation

$$S_m = \frac{1}{n} \sum_{i=1}^{n} S_i \qquad (5.3)$$

Regarding the evaporation, this parameter specifies the average diameter of the potential cavities on the surface. Figure 5.2 illustrates the definition of the foregoing parameters.

The hybrid parameters are combinations of the amplitude and spacing.

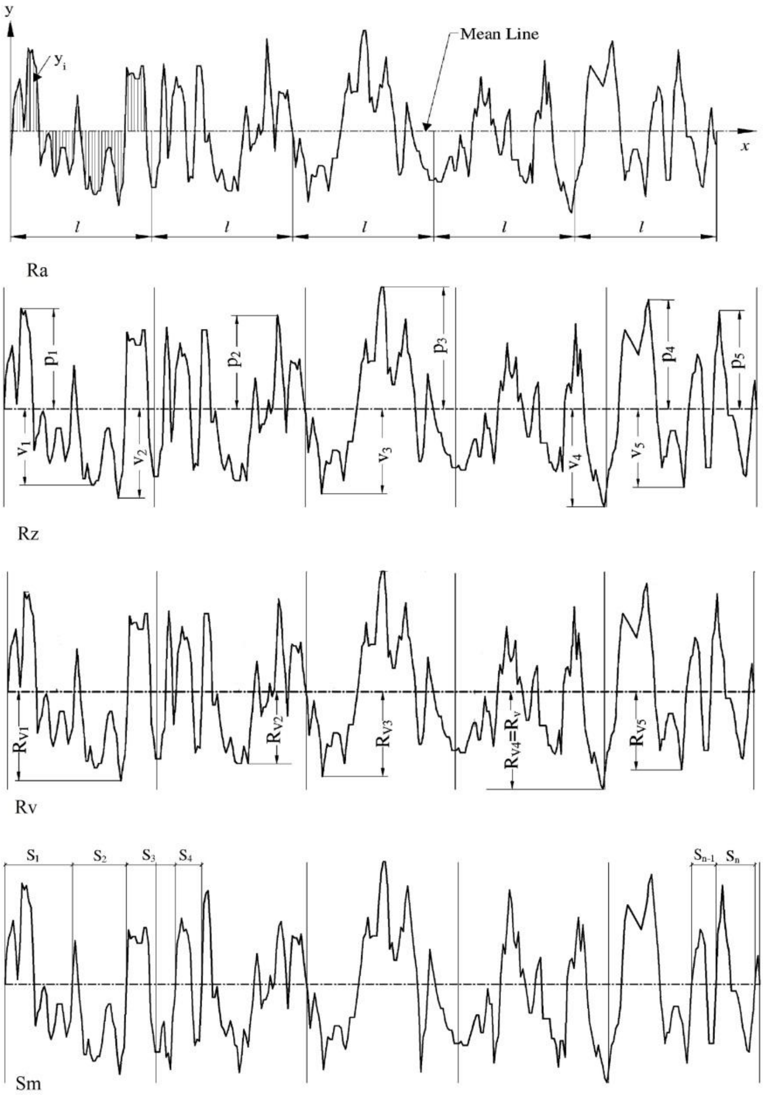

Figure 5.2 Definition of the surface roughness parameters of R_a, R_z, R_v and S_m

5.1.4 Design of Experiments with Taguchi Technique

The Taguchi method involves reducing the variation in a process through robust design of experiments. This method uses a special design of orthogonal arrays that allows studying the whole parameter space with a limited number of experiments [93].

Six adjustable process parameters are considered as variables and five discrete stages are assigned for every parameter. Table 5.2 depicts the process parameters and the intervals of the assigned levels. The levels of the process parameters are limited due to the capacity of the machine, wire breakage and short-circuiting of the wire. Experiments have been carried out using Taguchi's L25 orthogonal array experimental design which has 25 rows corresponding to the number of experiments, as shown in Table 5.3.

Table 5.2 Levels of the process parameters

Process Parameter	Level 1	Level 2	Level 3	Level 4	Level 5
T_{on} (µs)	0	1	2	3	4
T_{off} (µs)	2	10	12	15	19
V (v)	0.5	1	2	3	4
SF (mm/min)	0.5	1	1.5	2.0	2.5
C	0	1	2	3	4
WS (m/min)	2	3	4	5.5	7.5

5.1.5 Measurement of the Surface Roughness

Four surface roughness parameters, R_a, R_z, R_v *and* S_m have been measured by KEYENCE VK-X100 series laser 3D microscope and profile measurement device. A complex physical attribute, surface roughness may vary significantly according to the direction of the measurement [94]. Hence, three sections along the machining direction have been considered. At each section, five samples, each with about 200 µm length, have been averaged. Then, the average of each parameter has been taken for all three sections.

The dimensions of the microchannel are 700 µm (height) by 250 µm (width). To observe the inner surface of the microchannels via the microscope, one of the lateral walls of the microchannel is destroyed, and the other one is examined. The results of the experiments are listed in Table 5.3.

Table 5.3 Experimental design due to Taguchi method and surface roughness results

Exp. No	Process Parameters T_{on}(μs)	T_{off} (μs)	V(v)	SF(mm/min)	C	WS(m/min)	Surface Roughness Parameters R_a(μm)	R_z(μm)	R_v(μm)	S_m(μm)
1	0	2	0.5	0.5	0	2	0.94	6.67	3.00	5.30
2	0	10	1	1.0	1	3	1.07	7.47	3.22	6.56
3	0	12	3	1.5	2	4	1.24	8.63	3.55	7.56
4	0	15	4	2.0	3	5.5	1.61	10.78	4.43	8.24
5	0	19	2	2.5	4	7.5	2.09	14.21	5.85	9.85
6	1	2	1	1.5	3	7.5	1.59	10.91	4.45	10.51
7	1	10	3	2.0	4	2	1.88	13.19	5.52	7.66
8	1	12	4	2.5	0	3	1.04	8.34	3.22	5.34
9	1	15	2	0.5	1	4	1.12	8.43	3.79	5.51
10	1	19	0.5	1.0	2	5.5	1.10	7.53	3.37	7.15
11	2	2	3	2.5	1	5.5	1.21	8.51	3.82	6.04
12	2	10	4	0.5	2	7.5	1.73	12.55	5.23	7.12
13	2	12	2	1.0	3	2	1.70	12.10	5.58	6.03
14	2	15	0.5	1.5	4	3	2.25	15.89	6.23	9.12
15	2	19	1	2.0	0	4	0.90	7.03	2.88	5.46
16	3	2	4	1.0	4	4	1.92	12.41	5.36	9.70
17	3	10	2	15	0	5.5	0.96	7.36	2.90	5.96
18	3	12	0.5	2.0	1	7.5	1.14	7.52	3.24	6.08
19	3	15	1	2.5	2	2	1.25	8.45	3.79	5.94
20	3	19	3	0.5	3	3	1.80	11.31	4.88	8.28
21	4	2	2	2.0	2	3	1.29	8.67	3.63	6.56
22	4	10	0.5	2.5	3	4	1.74	12.37	4.71	8.36
23	4	12	1	0.5	4	5.5	1.95	13.88	5.87	9.08
24	4	15	3	1.0	0	7.5	1.04	8.18	3.28	4.74
25	4	19	4	1.5	1	2	1.13	7.74	3.66	5.39
26	3	12	4	2.5	3	7.5	1.63	11.51	4.86	7.81

Two microchannels of experiments 2 and 14 have been repeatedly fabricated to validate the preciseness of the experiments. The surface roughness results and the relative differences are shown in Table 5.4.

Table 5.4 Surface roughness results from the repetition of two experiments (2 and 14)

Roughness	R_a	R_z	R_v	S_m
Exp. 2 (μm)	0.96	6.80	2.97	5.88
Relative Difference %	10.14	8.97	7.84	10.49
Exp. 14 (μm)	2.38	15.86	5.57	9.05
Relative Difference %	-5.59	0.24	10.68	0.78

5.1.6 Data Analysis

Data analysis of the surface roughness parameters has been carried out using S/N ratios and ANOVA. The results listed in Table 5.3 are experienced considering Taguchi orthogonal array. The analyses have been performed on a well-known statistical software program MINITAB 17. The control parameters of the process have been determined as T_{on} (µs), T_{off} (µs), V (V), *SF* (mm/min), *C*, and *WS* (m/min). R_a, R_z, R_v and S_m have been specified as response data. In order to acquire a smooth surface, the values of the selected response parameters are desired to be low. The logarithmic function involved in the calculation of S/N ratios for the Taguchi method alters due to the objective of the optimization problem such as minimization and maximization. As the goal is the minimization of the values of response parameters, the formula used in this analysis may be shown as [95]

$$S/N = -10 \cdot log_{10}\left(\frac{y^2}{n}\right) \quad (5.4)$$

The analyses have been repeated for each response parameter to investigate the alteration of the effectiveness rank of the process parameters on responses. In order to find out the effect of each control factor on each response parameter, the main effect analysis for S/N ratios is carried out. The main effect plots of the process parameters on surface roughness parameters (R_a, R_z, R_v and S_m) are shown in Figure 5.3.

It is determined from Figure 5.3a that *C* is the most effective factor on R_a. T_{on} (µs) has second and *WS* (m/min) has third rate of effectiveness on R_a. T_{off} (µs) is designated as the least effective factor. Similarly, for R_z, *C* is again the most effective factor as may be observed from Figure 5.3. The effectiveness rates of other control factors on R_z resemble those for R_a.

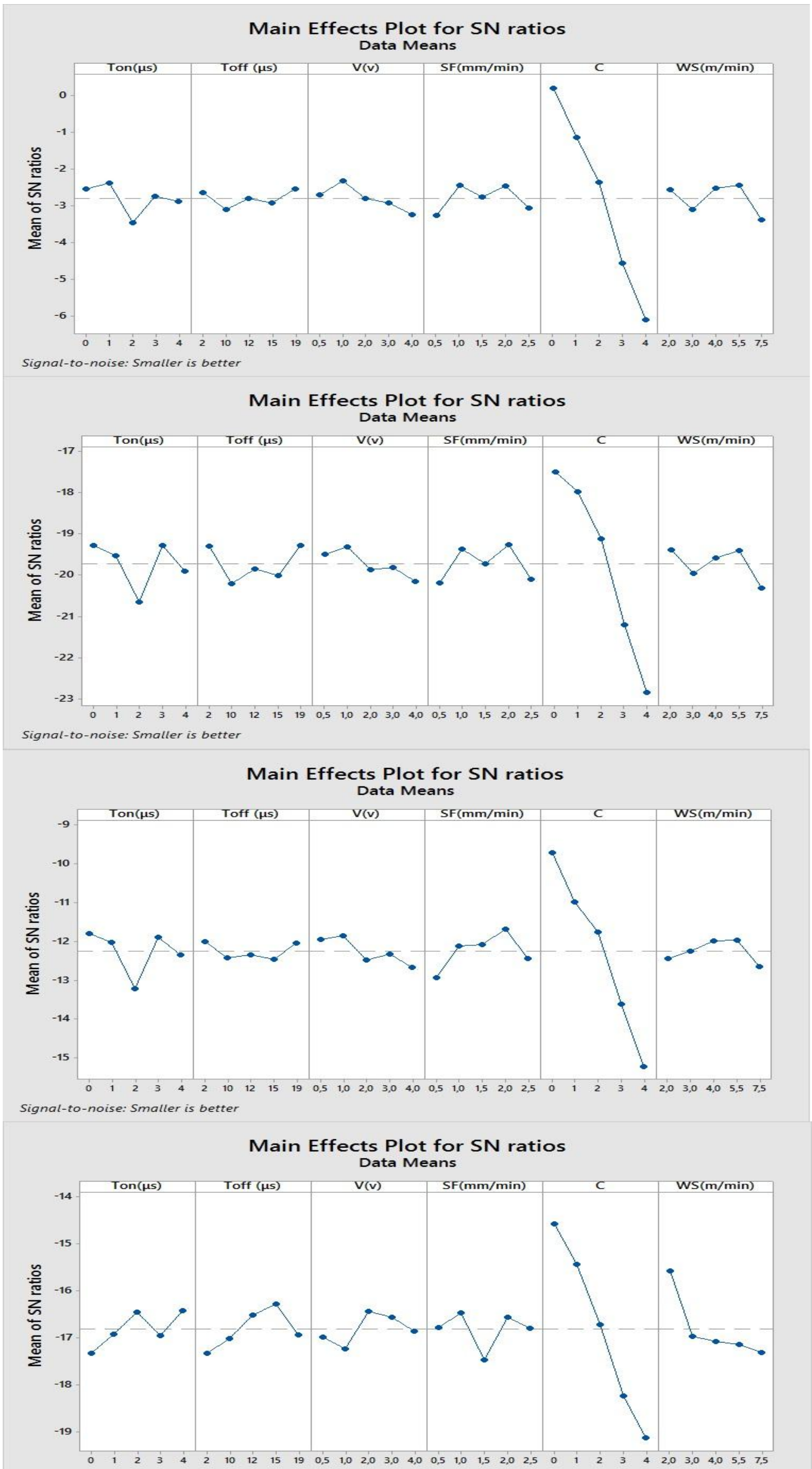

Figure 5.3 *S/N* ratio plots of (a) R_a, (b) R_z, (c) R_v and (d) S_m

5.1.7 Modeling of the Results

The artificial neural network (ANN) approach has been used to model the surface roughness based on the process parameters which are available in Table 5.3. The adjustable process parameters of T_{on}, T_{off}, V, SF, C and WS have been chosen as the inputs whereas the surface roughness parameters of R_a, R_z, R_v and S_m have been determined as the targets of the model. MATLAB, the commercial software package, has been employed for the modeling. The network has been trained based on a comparison of the outputs and the targets, until the outputs match the targets. The Bayesian Regularization Algorithm has been used in the network for the training. This algorithm typically is time consuming; however, it leads to good generalization for difficult and small datasets [96]. The training included 75% of the data (19 experiments). The validation in which the network is generalized and the training is stopped before overfitting, involved 15% (4 experiments) of data. Finally, three experiments have been used for a completely independent test of the network generalization.

The training stopped when the mean-square error of the validation falls down to its predetermined value. Figure 5.4 depicts that the mean-square error is very small for both of the training and the test.

Figure 5.5 illustrates the linear regression relation between the network outputs and the corresponding targets. The dashed and solid lines illustrate the ideal match and the best fit, respectively. The R value indicates the relationship between the output and the target with R = 1 referring to exact linear relation. It is shown that the outputs of the modeled neural network track the targets excellently for the training, the testing, and for all of the datasets. Accordingly, this network could reliably output the four surface roughness parameters with respect to the process parameters.

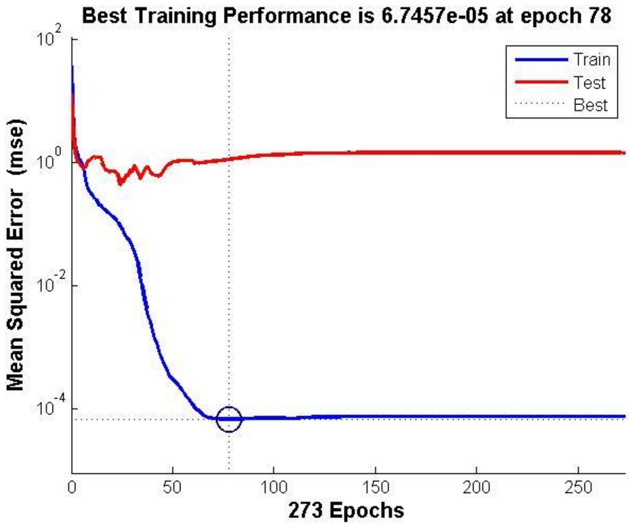

Figure 5.4 Mean squared errors of the training and the test results

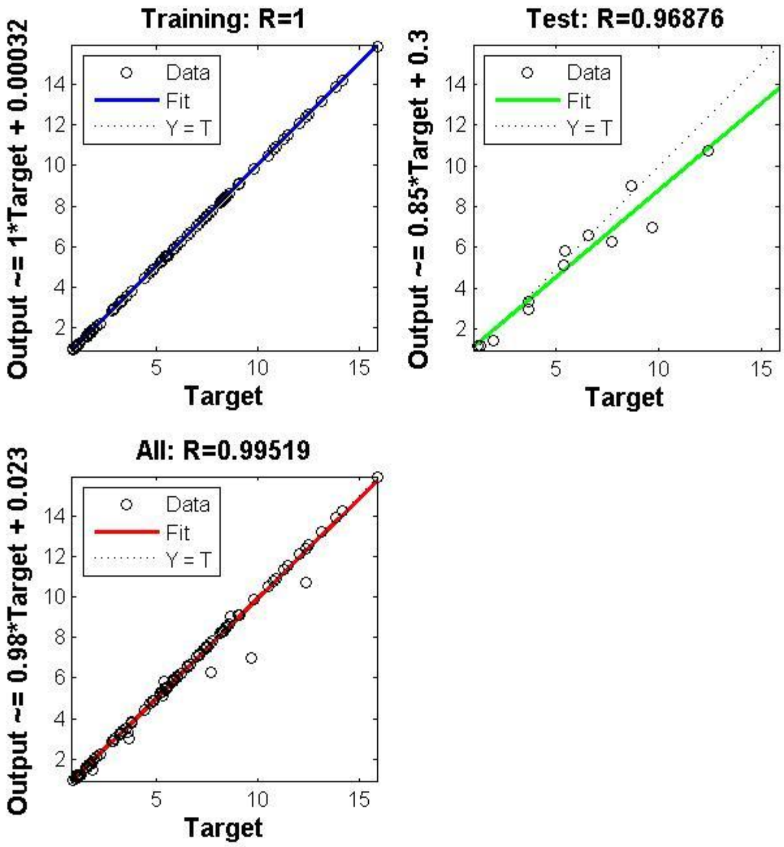

Figure 5.5 The linear regressions between the outputs and targets of the network

5.1.8 Visualization of the Surface Texture under the Optic Microscope and SEM

The surface texture strongly depends on the machining method used. For instance, sawing and milling produce narrow grooves on the surface. Regarding evaporation, the planned usage area of the microchannels, the images of the machined surfaces could clarify the potential cavities for nucleation, qualitatively.

The optical images with a magnification of 200 taken from the inner surface of the 25 microchannels have been presented in Figure 5.6. The difference of the surface form between the experiments can be identified. However, the characteristics of the surfaces such as the shapes and the sizes of the available cavities required more advanced techniques for clear recognition. A scanning electron microscope (SEM) has been utilized for the clarification.

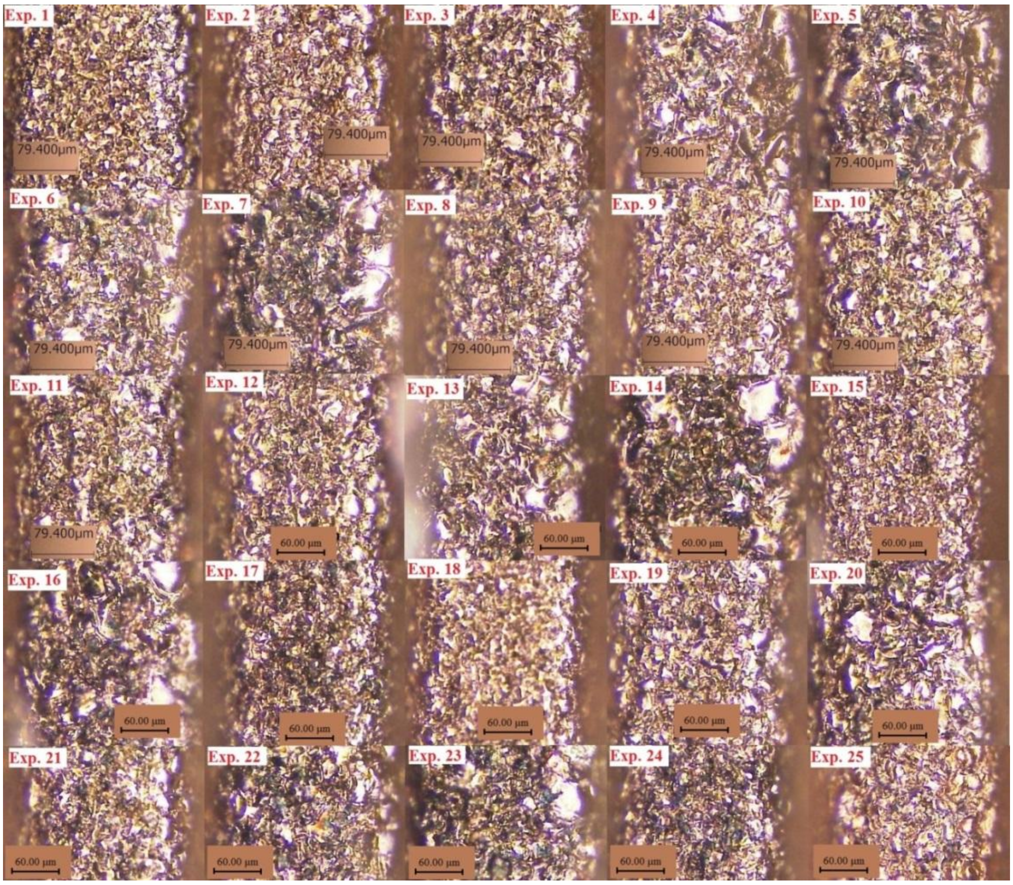

Figure 5.6 Optical images of the surfaces for the 25 experiments

Figure 5.7 illustrates the SEM images of the microchannels with the measured surface roughness parameters. The magnification of the images is 1000. It is observed that the experiments 15 and 24 with the smallest values of the surface roughness have more melted drops, crates, globules of debris and eventually smoother surfaces than the two other ones with the larger surface roughness. In other words, the size and the depth of the craters on the surfaces of experiments 6 and 14 with higher measured surface roughness parameters are perceived larger than those of the experiments 24 and 15 with smaller measured surface roughness.

The surfaces of the same experiments are represented with a further magnification of 8000 in Figure 5.8. For experiments 6 and 14, bigger and deeper cavities at the ridges of the craters are observed than those for experiments 15 and 24. It may be inferred that at the surfaces with the higher surface roughness parameters bigger and deeper cavities are attainable.

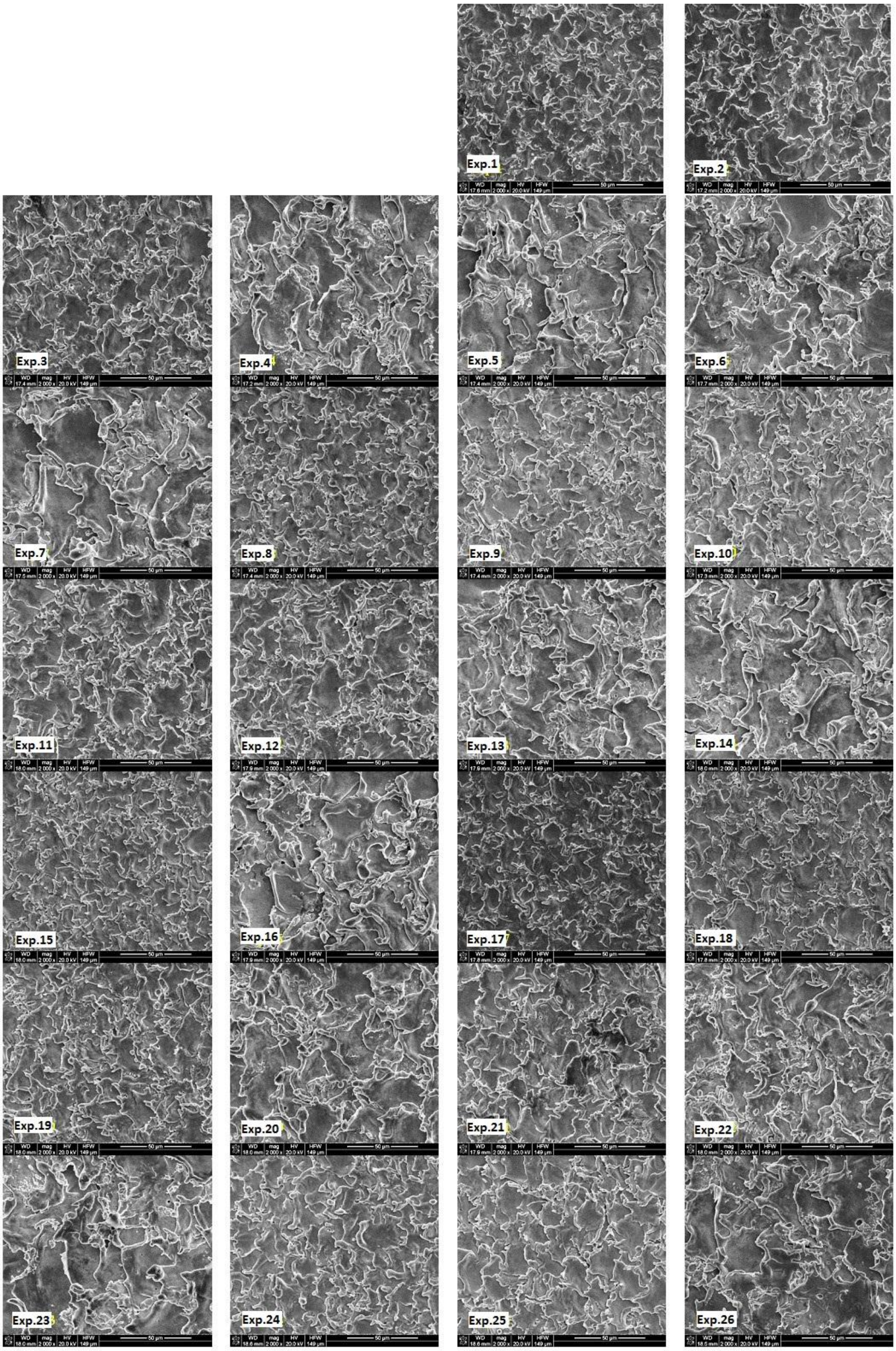

Figure 5.7 SEM images of the surfaces of microchannels

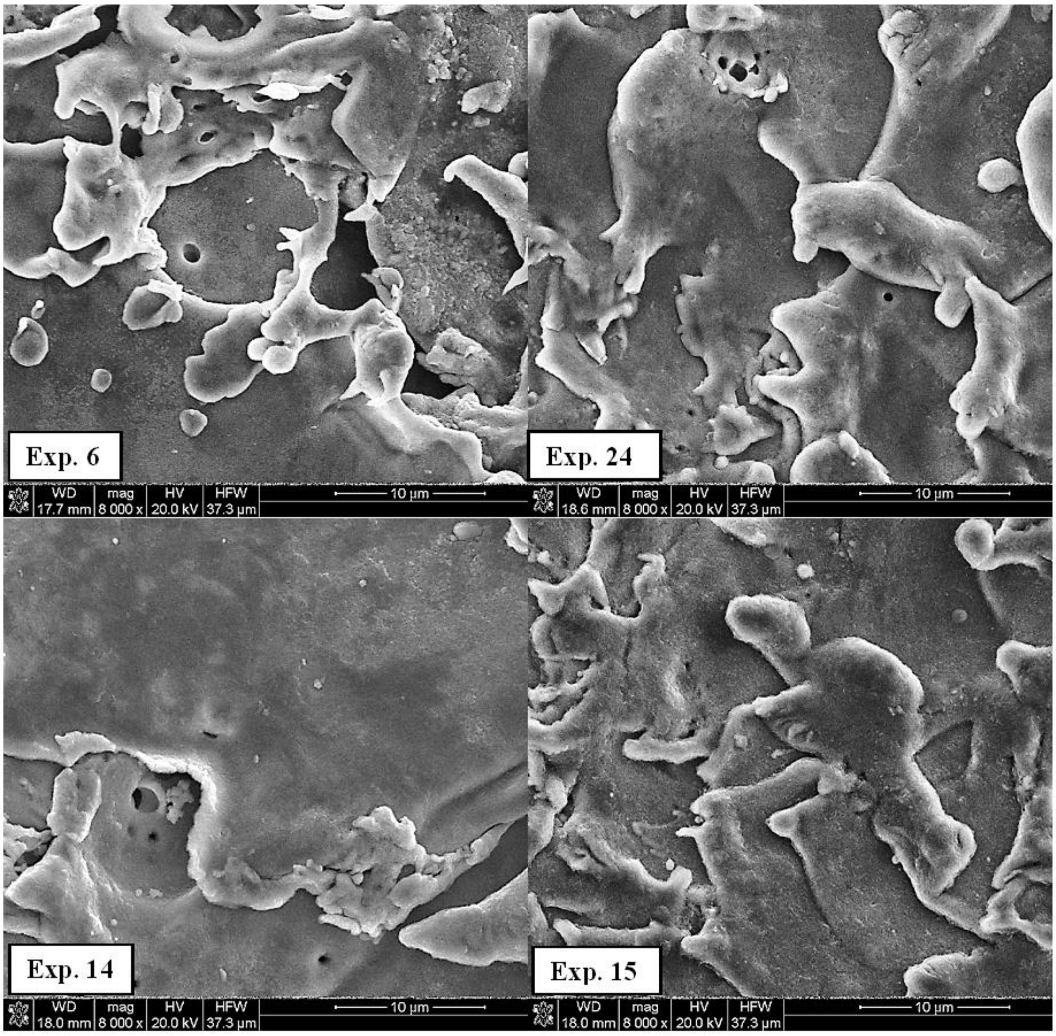

Figure 5.8 SEM images of experiments 6, 24, 14 and 15 with the magnification of 8000

5.2 Micro-Condenser Fabrication

The condenser that is used to conduct the experiments to investigate the surface roughness effects on the flow boiling is a circular copper tube a water bath. It facilitates the control of temperature ranges and cooling rates by adjusting the inlet temperature and velocity of the water.

To minimize the dimension of the refrigeration cycle and to set the cycle in a cooling package, the foregoing condenser is replaced with an aluminum condenser with microchannels. The design and analytical optimization of the micro-condenser has been made in a parallel study.

5.2.1 The Machine Specifications

Because of the formation of thin oxide layer on aluminum plates, the machining of the microchannels with electro discharge machining is difficult. For this reason, micromilling has been employed to fabricate the microchannels. DECKEL MAHO-HSC55 3 axis milling center equipped with NSKHES510-HSKA63 high speed spindle has been used.

5.2.2 Process Parameters

The spindle speed and feed rate have been adjusted to 25000 rpm and 1500 mm/min, respectively. The tool has the diameter of 500 μm, same size of the width of the microchannels. The machining operation is multipass and the depth of cut is 10 μm.

5.2.3 Visualization

Figure 5.9 displays the assembled condenser. The overall dimension of the condenser is 120 mm×30 mm×150 mm (H×W×L). Figure 5.10 illustrates the microchannels at two different magnifications. The dimensions of the microchannels are 0.5 mm×0.5 mm×150 mm (H×W×L). Brazing has been employed for the assembly of the microchannels and the fins in a vacuum furnace. The refrigerant flows in to the condenser and flows through the microchannels in a spiral path.

Figure 5.9 The condenser with microchannels

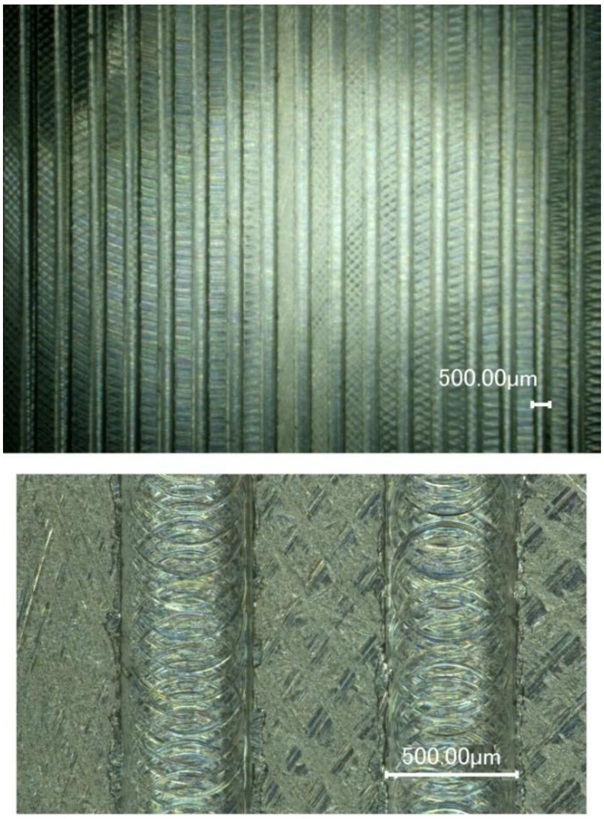

Figure 5.10 The microchannels of the condenser at two different magnifications

CHAPTER 6

EXPERIMENTAL STUDY

In this chapter, first, the components of the micro refrigeration cycle, and the experimental setup are presented. Then the heat transfer and pressure drop characteristics of the cycle with three evaporators of different surface roughness are reported. Finally, preliminary tests after the implementation of the micro-condenser are described.

6.1 Experimental Facilities

6.1.1 Test Setup

Figure 6.1 depicts the schematic diagram of the test setup constructed to carry out the experiments to investigate the surface roughness effect of the microchannels on the flow boiling performance.

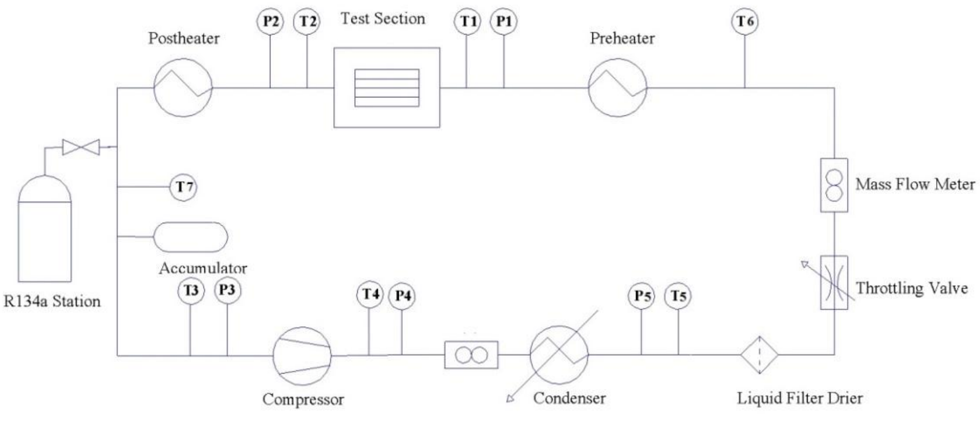

Figure 6.1 Schematic diagram of the test setup

The flow is pushed by an oil-free harmonic linear compressor with variable speed. The refrigerant is condensed to subcooled liquid state in the condenser which is a tube within a water bath with controllable temperature in the ranges of 15 to 25˚C. A liquid filter drier is installed to adsorb the humidity and system contaminations. The throttling valve is set to reach the desired pressure at the inlet of the evaporator (test section). In addition, the preheater is used to provide the desired vapor quality at the inlet of the evaporator. The refrigerant warms up through the postheater to reach the superheated state. It is necessary to ensure that only the vapor inlets the compressor. For this purpose, and also to damp out the flow fluctuations, the accumulator is installed just before the compressor. Figure 6.2 shows the photograph of the experimental setup. The DC power supply for the compressor, and the water bath supplier are not shown in the photograph.

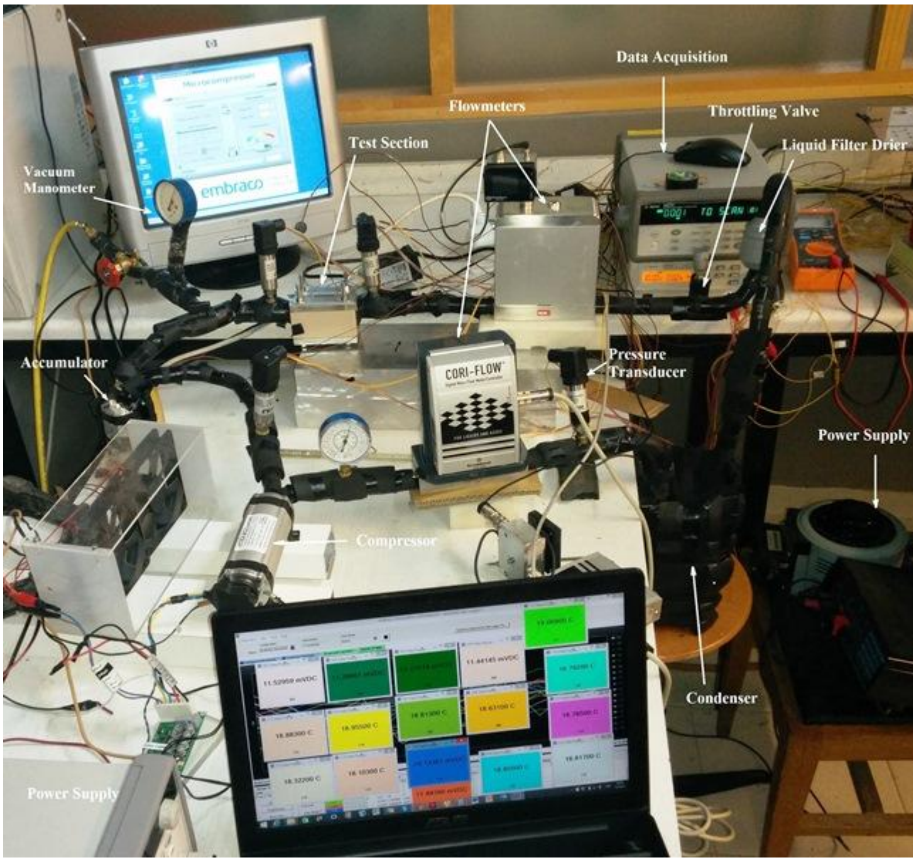

Figure 6.2 Photograph of the test setup

The experimental setup is instrumented with pressure transducers and thermocouples to measure the pressures and the temperatures, respectively. Two digital mass flow meters are installed just before the preheater and after the compressor to measure the refrigerant's flow rate. The components and their functions are presented in Table 6.1.

Table 6.1 Application and specifications of the components used in the test setup

Facility	**Application**	**Specification**
Micro compressor	Circulates the working fluid	Harmonic linear compressor manufactured by EMBRACO
Condenser	Removes the extracted heat from the evaporator	Circular copper 1/4" tube in a water bath
Accumulator	Stores the liquid to let only the saturated vapor to input in the compressor and it serves to damp out the flow fluctuations.	Material: stainless steel, dimension: Dia. 5 mm, Height: 10 mm
Throttling valve	Decreases the pressure	Manufactured by NUPRO company
Digital mass flow meter	Measures the mass flow at the inlet of the evaporator	Mini CORI- FLOW Manufactured by Bronkhorst
Gas station	Provides R134a refrigerant	
Liquid drier filter	Adsorbs system contaminations such as water and provides physical filtration	lett DFS-052S
Pressure transducer	Measures the pressure at the inlets and outlets of the evaporator and the condenser	PX4201 Manufactured by OMEGA Pressure range: 0-600 psig
Cartridge heaters	Apply uniform heat flux to the evaporator	Power range: 0-200 W
Wire heater (postheater)	Guarantees that only the vapor inputs the compressor	Power range: 0-10 W
Wire heater (preheater)	Adjusts the inlet vapor quality	Power range: 0-10 W
DC power supplies	Provides power for microcompressor, heaters and pressure transducers	Manufactured by Agilent Technologies
Data acquisition	Gathers temperatures and pressures	Agilent 34972A
Thermocouples	Measures temperatures at the inlet and outlet of the evaporator	T-type

Table 6.1 (continued)

	and condenser, and temperatures just under the bottom wall of the microchannels
Test section (Micro-evaporator)	Will be described in the next section

6.1.2 The Test Piece (Micro-Evaporator)

The test piece has been designed to contain the microchannels. Also two holes have been designed to embed the cartridge heaters to apply the heat. Figure 6.3 shows the manufactured test piece. There are 40 microchannels on the test piece. The dimensions of the microchannels are 700 μm ×250 μm × 19 mm (H×W×L). Figure 6.4 illustrates the side view of the fabricated microchannels. It is observed that microchannels have been fabricated with excellent tolerances and uniformity.

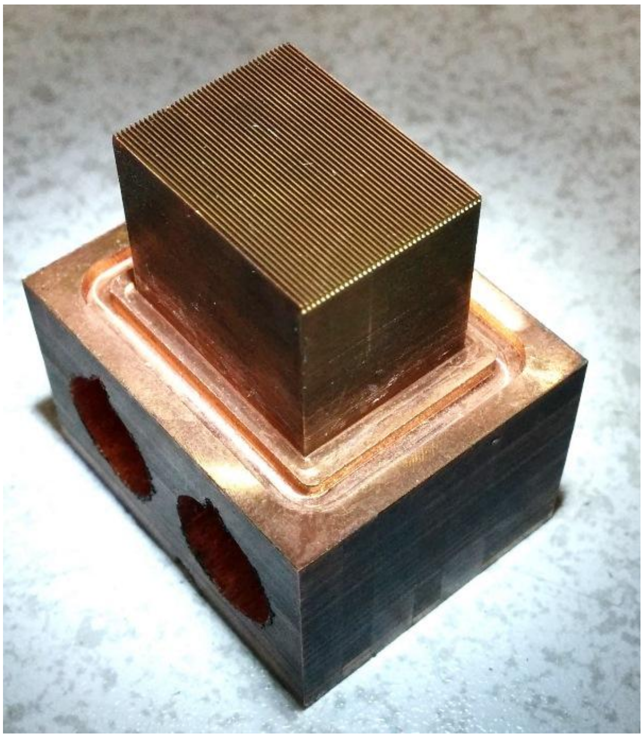

Figure 6.3 The evaporator test piece

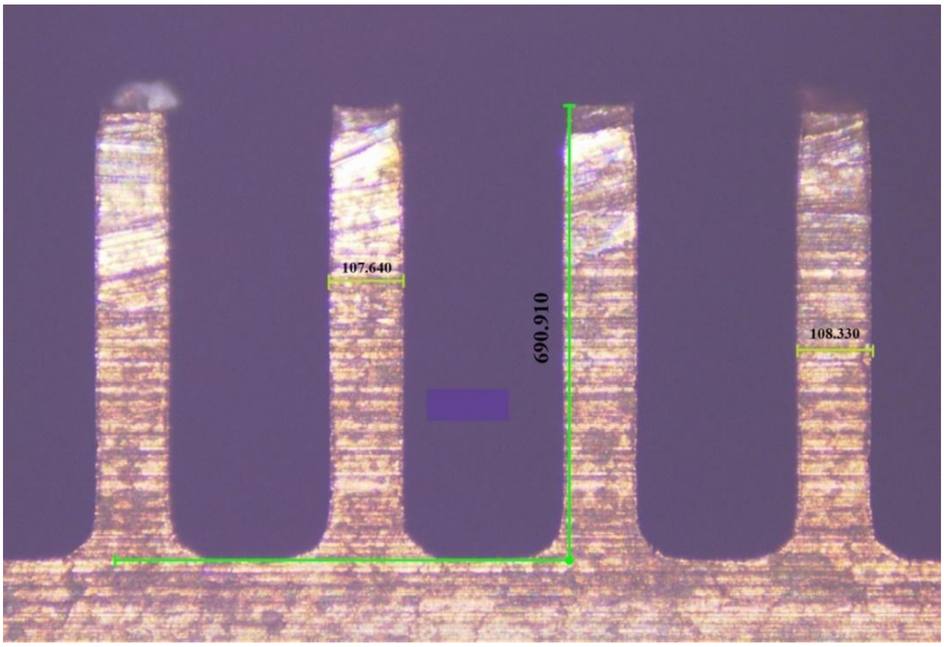

Figure 6.4 Side view of the fabricated microchannels (dimensions in μm)

Three microevaporators with three different surface roughness of microchannels have been fabricated to compare the heat transfer performance. The fabrication details have been described in section 5.1. The roughness parameters and texture of surfaces are displayed in Table 6.2 and Figure 6.5, respectively.

Table 6.2 Surface roughness parameters of the microchannels in three evaporator test pieces

Roughness	R_a **(μm)**	R_z **(μm)**	R_v **(μm)**	S_m **(μm)**
Test Piece 1	0.21	2.03	1.09	1.47
Test Piece 2	0.96	6.80	2.97	5.88
Test Piece 3	2.38	15.86	5.57	9.05

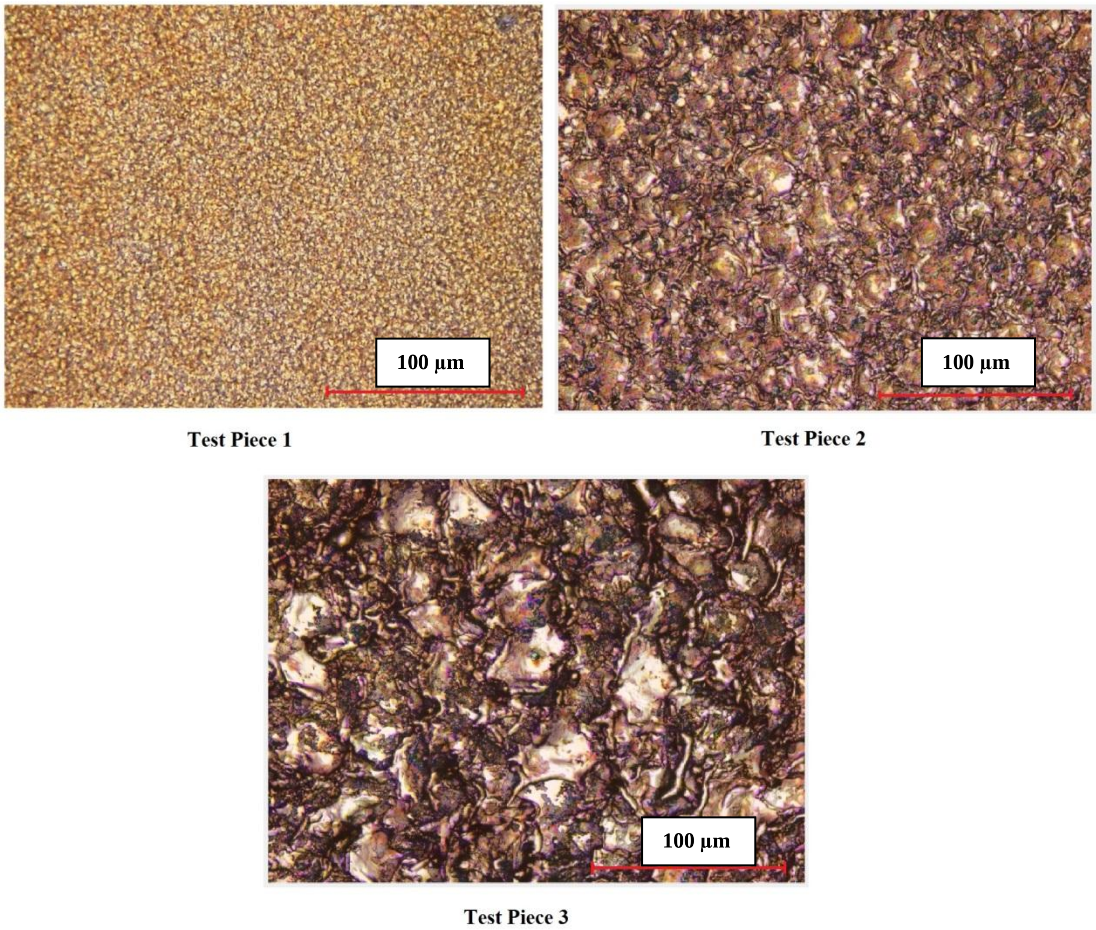

Figure 6.5 Optical microscopic images from surfaces of microchannels on three different evaporator test pieces

6.1.3 Test Section

The test section encloses the test piece to seal it as well as to measure the inlet and outlet pressures and temperatures. Furthermore, three embedded thermocouples just under the microchannels' wall measure the wall temperature at the inlet, middle and outlet of the microchannels. It is desired to calculate the heat transfer coefficient of the refrigerant along the microchannels. Therefore, the measurement of these temperatures is essential. For the observation of the flow distribution, a transparent Plexiglas has been placed at the top of the microchannels. Figure 6.6 shows the exploded view of the designed test section.

Since three microevaporators with different surface roughness have been experimented, effort has been made in the design of the test setup and especially the test section to exchange the components easily.

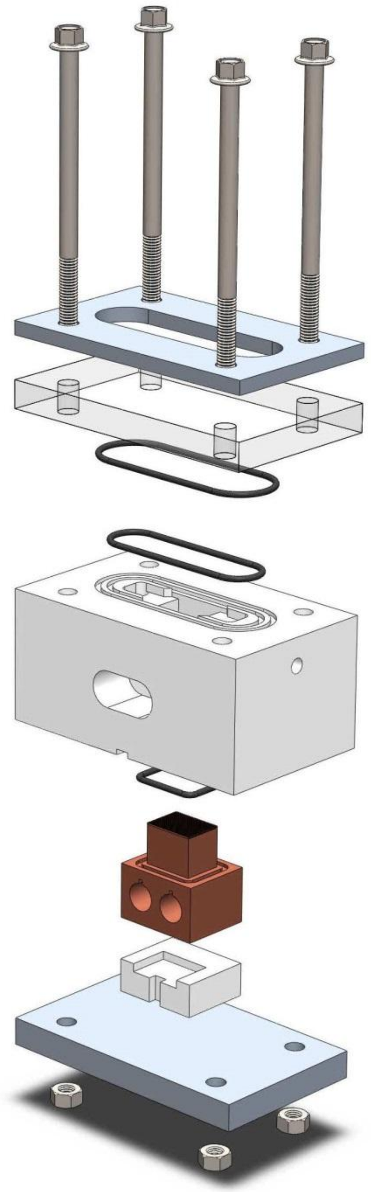

Figure 6.6 Explosive view of the evaporator test section

6.1.4 Heat Flux Distribution within the Test Section

Heat is applied in the designed evaporator through the embedded electrical heaters into the holes. A simulation has been conducted to analyze the uniformity of the heat flux under the microchannels of the designed test section. It is assumed a uniform convection is exerted on top of the microchannels, and all the lateral walls are insulated. Figure 6.7 illustrates the heat flux distribution in the test section. Figure 6.7a displays 3D total heat flux and isosurfaces by arrows and colorful planes, respectively. The conductive heat flux magnitude at the vertical plane cut through the middle of the test section is displayed in Figure 6.7b. A horizontal plane is introduced just one millimeter under the microchannels to recognize the uniformity of the heat flux, precisely. Figure 6.7c shows the conductive heat flux magnitude on the foregoing plane. The maximum relative difference is 8%.

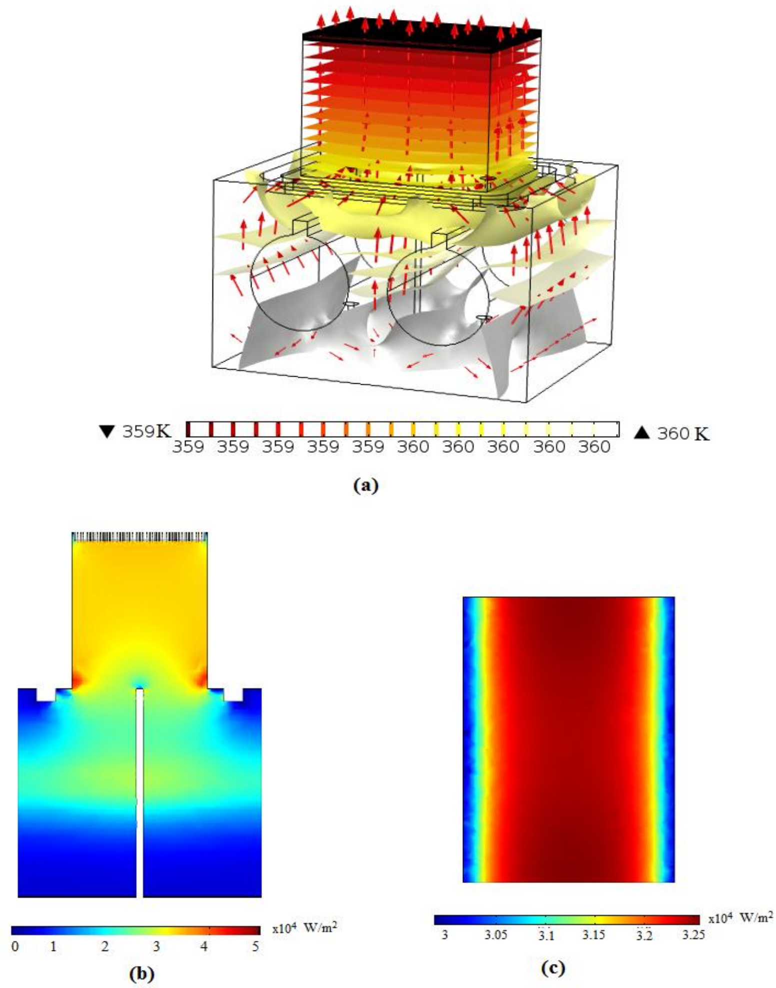

Figure 6.7 (a) Temperature distribution in the designed evaporator (b) heat flux distribution at the lateral cross section and (c) on the plane just one millimeter under the microchannels

Data Reduction

The base heat flux, $q^{"}$, is defined as

$$q^{"} = \frac{Q}{L \cdot W} \tag{6.1}$$

where L and W are length and width of the base wall of the microchannels, respectively. Q is the applied heat from the cartridge heaters which is calculated as

$$Q = V \cdot I \tag{6.2}$$

Where V and I are applied voltage and current, respectively.

Three thermocouples have been embedded just two millimeter under the microchannels' wall to measure the wall temperature at the inlet, middle and outlet of the microchannels. Thus the wall temperature, T_{surf}, is calculated as

$$q'' = k \frac{\Delta T}{\Delta x} \tag{6.3}$$

$$T_{\text{surf}} = T_{\text{measured}} + \frac{q'' \Delta x}{k} \tag{6.4}$$

Where k is thermal conductivity of the copper and Δx = 2 mm.

Heat transfer coefficient is defined as

$$h = \frac{q''}{T_{surf} - T_{sat}} \tag{6.5}$$

$T_{\text{surf, in}}$, $T_{\text{surf, mid}}$ and $T_{\text{surf, out}}$ are bottom wall temperatures at inlet, middle and outlet of the microchannels, respectively. T_{sat} is the saturation temperature of the refrigerant.

The efficiency of the evaporator is expressed in terms of the coefficient of performance (COP). The objective of the cycle is to remove heat (Q_L) from the test piece. To accomplish this objective, it requires a work input of $W_{\text{compressor}}$. Then the COP of a refrigerator can be expressed as [97]

$$COP = \frac{Q_L}{W_{\text{compressor}}} \tag{6.6}$$

6.2 Energy Balance of the Cycle with the First Law of Thermodynamics

For the energy balance of the constructed micro refrigeration cycle and validation of the obtained experimental results, the law of conservation of energy is applied. The measured temperatures and pressures at different points of the cycle are illustrated in Table 6.3. The applied heat to the evaporator and measured mass flow rate are 50 W and 0.7 g/s, respectively. The work done by the compressor, and the heat applied to the evaporator and by the post heater should be equal to the dissipated heat in the condenser.

Table 6.3 Temperatures and Pressures at Various States of the Cycle at Q = 50 W

State	Position	Pressure (bar)	Temperature (°C)
1	Evaporator-inlet	4.2	9.9
2	Evaporator-outlet	4.2	10.0
3	Condenser-inlet	6.7	29.4
4	Condenser-outlet	6.7	24.1
5	Compressor-inlet	4.2	18.3
6	Compressor-outlet	6.7	29.8

The work done by the compressor is assumed to be equal to the exerted total electrical power to the compressor minus the exerted electrical power for cooling fans which manufacturer has put to cool down the compressor shell. Then

$$W_{\text{compressor}} = W_{\text{compressor-total}} - W_{\text{cooling fans}}$$

Applied voltage and current are V = 24 V and I = 1.08 A, respectively. Then

$$W_{\text{compressor-total}} = 25.92 \text{ W}$$

$$W_{\text{cooling fans}} = 13 \text{ W}$$

$$W_{\text{compressor}} = 12.92 \text{ W}$$

The applied heat to the test piece and the post heater are

Q_L = 50 W

$Q_{\text{postheater}}$ = 31.8 W

The total supplied energy to the cycle will be

$E_{\text{in}} = W_{\text{compressor}} + Q_{\text{L}} + Q_{\text{postheater}}$

E_{in} = 94.72 W

The removed heat from the cycle would be calculated from the inlet and outlet states of the condenser. Then

$$Q_{\text{out}} = m(h_{\text{condenser-in}} - h_{\text{condenser-out}})$$

Q_{out} = 0.7(380.17-233.18) W

Q_{out} = 102.89 W

$E_{\text{out}} = Q_{\text{out}}$

The energy balance can be expressed as

$E_{\text{in}} - E_{\text{out}}$ = -8.17 W

Which infers the relative difference between the input and output energies to the system is 8%. The reason is believed to be the presumption fully insulated system. The surrounding temperature is measured as 23.95°C whereas the saturation temperature is set to 10°C. Therefore, there is heat gain to the system which is quite unavoidable.

6.3 Vapor Quality Calculation in the Test Section

The state at the inlet of the compressor is superheated vapor. According to Table 6.3 the enthalpy of R134a at the inlet of the compressor will be 427.92 kJ/kg. The total applied heat at the test section and postheater is 81.8 W. With a mass flow rate of 0.7 g/s, this heat results in an enthalpy of 116.85 kJ/kg. The enthalpy at the inlet of the test section will be the difference of the two. Therefore, the vapor quality, x, at the inlet of the evaporator is calculated as

$$i = i_{\mathrm{f}} + x i_{\mathrm{fg}} \tag{6.6}$$

Where i, i_f and i_{fg} are enthalpies at the inlet of the evaporator, the liquid and difference of liquid and vapor, respectively. Eventually, the vapor quality is estimated as 0.5. Figure 6.8 displays the state points of the refrigeration cycle on the pressure-enthalpy diagram. There are liquid filter dryer, throttling valve and flowmeter between the output of the condenser (state 4) and input of the evaporator (state 1) without perfect insulation. Since this region would be the place in where the most of the calculated heat gain transfers to the cycle, dashed line is used to illustrate the path behavior from state 4 to state 1. Therefore, the state point of 4 would vary within the circle shows in Figure 6.8.

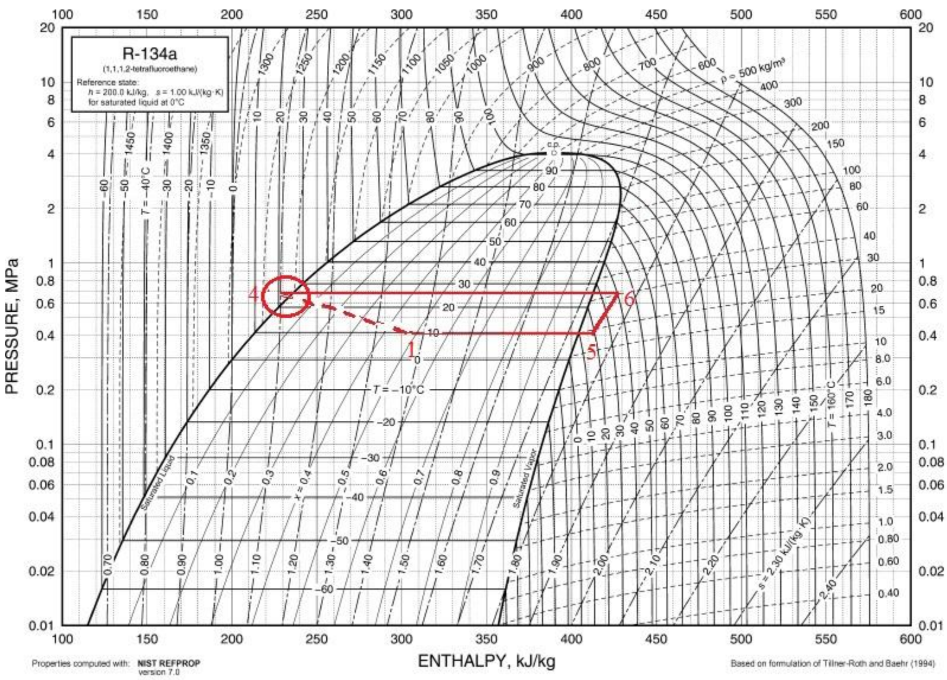

Figure 6.8 Pressure-enthalpy diagram of the refrigeration cycle

6.4 Uncertainty Analysis

The uncertainties in the results may be calculated using the theory of the propagation of error. The uncertainty U_{F} on a quantity F, which is a function of measured variables $x_1, \dots, x_n$ with an associated uncertainty U_{xi} can be expressed as follows [98]

$$U_F = \pm \sqrt{\sum_{i=1}^{n} \left(\frac{\partial F}{\partial x_i} U_{x_i}\right)^2} \qquad (6.7)$$

with a corresponding relative uncertainty of $\delta F = U_F / F$. Accordingly, the uncertainty in the heat transfer coefficient, Equation 6.7, would be expressed as

$$\delta h = \sqrt{\left(\frac{\delta q"}{T_{\mathrm{surf}} - T_{\mathrm{sat}}}\right)^2 + \left(\frac{q" \delta T_{\mathrm{surf}}}{(T_{\mathrm{surf}} - T_{\mathrm{sat}})^2}\right)^2 + \left(\frac{q" \delta T_{\mathrm{sat}}}{(T_{surf} - T_{\mathrm{sat}})^2}\right)^2}$$

From Equation 6.1, $\delta q"$ is calculated as

$$\delta q" = \sqrt{\left(\frac{\delta V\, I}{WL}\right)^2 + \left(\frac{V \delta I}{WL}\right)^2 + \left(\frac{VI\delta W}{W^2 L}\right)^2 + \left(\frac{VI\delta L}{WL^2}\right)^2}$$

The uncertainty in the pressure drop of the microchannels is

$$\delta \Delta P = \sqrt{\delta P_{\mathrm{in}}{}^2 + \delta P_{\mathrm{out}}{}^2}$$

For the COP of the cycle, the uncertainty is calculated as

$$\delta \mathrm{COP} = \sqrt{\left(\frac{\delta V_1\, I_1}{V_2 I_2}\right)^2 + \left(\frac{V_1 \delta I_1}{V_2 I_2}\right)^2 + \left(\frac{V_1 I_1 \delta V_2}{V_2{}^2 I_2}\right)^2 + \left(\frac{V_1 I_1 \delta I_2}{V_2 I_2{}^2}\right)^2}$$

Where V_1, I_1, V_2 and I_2 are applied voltages and currents to the cartridge heaters and the compressor, respectively.

The measurement uncertainty for the sensors, measuring devices and the reported results are listed in Table 6.4.

Table 6.4 Uncertainty results

Name	Uncertainty
V	±0.01% (V)
I	±0.01% (A)
W	±10 (μm)
L	±20 (μm)
T_{surf}	±0.1 (°C)
T_{sat}	±0.1 (°C)
P_{in}	±0.1 (bar)
P_{out}	±0.1 (bar)
q''	0.1%
h	27% at Q = 5 W 12% at Q = 10 W 4% > at Q = 20 W and higher heats
ΔP	1.4 kPa
COP	7% at flow rate of 85 kg/m^2·s 1.5% at flow rate of 200 kg/m^2·s

6.5 Experimental Results

In this section, the experimental flow boiling heat transfer and pressure drop results obtained using the microchannel evaporators of three different surface roughness are presented and discussed. The saturation temperature at the inlet of the test section is maintained at approximately 10°C. Two mass fluxes of G = 85 kg/m^2·s and 200 kg/m^2·s are adjusted. These two mass fluxes have been selected based on the upper and lower limitations of the compressor and the throttling valve at the saturation temperature of 10°C. The base heat flux is ranged from 1 W/cm^2 to 48 W/cm^2.

6.5.1 Wall Heat Transfer Coefficient

Surface roughness effects on heat transfer coefficient as a function of the base heat flux are presented in Figure 6.9-6.12.

Figure 6.9 and 6.11 illustrate the local heat transfer coefficient with respect to the base heat flux at the mass flux of G = 85 kg/m^2·s with the vapor qualities of 0.5 and

0.3, respectively. The heat transfer coefficient increases with increasing surface roughness in both cases. The heat transfer coefficient rises up to 40% as the surface roughness increases from test piece 1 to test piece 3. Also the heat transfer coefficient steadily grows by increasing the applied heat flux. This trend agrees with available data in the literature except at low heat fluxes. The reason for this inverse behavior is possibly due to the high uncertainty at low heat fluxes. The results indicate that the critical heat flux increases as the surface roughness increases. The circle markers display the critical heat fluxes.

Visual observation strongly discloses instability and nonuniformity in the fluid flow at mass flux of G = 85 kg/m^2.s.

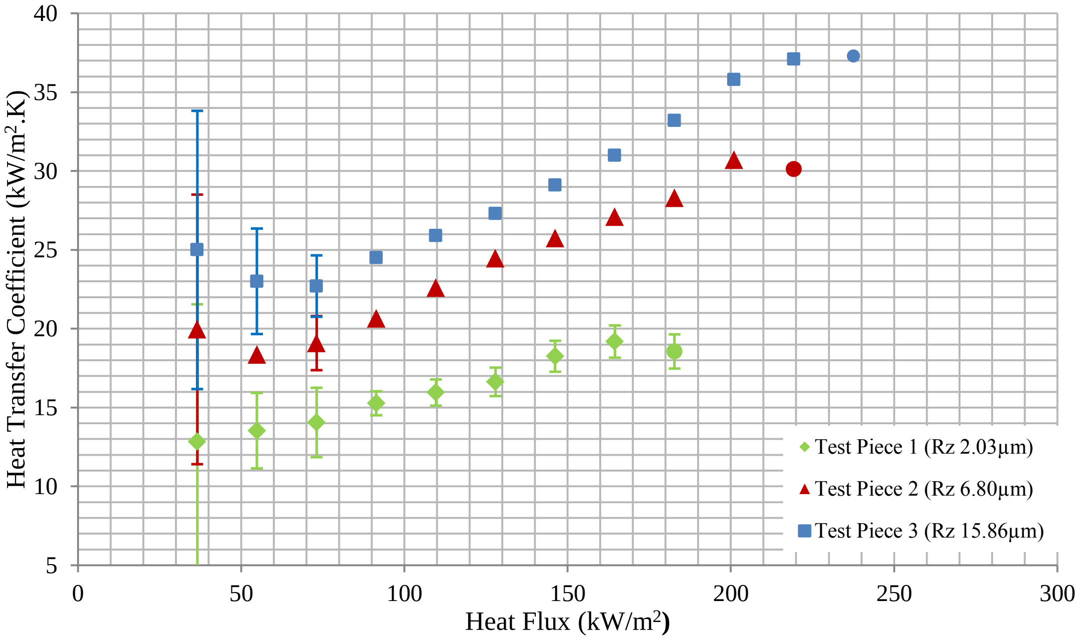

Figure 6.9 The effect of microchannels' surface roughness on heat transfer coefficient with a mass flux of G = 85 kg/m^2·s and inlet vapor quality of x = 0.5

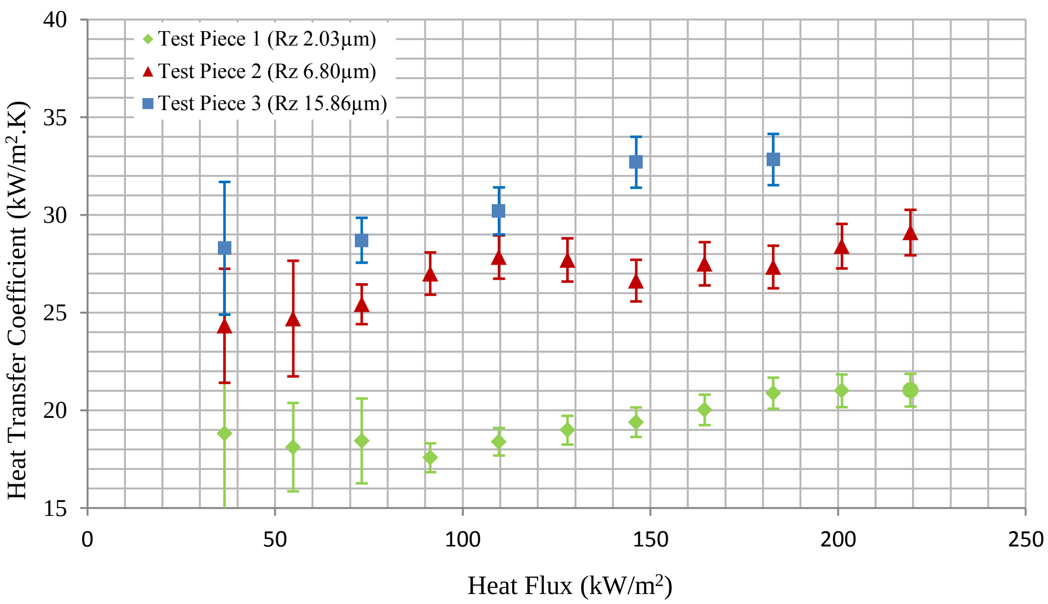

Figure 6.10 The effect of microchannels' surface roughness on heat transfer coefficient with a mass flux of G = 85 kg/m^2·s and inlet vapor quality of x = 0.3

Figure 6.11and 6.13 display the local heat transfer coefficient versus the base heat flux at mass flux of G = 200 kg/m^2.s and the vapor qualities of 0.5 and 0.8, respectively.

As Figure 6.11 shows the heat transfer coefficient rises whilst increasing the surface roughness. It increases up to 45%, a slight increase compared to the heat for the mass flux of G = 85 kg/m^2.s, as the surface roughness increases from test piece 1 to test piece 3. Since the fluid flow is much more uniform and stable than that with the lower mass flux, a higher heat flux could be applied. With a similar trend, the heat transfer coefficient grows as the applied heat flux increases except at low heat fluxes.

However, Figure 6.12 demonstrates that the heat transfer coefficient does not alter by changing the surface roughness for the large vapor quality of 0.8. In addition, the heat transfer coefficient decreases drastically with increased heat flux. The decrease in the heat transfer coefficient reduces as the applied heat flux increases. To avoid the film boiling, the experiments were performed at very low heat fluxes.

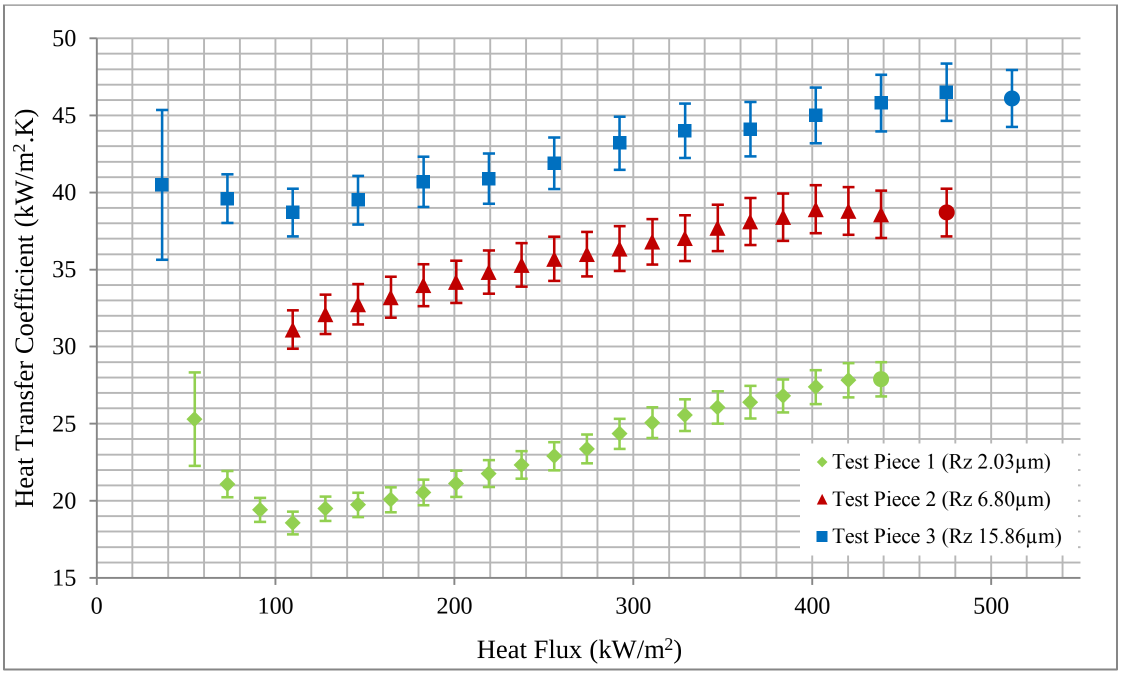

Figure 6.11 The effect of microchannels' surface roughness on heat transfer coefficient with a mass flux of G = 200 kg/m^2·s and inlet vapor quality of x = 0.5

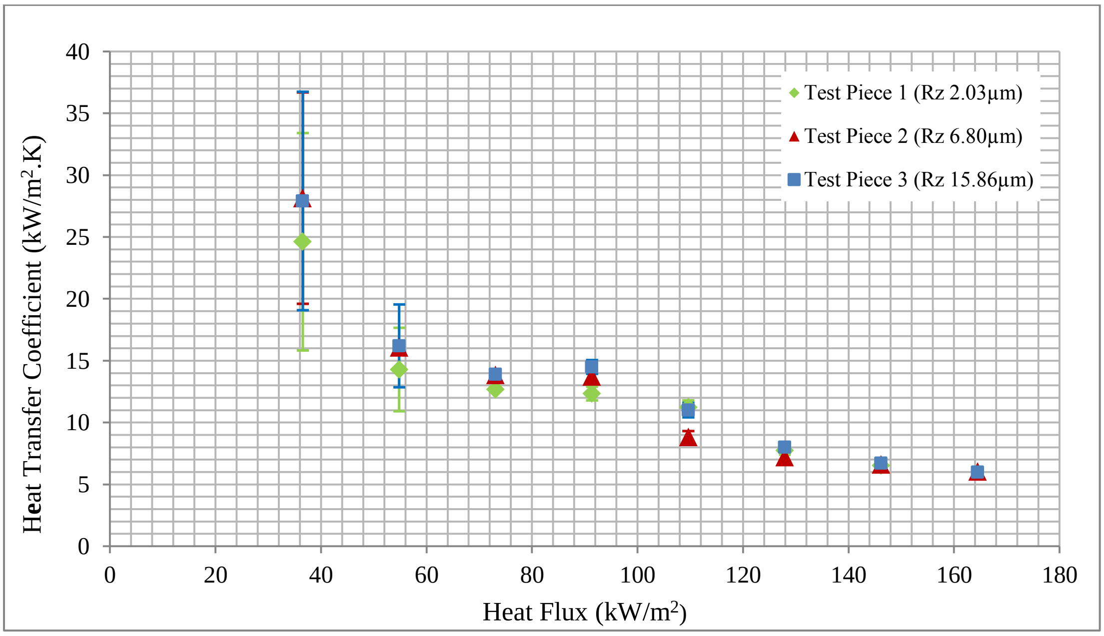

Figure 6.12 The effect of microchannels surface roughness on heat transfer coefficient with a mass flux of G = 200 kg/m^2·s and inlet vapor quality of x = 0.8

6.5.2 Pressure Drop

Since two pressure transducers have been installed at the inlet and outlet of the test section, the overall pressure drop including the inlet restriction pressure drop, the microchannels pressure drop and the outlet pressure drop has been measured.

Figure 6.13 and 6.15 illustrate the total pressure drop with respect to the base heat flux for three evaporators with different surface roughness with two different mass fluxes of G = 85 kg/m^2·s and G = 200 kg/m^2·s, respectively. The total pressure drop increases by increasing the surface roughness of the microchannels. The maximum difference pressure drop is 38% with the mass flux of G = 85 kg/m^2·s. Also it is inferred that the pressure drop increases approximately linearly with the heat flux. As it is expected the total pressure drop with the mass flux of G = 200 kg/m^2·s for all the surface roughness is higher than the pressure drop with the mass flux of G = 85 kg/m^2·s.

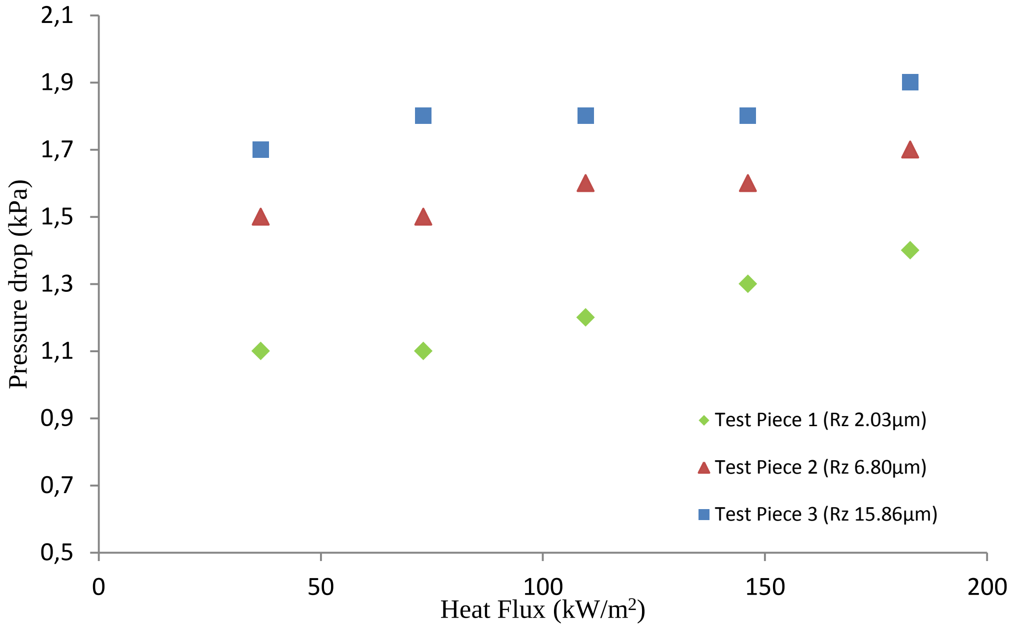

Figure 6.13 Total pressure drop for the mass flux of G = 85 kg/m^2·s and inlet vapor quality of x = 0.5

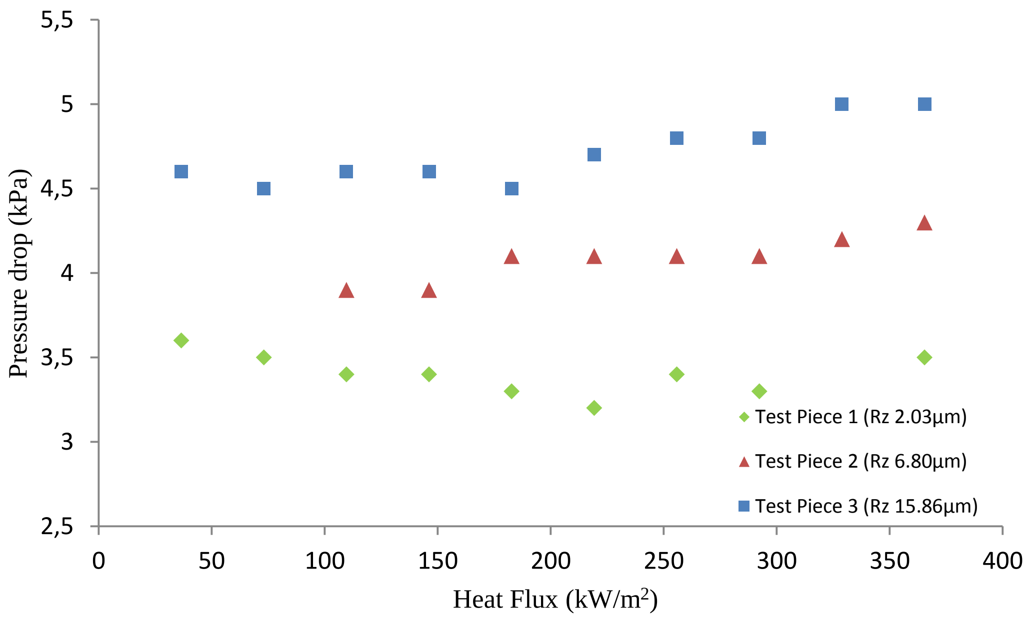

Figure 6.14 Total pressure drop for the mass flux of G = 200 kg/m^2·s and inlet vapor quality of x = 0.5

6.5.3 Coefficient of Performance (COP)

The COPs of the cycle for three test pieces (evaporators) with different surface roughness with respect to the heat flux are presented in Figure 6.15. The COP increases linearly with the heat flux for both of the mass fluxes. The development of the COP with the mass flux of G = 85 kg/m^2·s is sharper than the mass flux of G = 200 kg/m^2·s. A COP of 4 is achieved at a low heat flux of 18 W/cm^2 with G = 85 kg/m^2·s whereas the COP of 2.6 is attained at a medium heat flux of 43 W/cm^2 with G = 200 kg/m^2·s. $COP_{reversible} \cong 14$ and 10, respectively, for the low and medium heat fluxes which indicates that with the optimization of the cycle, higher COP values may be attained.

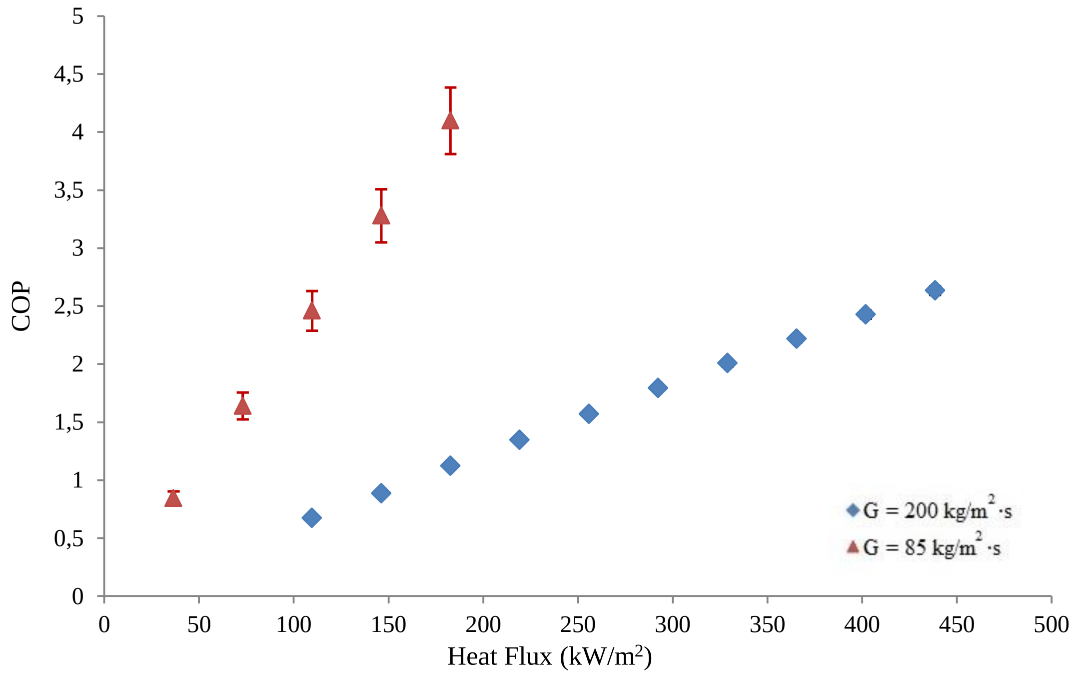

Figure 6.15 COP of the micro refrigeration cycle with two different mass fluxes

Table 6.5 shows the actual COP values and their corresponding theoretical limits for the cycles with three different evaporator test sections. Results are presented at two different cooling loads, 50 and 120 W. At the same cooling load, the change of the pumping power, hence, the variation of the COP value are negligible. Along with the apparent increase in the heat transfer performance, this result is a clear indication of the favorable employment of the surface roughness in refrigeration cycles. Further increase in COP may be possible with the use of a throttling valve which enables a more precise and wider range of evaporator pressures.

Table 6.5 Comparison of COP values at the same cooling load with varying roughness

R_z(μm)	q''(W/cm^2)	Q_L(W)	W_{comp}(W)	T_H(K)	T_L(K)	COP	$COP_{reversible}$
2.03	18	50	12.2	303	283	4.1	14.1
2.03	43.86	120	45.5	311.1	283.1	2.6	10.1
6.8	18	50	12.2	303.4	283	4.1	13.8
6.8	43.86	120	45.9	310.8	283	2.6	10.2
15.86	18	50	12.3	304.3	282.9	4.1	13.2
15.86	43.86	120	46	311.3	283.1	2.6	10.0

6.6 Preliminary Tests with Micro-Condenser

As the final stage of the construction of the micro-refrigeration cycle, the micro-condenser has been integrated into the test set-up. Figure 6.16 shows the photograph of the refrigeration cycle with the microscale heat exchangers, the micro-evaporator and the micro-condenser. To check if the complete cycle operates safely and properly, a preliminary test has been carried out at various saturation temperatures from 10°C to 28°C and for a mass flux of 200 kg/m^2·s. The entrance of the liquid refrigerant into the micro-evaporator has been successfully observed. The measured temperatures and pressures at different locations of the cycle for the saturation temperature of 13.3°C are illustrated in Table 6.6.

Figure 6.16 Photograph of the test setup with the micro-condenser

Table 6.6 Temperatures and pressures at various states of the cycle with micro-condenser at saturation temperature of 13.3°C

State	Position	Pressure (bar)	Temperature (°C)
1	Evaporator-inlet	4.8	13.4
2	Evaporator-outlet	4.8	13.3
3	Condenser-inlet	8.5	37.2
4	Condenser-outlet	8.5	32.1
5	Compressor-inlet	4.8	18.3
6	Compressor-outlet	8.5	29.8

It should be noted that during the preliminary tests, the objective was to observe the successful integration of the micro-condenser. For this reason, the cartridge heaters within the micro-evaporator test piece have not been operated. Only the post-heater was used to eliminate the entrance of liquid refrigerant into the micro-compressor. The experimental evaluation of the complete micro-refrigeration cycle at various heat and mass fluxes are left to be conducted as part of a future study.

CHAPTER 7

CONCLUSIONS AND FUTURE RECOMMENDATIONS

7.1 Conclusions

In the numerical part of the study, two different techniques have been employed to simulate the evaporation in the microchannels. Firstly, a numerical model has been developed based on the arbitrary Lagrangian-Eulerian description to investigate the hydrodynamics and heat transfer of an elongated vapor bubble in a microtube. COMSOL Multiphysics^{TM} has been employed as the simulation tool. The finite element method has been used to discretize the Navier-Stokes and heat transfer equations. The equations have been solved in a domain as a single flow with two subdomains and a moving mesh at the interface of the liquid and vapor phases. The proposed method has been validated against an analytical solution available in the literature. In the simulations, an initially nucleated bubble in an axisymmetric two dimensional space comes in contact with superheated water and starts growing. With the developed conservative model, it is possible to accurately estimate the velocity, temperature and pressure fields inside the microchannel for a single or multiple bubbles at any desired time.

The second numerical model based on the phase-field method has been developed, for the first time in the literature, to investigate the hydrodynamics and heat transfer characteristics of a vaporized elongated bubble in a rectangular microchannel. The robust finite element software, COMSOL Multiphysics^{TM}, has been employed by utilizing the equations for the evaporation. In the simulations, an initially nucleated bubble comes in contact with superheated water and starts growing. The simulated vapor bubble shape and the growth rate are in very good agreement with experimental results available in the literature. With the developed model, it is possible to accurately estimate the velocity, temperature and pressure fields inside the microchannel at any desired time, which is rather a difficult task in an experimental study. The variations of the local heat transfer coefficient and the heat flux along the microchannel have been investigated as well. In addition, the effects of the contact angle, and water inlet velocity on the average heat transfer coefficient have been demonstrated. A maximum local heat transfer coefficient of 137000 $W/m^2 \cdot K$ has been attained at locations where the liquid film, the bubble and the wall are all in contact. A maximum heat flux of 270 kW/m^2 could be dissipated from the bottom wall. Since the simulation of two-phase flow with evaporation in microchannels is mesh dependent and time consuming, the 2D simulation by using of Cahn-Hilliard phase-field method yields accurate results reducing the need for a 3D analysis. Furthermore, the inception of bubbles from an artificial cavity in a microchannel has been simulated. Unlike in the previous numerical studies in the literature which presume a generated bubble at the beginning of the simulations or a pseudo-boiling in which bubbles are generated by the injection, in the present work, the boiling has been initiated from a cavity. The growth and departure of the nucleated bubbles from the cavity have been simulated. Hence, a complete simulation for nucleate boiling in a microchannel was illustrated. The latter code has been expanded to the microchannels with different size of cavities to simulate a preliminary model for the surface roughness.

Imposing different mass fluxes in the microchannel with uniform temperature at the bottom wall, the following findings may be reported:

- Boiling from a cavity raises the heat transfer performance locally, more than eight times of single phase heat removal; however, it decreases sharply as the flow develops thermally in the streamwise direction.

- An optimized mass flux value of about 64 $kg/m^2 \cdot s$ has been determined to accelerate the generation of the bubbles from the cavity. For mass fluxes greater than 64 $kg/m^2 \cdot s$, a steady-state condition has been reached.

- The removed heat flux from the heated bottom wall has been illustrated at a constant time. It was affected slightly at different mass fluxes.

- The localized heat transfer from the heated bottom wall at the point of some hundred micrometers away from the artificial cavity has been depicted as time elapses. The removed heat flux and heat transfer coefficient changed periodically and their value at high mass fluxes were more than those at low mass fluxes. However, the heat transfer coefficient reduced gradually for the higher mass flux. Successive cavities have been created in the bottom wall of the microchannel to simulate a preliminary to the surface roughness. The results showed that the increase in the size of the cavities increases the heat transfer coefficient.

In the manufacturing part of the study, the surface texture of the metal-based heat sinks has been the focus. The influence of six controllable machining process parameters of WEDM, namely, the discharge current, the peak voltage, the spark time on, the spark time off, the feed rate and the wire speed, have been investigated on the surface roughness of oxygen free copper microchannels. The results of S/N ratios indicated that the capacitance which is proportional to the discharge current has the most dominant effect on surface roughness. The pulse on time and the wire speed have the second and third most effects, respectively. A neural network model has been constructed and has proved to be capable of predicting the surface roughness parameters R_a, R_z, R_v and S_m as a result of the machining process parameters. The roughness parameters measured by the 3D microscope and profile measurement device, and those predicted by the neural network model are in very good agreement with an R value of 99.5%. The achieved surface textures may be observed from the optical microscope and SEM images. The various crater sizes obtained during the WEDM process would be nucleation sites favoring evaporation in the microchannels.

In the experimental evaluation part, the hydrodynamics and heat transfer performance of the three microchannel evaporators of the same dimensions and different surface roughness have been compared at variously imposed heat fluxes and mass fluxes. For this purpose, a microscale vapor compression refrigeration cycle has been constructed. The facility and instrumentation which include the two phase flow loop have been presented. R134a has been used as the refrigerant with saturation temperature of 10°C at mass fluxes of 85 and 200 kg/(m^2·s). The COPs of 2 and 4 at mass fluxes of 85 and 200 kg/(m^2·s) indicate the at high efficiency of the cycle. The results demonstrated a significant enhancement in two-phase heat transfer at low to moderate heat flux values ranging from 0 to 48 W/cm^2. The heat transfer coefficient increased up to 45% as the surface roughness increased from test piece 1 to test piece 3. On the other hand, the maximum difference in the pressure drop was 38%.

7.2 Future Work

The Arbitrary Lagrangian-Eulerian method may be extended to include the wall in the computations as the third phase in addition to the liquid and vapor phases. However, the mesh deformation is the most challenging aspect of the method, and a criterion seems to be necessary to stop the meshing process when the meshes are deformed and remeshing the structure automatically.

Different shapes of cavity such as triangular, rectangular and sinusoidal geometries would be simulated to attain the best geometry for simulation of surface roughness effect on nucleate flow boiling in the microchannels.

The state points at the inlets and outlets of the components may be obtained precisely in the constructed microscale vapor compression refrigeration cycle. To achieve this, more precise instruments, thermistors and IR sensors, would be replaced by the thermocouples.

New experiments may be carried out to optimize the performance of the cycle. This would be attained by fabricating new micro-condensers with different geometries and fin shapes. Cooling fans with various powers could be employed to evaluate the performance of the micro-condenser.

REFERENCES

[1] Roadmap, I., International Technology Roadmap for Semiconductors, 2006 Semiconductor Industry Association, 2009, http://www.itrs.net/ Last visited on August 30, 2015

[2] S. Krishnan, S. Garimella, G. Chrysler and R. Mavajan, Towards a thermal Moore's law, IEEE Transactions on Advanced Packaging, Vol. 30(3), pp. 462-474, 2007

[3] D. C. Price, A review of selected thermal management solutions for military electronic systems, IEEE Transactions on Components and Packaging Technologies, Vol. 26(1), pp. 26-39, 2003

[4] G. Pautsch, Thermal Challenges in the Next Generation of Supercomputers, Proceeding of CoolCon MEECC Conference, pp. 1-83, PRINT ISSN #1098-7622 online ISSN #1550-0381, Scottsdale, Arizona, Publisher ACM New York, NY, USA, 2005

[5] N.E. Todreas and M. Kazimi, Nuclear Systems I: Thermal Hydraulic Fundamentals. Taylor and Francis, New York, 1 edition, 1993

[6] W.M. Rohsenow, J.P. Hartnett, and Y.I. Cho, Handbook of heat transfer, McGraw-Hill handbooks. McGraw-Hill, 1998

[7] W.M. Rohsenow, Pool boiling, in: G. Hetsroni (Ed.), Handbook of Multiphase Systems, Chapter 6.2, Hemisphere, Washington, DC, 1982

[8] S. Liter, Pool-boiling CHF enhancement by modulated porous-layer coating: theory and experiment, International journal of heat and mass transfer, 44, 22:4287-4311, 2001

[9] S. Li, M. Toprak, R. Furberg, B. Palm and M. Muhammed, The use of a nano- and microporous surface layer to enhance boiling in a plate heat exchanger, Journal of Heat Transfer, 131, 2009

[10] C.H. Wang, V.K. Dhir, On the gas entrapment and nucleation site density during pool boiling of saturated water, Journal of Heat Transfer 115 pp.670–679, 1993

[11] Y.Y. Hsu, On the size range of active nucleation cavities on a heating surface, Journal of Heat Transfer 98 pp. 207–216, 1962

[12] S. G. Kandlikar, S. Garimella, D. Li, S. Colin, M. R. King, Heat transfer and fluid flow in minichannels and microchannels, Chapter 5: Flow boiling in minichannels and microchannels, pp.175-226, 2014

[13] D. Liu, P.S. Lee, S.V. Garimella, Prediction of the onset of nucleate boiling in microchannel flow, International Journal of Heat and Mass Transfer 48 pp. 5134-5149, 2005

[14] M. Kang, Effect of surface roughness on pool boiling heat transfer, International Journal of Heat and Mass Transfer 43, pp.4073-4085, 2000

[15] B. J. Jones, J. P. McHale, and S. V. Garimella, The Influence of Surface Roughness on Nucleate Pool Boiling Heat Transfer, Journal of Heat Transfer, Vol. 131 / 121009, 2009

[16] A. Koyuncuoğlu, R. Jafari, T. Okutucu-Özyurt, H. Külah, Heat transfer and pressure drop experiments on CMOS compatible microchannel heat sinks for monolithic chip cooling applications, International Journal of Thermal Sciences 56 pp. 77-85, 2012

[17] D.B. Tuckerman, R.F.W. Pease, High-performance heat sinking for VLSI, IEEE Electron Device Letters 2, pp. 126-129, 1981

[18] B. Agostini, M. Fabbri, J.E. Park, L.Wojtan, J.R. Thome, B. Michel, State of the art of high heat flux cooling technologies, Heat Transfer Engineering28 pp. 258-281, 2007

[19] X. Wei, Y. Joshi, M.K. Patterson, Experimental and numerical study of a stacked microchannel heat sink for liquid cooling of microelectronic devices, Journal of Heat Transfer 129 1432, 2007.

[20] S.G. Kandlikar, High flux heat removal with microchannels -a roadmap of challenges and opportunities, Heat Transfer Engineering 26 pp. 5-14, 2005

[21] J. R. Thome, Boiling in microchannels: a review of experiment and theory, International Journal of Heat and Fluid Flow 25 pp. 128-139, 2004

[22] I. Mudawar, Two-Phase Microchannel Heat Sinks: Theory, Applications, and Limitations, Journal of Electronic Packaging 133 pp.041002, 2011

[23] Z. Wu, R. Du, Design and experimental study of a miniature vapor compression refrigeration system for electronics cooling, Applied Thermal Engineering 31 pp. 385-390, 2011

[24] W. Yu-Ting, Ma Chong-Fang, Zhong Xiao-Hui, Development and experimental investigation of a miniature-scale refrigeration system, Energy Conversion and Management 51 pp. 81–88, 2010

[25] S. Trutassanawin, E. A. Groll, SV. Garimella, L Gremaschi, Experimental Investigation of a Miniature-Scale Refrigeration System for Electronics Cooling, CTRC research publications (2006)

[26] R. Mongia, K. Masahiro, E. DiStefano, SMALL SCALE REFRIGERATION SYSTEM FOR ELECTRONICS COOLING WITHIN A NOTEBOOK COMPUTER, Thermal and Thermomechanical Phenomena in Electronics Systems (ITHERM '06), 2006.

[27] M. Takacs, B. Vero, I. Meszaros, Micromilling of metallic materials, Journal of Material Processing Technology 138 pp. 152-155, 2003

[28] C. R. Friedrich, M. J. Vasile, Development of the micromilling process for high-aspect ratio microstructures, JMEMS 5 pp. 33-38, 1996

[29] D. P. Adams, M. J. Vasile, G. Benavides, A. N. Campbell, Micromilling of metal alloys with focused ion beam fabricated tools, Precision Enginnering 25 pp. 107-113, 2001

[30] C. R. Friedrich, P. J. Coane, M. J. Vasile, Micromilling Development and Applications for Microfabrication, Microelectronic Engineering 35 pp. 367-372, 1997

[31] J. Li, G. K. Ananthasuresh, A quality study on the excimer laser micromachining of electro-thermal-compliant micro devices, Journal of Micromechanics and Microengineering, 11 (1) pp.38-47, 2001

[32] V. V. Semak, B. R. Campbell, J. G. Thomas, On the possible effect of pedestal pulse on material removal by ultrahigh intensity laser pulses, Journal of Physics D: Applied Physics 39 pp. 3440-3449, 2006

[33] F. H. Han, Y. Yamada, T. Kawakami, M. Kunieda, Experimental attempts of submicrometer order size machining using micro-EDM, Precision Engineering 30 pp. 123-131, 2006

[34] G. L. Benavides, L. F. Bieg, M. P. Saavedra, E. A. Bryce, High aspect ratio meso scale parts enabled by wire micro-EDM, Microsysem Technologies. 8 pp. 395-401, 2002

[35] H. S. Jang, D. S. Park, Microfabrication of Microchannels for Fuel Cell Plates, Sensors 10 pp. 167-175, 2010

[36] H. lal, H. Lal, S.S. Sehgal, Evaluation of micromachining processes for fabrication of micro-channels, International Journal of Latest Trends in Engineering and Technology (IJLTET), 2012

[37] M. Yeakub Ali, Fabrication of microfluidic channel using micro end milling and micro electrical discharge milling, International Journal of Mechanical and Materials Engineering (IJMME), Vol. 4 No. 1 pp. 93 -97, 2009

[38] B. Lu, K. Chen, W. J. Meng, F. Mei, Fabrication, assembly and heat transfer testing of low-profile copper-based microchannel heat exchangers, Journal of Micromechanics and Microengineering 20, 115002, 2010

[39] E. Vázquez, C.A. Rodríguez, A. Elías-Zúñiga, J. Ciurana, An experimental analysis of process parameters to manufacture metallic micro-channels by micro-milling, International Journal of Advanced Manufacturing Technology 51 pp. 945–955, 2010

[40] K. Iwatsuka, Y. Isokawa, Y. Maeda, H. Tanaka, T. Yazawa, S. Suzuki, Study on fine groove milling of microchannel dies Tool bending in milling of micro-grooves. Advanced Materials Research Vol. 565 pp. 523-528, 2012

[41] W. C. Jung , Y. M. Heo , G. S. Yoon , K. H. Shin , S. H. Chang , G. H. Kim, M. W. Cho, Micro Machining of Injection Mold Inserts for Fluidic Channel of Polymeric Biochips, Sensors 7 pp. 1643-1654, 2007

[42] E.S. Gadelmavla, M.M. Koura, T.M.A. Maksoud, I.M. Elewa, H.H. Soliman, Roughness Parameters, Journal of Material Processing Technology 123 pp. 133-145, 2002

[43] B. J. Jones, S. V. Garimella, Surface Roughness Effects on Flow Boiling in Microchannels, Journal of Thermal Science and Engineering Applications, Vol. 1 / 041007, 2009

[44] C.-J. Kuo, Y. Peles, Local measurement of flow boiling in structured surface microchannels, International Journal of Heat and Mass Transfer 50 pp. 4513–4526, 2007

[45] H. Honda, J. J. Wei, Enhanced boiling heat transfer from electronic components by use of surface microstructures, Experimental Thermal and Fluid Science 28 pp.159–169, 2004

[46] F. Yang, X. Dai, Y. Peles, P. Cheng, J. Khan, C. Li, Flow boiling phenomena in a single annular flow regime in microchannels (I): Characterization of flow boiling heat transfer, International Journal of Heat and Mass Transfer 68 pp. 703–715, 2014

[47] K. H. Chu, Micro and Nanostructured Surfaces for Enhanced Phase Change Heat transfer, PhD. Thesis, Massachusetts Institute of Technology, Jan. 2013

[48] B. Agostini, M. Fabbri, J.E. Park, L. Wojtan, J.R. Thome, B. Michel, State of the art of high heat flux cooling technologies, Heat Transfer Engineering 28 pp. 258–281, 2007

[49] J. Lee, I. Mudawar, Two-phase flow in high-heat-flux micro-channel heat sink for refrigeration cooling applications: Part II-pressure drop characteristics, International Journal of Heat and Mass Transfer 48 pp. 928–940, 2005

[50] J. Lee, I. Mudawar, Two-phase flow in high-heat-flux micro-channel heat sink for refrigeration cooling applications: Part II—heat transfer characteristics, International Journal of Heat and Mass Transfer 48 pp. 941–955, 2005

[51] R. Revellin, J.R. Thome, Experimental investigation of R-134a and R-245fa two-phase flow in microchannels for different flow conditions, International Journal of Heat and Fluid Flow 28 pp. 63-71, 2007

[52] B. Agostini, J.R. Thome, M. Fabbri, B. Michel, D. Calmi, U. Kloter, High heat flux flow boiling in silicon multi-microchannels - Part I: Heat transfer characteristics of refrigerant R236fa, International Journal of Heat and Mass Transfer 51pp. 5400-5411, 2008

[53] S. Bertsch, E.A. Groll, S. V. Garimella, Refrigerant flow boiling heat transfer in parallel micro channels as a function of local vapor quality, International Journal of Heat and Mass Transfer 51 pp. 4775-4787, 2008

[54] E. Costa-Party, J. Olivier, B. Michel, J.R. Thome, Two-phase flow of refrigerants in 85 lm-wide multi-microchannels: Part II – Heat transfer with 35 local heaters, International Journal of Heat and Fluid Flow 32 pp. 464-476, 2011

[55] Y.Q. Zu, Y.Y. Yan, S. Gedupudi, T. G. Karayiannis, D.B.R. Kenning, Confined bubble growth during flow boiling in mini-micro-channel of rectangular cross-section part II: approximate 3-D numerical simulation, International Journal of Thermal Sciences 50 pp. 267-273, 2011

[56] Z. Dong, J. Xu, F. Jiang, P. Liu, Numerical study of vapor bubble effect on flow and heat transfer in microchannel, International Journal of Thermal Sciences 54 pp. 22-32, 2012

[57] D.L. Sun, J.L. Xu, L. Wang, Development of a vapor-liquid phase change model for volume-of-fluid method in FLUENT, International Communications in Heat and Mass Transfer 39 pp. 1101-1106, 2012

[58] M. Magnini, B. Pulvirenti, J.R. Thome, Numerical investigation of hydrodynamics and heat transfer of elongated bubbles during flow boiling in a microchannel, International Journal of Heat and Mass Transfer 59 pp. 451-471, 2013

[59] L. Consolini, J.R. Thome, A heat transfer model for evaporation of coalescing bubbles in micro-channel flow, International Journal of Heat and Mass Transfer 31 pp. 115-125, 2010

[60] A. Mukherjee, S.G. Kandlikar, Z.J. Edel, Numerical study of bubble growth and wall heat transfer during flow boiling in a microchannel, International Journal of Heat and Mass Transfer 54 pp. 3702-3718, 2011

[61] W. Lee, G. Son, Bubble Dynamics and Heat Transfer during Nucleate Boiling in a Microchannel, Numerical Heat Transfer, Part A 53 pp. 1074–1090, 2008

[62] S. Zhou, X. Xu, B.G. Sammakia, Modeling of boiling flow in microchannels for nucleation characteristics and performance optimization, International Journal of Heat and Mass Transfer 64 pp. 706–718, 2013

[63] H.A. Akhlaghi Amiri, A.A. Hamouda, Evaluation of level set and phase-field methods in modeling two phase flow with viscosity contrast through dual-permeability porous medium, International Journal of Multiphase Flow 52 pp. 22–34, 2013

[64] R. Jafari, T. Okutucu-Özyurt, 3D numerical modeling of boiling in a microchannel by arbitrary Lagrangian–Eulerian (ALE) method, Applied Mathematics and Computations, doi:10.1016/j.amc.2015.03.042 , 2015

[65] R. Jafari, T. Okutucu-Özyurt, The Arbitrary Lagrangian-Eulerian (ALE) Modeling of a Vapor Bubble Growth in a Microtube, 12th International Conference of Numerical Analysis and Applied Mathematics, ICNAAM 2014, p. 929, Greece, September 2014

[66] J. Donea, A. Huerta, J. Ponthot, and A. Rodriguez Ferran, Encyclopedia of Computational Mechanics, Wiley & sons, 2004

[67] R. Scardovell, S. Zalesk, Direct Numerical Simulation of Free Surface and Interfacial Flow, Annual Review Fluid Mechanics 31 pp. 567–600, 1999

[68] W.H. Lee, A pressure iteration scheme for two-phase flow modeling, T.N. Veziroğlu (Ed.), Multiphase Transport Fundamentals, Reactor Safety, Applications vol. 1, Hemisphere Publishing, Washington, DC, 1980

[69] L.E. Scriven, On the Dynamics of Phase Growth, Chemical Engineering Science 10 pp. 1–13, 1959

[70] P. Aussillous, D. Quere, Quick deposition of a fluid on the wall of a tube, Physics of Fluids 12 pp. 2367-2371, 2000

[71] R. Jafari, T. Okutucu-Özyurt, Phase Field Modeling of a Vapor Bubble Growth in a Microchannel, Journal of Computational Multiphase Flows7(3) pp.143-158, 2015

[72] R. Jafari, T. Okutucu-Özyurt, CFD Modeling of Boiling in a Microchannel Based On Phase-Field Method, International Journal of Mechanical, Aerospace, Industrial and Mechatronics Engineering 9(4) pp.572-576, 2015

[73] R. Jafari, T. Okutucu-Özyurt, Numerical Simulation of Flow Boiling from an Artificial Cavity in A Microchannel, International Journal of Heat and Mass Transfer, submited to International Journal of Heat and Mass Transfer

[74] P. Yue, C. Zhou, J.J. Feng, C.F. Ollivier-Gooch, H.H. Hu, Phase-field simulations of interfacial dynamics in viscoelastic fluids using finite elements with adaptive meshing, Journal of Computational Physics 219 pp. 47–67, 2006

[75] D.M. Anderson, G.B. McFadden, Diffuse-interface methods in fluid mechanics, Annual Review Fluid Mechanics 30 pp. 139–165, 1998

[76] C. Liu, J. Shen, A phase-field model for the mixture of two incompressible fluids and its approximation by a Fourier-spectral method, Physica D 179 pp. 211–228, 2003

[77] P. Yue, J.J. Feng, C. Liu, J. Shen, A diffuse-interface method for simulating two-phase flows of complex fluids, Journal of Fluid Mechanics 515 pp. 293–317, 2004

[78] H. Gomez, V.M. Calo, Y. Bazilevs, T. J.R. Hughes, Isogeometric analysis of the Cahn-Hilliard phase-field model, Computer Methods in Applied Mechanics and Engineering 197 pp. 4333–4352, 2008

[79] I. Steinbach, Phase-field models in materials science, Modelling and Simulation in Materials Science and Engineering 17 pp. 073001-1-31, 2009

[80] C. Miehe, F. Welschinger, M. Hofacker, Thermodynamically consistent phase-field models of fracture: variational principles and multi-field FE implementations, International Journal for Numerical Methods in Engineering 83 pp. 1273–1311, 2010

[81] D. Jacqmin, Calculation of two-phase Navier–Stokes flows using phase-field modeling, Journal of Computational Physics 155 pp. 96–127, 1999

[82] H. D. Ceniceros, R. L. Nós, A. M. Romac, Three-dimensional, fully adaptive simulations of phase-field fluid models, Journal of Computational Physics 229 pp. 6135–6155, 2010

[83] V.E. Badalassi, H.D. Ceniceros, S. Banerjee, Computation of multiphase systems with phase field models, Journal of Computational Physics 190 pp. 371–397, 2003

[84] A. Badillo, Quantitative phase-field modeling for boiling phenomena, Physical Review E 86 pp. 041603-1-25, 2012

[85] W.H. Lee, A pressure iteration scheme for two-phase flow modeling, T.N. Veziroğlu (Ed.), Multiphase Transport Fundamentals, Reactor Safety, Applications, vol. 1, Hemisphere Publishing, Washington, DC, 1980.

[86] Z. Yang, X.F. Peng, P. Ye, Numerical and Experimental Investigation of Two Phase Flow During Boiling in a Coiled Tube, International Journal of Heat and Mass Transfer 51 pp. 1003-1016, 2008

[87] J. Y. Lee, M. M. Kim, M. Kaviany, S. Y. Son, Bubble nucleation in microchannel flow boiling using single artificial cavity, International Journal of Heat and Mass Transfer 54 pp. 5139–5148, 2011

[88] B.B. Mikic, W.M. Rohsenow, Bubble growth rates in non-uniform temperature field, Progress in Heat and Mass Transfer 2 pp. 283–292, 1969

[89] S. Kandlikar, S. Garimella, D. Li, S. Colin, M R. King, Heat Transfer and Fluid Flow in Minichannels and Micro channels, second edition Chapter 5, pp. 223, 2014

[90] R. Jafari, M. Kahya, S. Oliaei, H.O. Unver, T. Okutucu-Özyurt, Effect of Process Parameters on Surface Texture of Microchannels Fabricated using Micro-WEDM, submitted to International Journal of Advanced Manufacturing Technology

[91] Hsien-Ching Chen, Jen-Chang Lin, Yung-Kuang Yang, Chih-Hung Tsai, Optimization of wire electrical discharge machining for pure tungsten using a neural

network integrated simulated annealing approach, Expert Systems with Applications 37, pp. 7147–7153, 2010

[92] S. S. Mahapatra, Amar Patnaik, Optimization of wire electrical discharge machining (WEDM) process parameters using Taguchi method, International Journal of Advanced Manufacturing Technology 34, pp. 911–925, 2007

[93] P.J. Rose, Taghuchi Techniques For Quality Engineering, McGraw-Hill, USA, pp. 43-73, 1996

[94] M. P. Groover, Introduction to Manufacturing processes, WILEY, USA, pp. 85, 2012

[95] G. Taguchi, S. Chowdhury, Y. Wu, Taguchi's Quality Engineering Handbook, John Wiley & Sons, Inc., New Jersey, USA, 2004

[96] H. Demuth, M. Beale, M. Hagan, MATLAB, Neural Network ToolboxTM 6, User's Guide

[97] Y.A. Çengel, M.A. Boles, Thermodynamics An Engineering Approach, Seventh Edition, Mc Grew Hill, 2011

[98] J. R. Taylor, An introduction to error analysis, 2nd Edition, University Science Books, California, 1997

APPENDICES

A. CURRICULUM VITE

PERSONEL INFORMATION

Surname, Name: Jafari Khousheh Mehr, Rahim

Nationality: Iranian

Date and Place of Birth: 09.04.1979 Tabriz-Iran

Marital Status: Married

Phone: +90 534 299 3004

Email: e170530@metu.edu.tr

EDUCATION

Degree	Institution	Year of Graduation
MS	Urmia University	2003
BS	University of Tabriz	2001
High School	Sadi High School	1996

WORK EXPERIENCES

Year	Place	Enrollment
2010-2015	METU-Department of Mechanical Engineering	Research Assistant

FOREIGN LANGUAGES

Azerbaijani, Turkish, Persian, English

PUBLICATIONS

R. Jafari, T. Okutucu-Özyurt, Numerical Simulation of Flow Boiling from an Artificial Cavity in A Microchannel, International Journal of Heat and Mass Transfer, submitted

R. Jafari, M. Kahya, S. Olyaei, H. O. Ünver, T. Okutucu-ÖzyurtEffect of Process Parameters on Surface Texture of Microchannels Fabricated using Micro-WEDM, International Journal of Advanced Manufacturing Technology**,** submitted

R. Jafari, T. Okutucu-Özyurt, 3D Numerical Modeling of Boiling in a Microchannel by Arbitrary Lagrangian- Eulerian (ALE) Method, Applied Mathematics and Computation, http://dx.doi.org/10.1016/j.amc.2015.03.042

R. Jafari, T. Okutucu-Özyurt, Phase Field Modeling of a Vapor Bubble Growth in a Microchannel, Journal of Computational Multiphase Flows*7(3) pp.143-158, 2015*

R. Jafari, T. Okutucu-Özyurt, CFD Modeling of Boiling in a Microchannel Based On Phase-Field Method, International Journal of Mechanical, Aerospace, Industrial and Mechatronics Engineering *9(4) pp.572-576, 2015*

A. Koyuncuoğlu, R. Jafari, T. Okutucu-Özyurt, H. Külah, Heat transfer and pressure drop experiments on CMOS compatible microchannel heat sinks for monolithic chip cooling applications, International Journal of Thermal Sciences *56 pp.77-85, 2012*

S. Olyaei, R. Jafari, B. Rohani, A. Mostafapour, Investigation and Analysis of Weld Induced Residual stresses in Two Dissimilar Pipes by Finite Element Modeling, ***Journal of Applied Sciences*** *8 (6) pp. 1014-1020, 2008*

R. Jafari, T. Okutucu-Özyurt, The Arbitrary Lagrangian-Eulerian (ALE) Modeling of a Vapor Bubble Growth in a Microtube, International Conference of Numerical Analysis and Applied Mathematics, Rhodes, Greece, September 2014

R. Jafari, A. Koyuncuoğlu, T. Okutucu-Özyurt, H. Külah, MEMS Tabanlı Mikrokanallı Isı Alıcılarda Su ve Nanoakışkanlar ile Isı Transferi İyileştirme Deneyleri, 19. ULUSAL ISI BİLİMİ ve TEKNİĞİ KONGRESİ 09 -12 Eylül 2013, Samsun

R. Jafari, A. Koyuncuoğlu, T. Okutucu-Özyurt, H. Külah, Heat transfer enhancement with nanofluids in CMOS compatible microchannel heat sinks, 8. Turkey Nanoscience and Nanotechnology Conference, s.0199, OP-1, 2012